



Aalborg Universitet

AALBORG UNIVERSITY  
DENMARK

## Electronic and optical properties of graphene and other 2D materials

Petersen, René

DOI (link to publication from Publisher):  
[10.5278/vbn.phd.eng.00021](https://doi.org/10.5278/vbn.phd.eng.00021)

Publication date:  
2017

Document Version  
Publisher's PDF, also known as Version of record

[Link to publication from Aalborg University](#)

Citation for published version (APA):  
Petersen, R. (2017). *Electronic and optical properties of graphene and other 2D materials*. Aalborg Universitetsforlag. <https://doi.org/10.5278/vbn.phd.eng.00021>

### General rights

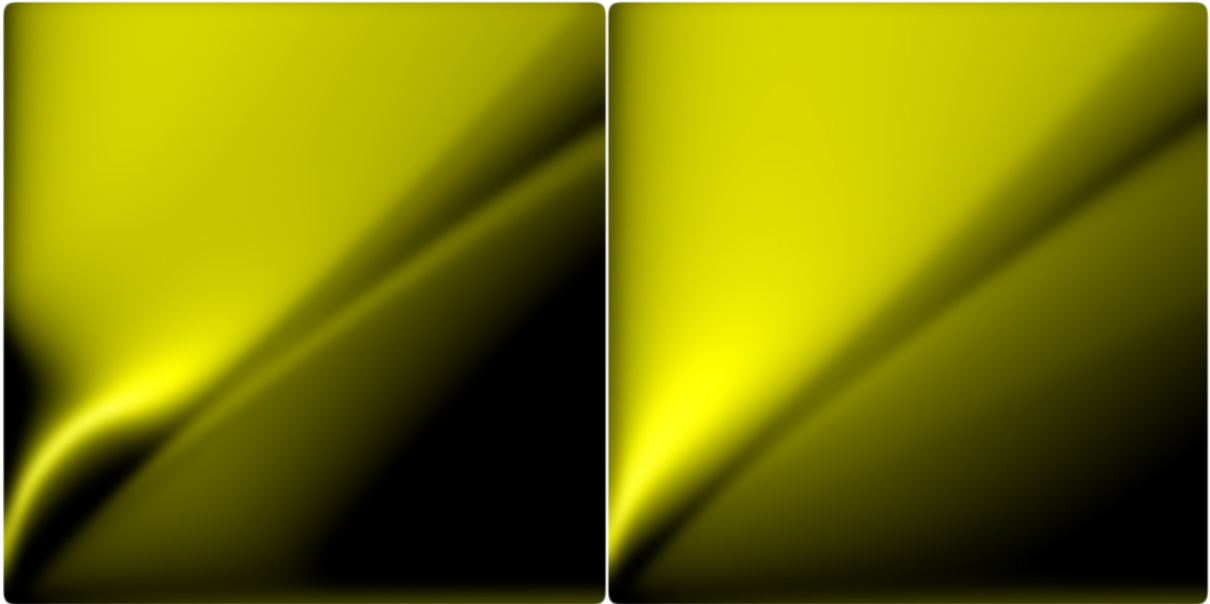
Copyright and moral rights for the publications made accessible in the public portal are retained by the authors and/or other copyright owners and it is a condition of accessing publications that users recognise and abide by the legal requirements associated with these rights.

- Users may download and print one copy of any publication from the public portal for the purpose of private study or research.
- You may not further distribute the material or use it for any profit-making activity or commercial gain
- You may freely distribute the URL identifying the publication in the public portal -

### Take down policy

If you believe that this document breaches copyright please contact us at [vbn@aub.aau.dk](mailto:vbn@aub.aau.dk) providing details, and we will remove access to the work immediately and investigate your claim.





**ELECTRONIC AND OPTICAL  
PROPERTIES OF GRAPHENE AND  
OTHER 2D MATERIALS**

**BY  
RENÉ PETERSEN**

DISSERTATION SUBMITTED 2017



**AALBORG UNIVERSITY**  
DENMARK



---

---

# Electronic and optical properties of graphene and other 2D materials

---

---

Ph.D. Dissertation  
René Petersen

Dissertation submitted September, 2017

Dissertation submitted: September, 2017

PhD supervisor: Prof. Thomas Garm Pedersen  
Aalborg University

PhD committee: Associate Professor Thomas Søndergaard (chairman)  
Aalborg University  
Dr. Alexey Yu Nikitin  
CIC Nanogune  
Donostia – San Sebastián  
Associate Professor Georg M. Bruun  
Aarhus University

PhD Series: Faculty of Engineering and Science, Aalborg University

Department: Department of Materials and Production

ISSN (online): 2446-1636  
ISBN (online): 978-87-7210-073-9

Published by:  
Aalborg University Press  
Skjernvej 4A, 2nd floor  
DK – 9220 Aalborg Ø  
Phone: +45 99407140  
aauf@forlag.aau.dk  
forlag.aau.dk

© Copyright: René Petersen

Printed in Denmark by Rosendahls, 2017

# Abstract

Graphene is a 2D sheet of carbon atoms arranged in a honeycomb lattice and it has attracted a great deal of interest due to its superior electronic properties, the possibility of its usage as the main ingredient of semiconductor devices, and for its easily tunable optical properties. Graphene has sparked a tremendous amount of work and interest also in other 2D materials such as the transition metal dichalcogenides (TMDs) and monoelement 2D materials. Recently, stacks of different 2D materials, the so-called van der Waals heterostructures, have attracted much attention due to the possibility of easy customization of the optical properties.

In order to exploit the electronic properties of graphene in semiconductor devices, it is essential to open up a bandgap in the otherwise semimetallic band structure of graphene. This can be accomplished by making a periodic array of holes in graphene thereby turning graphene into a so-called graphene antidot lattice (GAL) with a bandgap that can be tuned by varying the lattice parameters. Monolayer GALs have been intensively investigated, but bilayer GALs have so far not attracted much attention. In this work, the electronic properties of bilayer GALs are elucidated. Intrinsic bilayer graphene offers the possibility to open a bandgap and tune it simply by electrostatic gating, and it is found that it may be possible to exploit this tunability to provide for even more control over the bandgap in bilayer GALs. It is found also that bilayer GALs follow the rules for bandgap opening previously established for monolayer GALs.

To describe the optical properties of layered heterostructures it has become common practice to use the effective medium theory (EMT), which basically amounts to averaging the dielectric constants of the constituents. This is obviously an approximation, and in this work this approximation is evaluated in heterostructures of graphite and hexagonal boron nitride (hBN). Two limits are investigated: Very thin layers and very thick layers. It is found that in layers with as few as 5 monolayer sheets, EMT is a reasonable approximation, but when the layer thickness is increased EMT breaks down sooner than anticipated. It is found also that surface effects may be extremely important, in particular for evanescent light modes, something that affects heavily the de-

scription of the decay rate of a dipole, also called the Purcell factor, in the vicinity of the heterostructure.

The graphite/hBN stacks are investigated also for their properties as a hyperbolic metamaterial. Hyperbolic materials are predicted to give strong Purcell enhancement due to the hyperbolic dispersion leading to an apparent divergence in the photonic density of states. It is found, however, that the hyperbolic region does not lead to a clear signature in the Purcell factor of graphite/hBN structures because losses cause the Purcell factor to remain high also outside the hyperbolic region. 31 naturally occurring TMDs are shown to exhibit hyperbolic dispersion with unusual low losses because the special band structure features a metallic band separated by lower and higher bands by a considerable gap, large enough to separate intra- and interband losses. These materials are found to exhibit strong Purcell enhancement with a clear indication of the hyperbolic regime and an abrupt drop of emission rate outside this regime. The TMDs are compared to a conventional silver/SiO<sub>2</sub> metamaterial and found to offer much higher Purcell enhancement due to the lack of internal structure.

Finally, plasmons in doped and optically pumped graphene, MoS<sub>2</sub> and black phosphorus have been examined. In the intrinsic materials at zero temperature plasmons cannot be excited due to a lack of mobile carriers, but by optically pumping with a high intensity laser beam electrons can be excited into the conduction bands. This results in an unstable state that after a few 10s of fs decays into a metastable state that can be described with a Fermi-Dirac distribution of the electrons and holes of a temperature much above the ionic temperature. In these optically heated materials it is found that plasmons are activated and that their dispersive properties are similar to the dispersive properties in the doped materials provided that an equivalent doping level is chosen. It is furthermore found that optically activated plasmons may lead to a strong increase in the decay rate of a dipole located close to the materials.



# Resumé

Grafen er et todimensionelt materiale bestående af kulstof atomer placeret i et mønster tilsvarende hønsetrådsnet. Grafen har tiltrukket stor opmærksomhed pga. dets overlegne elektroniske egenskaber, for muligheden for måske at anvende grafen som grundsubstans i halvleder komponenter samt for dets nemt modificerbare optiske egenskaber. Grafen har desuden startet en enorm interesse også i andre 2D materialer såsom overgangsmetal dichalcogenider og enkelt element 2D materialer. På det seneste er også stakke af forskellige 2D materialer, de såkaldte van der Waals heterostrukturer, blevet grundigt undersøgt pga. muligheden for at tilpasse deres optiske egenskaber ved at vælge "byggeklodser" med passende egenskaber.

For at kunne udnytte de elektroniske egenskaber af grafen i halvleder komponenter, er det nødvendigt at åbne et båndgab i grafen, som ellers i dets naturlige form er et halvmetal. Dette kan opnås ved at lave et periodisk gitter af huller i grafen, hvormed grafen bliver til et såkaldt grafen antidot gitter med et båndgab som kan justeres blot ved at ændre parametrene for gitteret. Antidot gitre baseret på enkeltlags grafen er allerede blevet grundigt undersøgt, men der har ikke tidligere været meget interesse for antidot gitre i dobbeltlags grafen. I dette projekt undersøges de elektroniske egenskaber af dobbeltlags grafen antidot gitre. Dobbeltlags grafen i dets naturlige form giver allerede mulighed for åbning og efterfølgende justering af et båndgab ved at påspænde et elektrisk felt vinkelret på lagene. I dette projekt vises det at denne egenskab kan udnyttes også i antidot gitre i dobbeltlags grafen, til at give yderligere kontrol over båndgabet. Ydermere findes det at tidligere etablerede regler for åbning af båndgab i monolags antidot gitre, også gælder i dobbeltlags antidot gitre.

Til beskrivelse af de optiske egenskaber af stakkede heterostrukturer bestående af forskellige materialer, er det blevet normalt at anvende den såkaldte effektiv medie approksimation, som grundlæggende blot svarer til at beskrive egenskaberne af stakken ved middelværdien af permittiviteterne for de enkelte materialer. Dette er naturligvis en tilnærmelse, og i dette projekt evalueres denne tilnærmelse i heterostrukturer bestående af grafit og hexagonalt bohr nitrid (hBN). Grænserne hvor de enkelte lag er meget tynde og meget tykke

undersøges. Det findes at lag bestående af så få som 5 enkeltlag kan beskrives vha. EMT, men at EMT bryder sammen før forventet når lag tykkelsen øges. Det findes endvidere at overflade effekter kan være ekstremt vigtige, specielt for ikke propagerende lys hvilket kan have stor indflydelse på beskrivelsen af henfaldsraten af en dipol, den såkaldte Purcell faktor, i nærheden af heterostrukturen.

Grafit/hBN strukturerne er blevet undersøgt også for deres egenskaber som et hyperbolsk metamateriale. Hyperbolske materialer giver en kraftig forstærkning af Purcell faktoren, men det findes at der i grafit/hBN strukturer ikke er en tydelig forstærkning i det hyperbolske område af spektret, fordi tab i materialet bevirker at Purcell faktoren forbliver høj også udenfor det hyperbolske område. 31 naturligt forekommende overgangsmetal dichalcogenider vises at have hyperbolsk dispersion med usædvanligt lave absorptions tab pga. deres specielle båndstrukturer hvor det metalliske bånd er adskilt fra under- og overliggende bånd af et stort gab. Dette giver en adskillelse af intra- og interbånds tab, og følgelig et energiområde med lave tab. Det vises, at disse materialer har stor Purcell faktor med en klar indikation af det hyperbolske område, samt at de byder på meget større Purcell faktorer end konventionelle sølv/SiO<sub>2</sub> metamaterialer fordi de ikke har nogen indre struktur.

Slutligt er plasmoner i doteret og optisk pumpet grafen, MoS<sub>2</sub> og sort fosfor blevet undersøgt. I de naturligt forekommende materialer ved en temperatur på 0 K kan plasmoner ikke exciteres fordi der er for få frie ladningsbærere, men ved optisk pumpning med en laser ved høj intensitet, kan elektroner exciteres op i ledningsbåndene. Dette resulterer i en metastabil tilstand som kan beskrives ved en Fermi-Dirac fordeling af elektroner og huller med en temperatur meget højere end stuetemperatur. I disse optisk opvarmede materialer findes det at plasmoner er aktiveret og at deres dispersive egenskaber ligner de dispersive egenskaber af plasmoner i de doterede materialer, såfremt det ækvivalente doterings niveau bruges. Det findes endvidere, at optisk aktiverede plasmoner fører til en kraftig stigning i henfaldsraten af en dipol placeret i nærheden af et af materialerne.

# Contents

<b>Abstract</b>	<b>iii</b>
<b>Resumé</b>	<b>v</b>
<b>Thesis Details</b>	<b>ix</b>
<b>Preface</b>	<b>xi</b>
<b>1 Introduction</b>	<b>1</b>
1.1 The beginning of the 2D era . . . . .	1
1.2 This work . . . . .	3
1.2.1 Bilayer graphene antidot lattices . . . . .	3
1.2.2 Effective medium theory for the description of metamaterials . . . . .	6
1.2.3 Natural hyperbolic materials . . . . .	8
1.2.4 Optically activated plasmons in 2D materials . . . . .	10
<b>2 Theory and Methods</b>	<b>13</b>
2.1 Tight binding . . . . .	13
2.2 Optical response theory . . . . .	15
2.3 Transfer matrix method . . . . .	20
2.4 Reflection from anisotropic media . . . . .	23
2.5 Response of layered structures . . . . .	25
2.6 Effective medium theory . . . . .	25
<b>3 Summary of results</b>	<b>29</b>
3.1 Electronic properties of bilayer graphene antidot lattices . . . . .	29
3.2 Effective medium theory in graphene/hBN multilayer structures	33
3.2.1 Calculation of $\varepsilon$ using EMT and TB . . . . .	34
3.2.2 Calculation of $r^p$ using TMM based on EMT and TB . . . . .	36
3.2.3 Doped structures . . . . .	40
3.3 Natural hyperbolic materials . . . . .	42

3.4	Optically activated plasmons in 2D materials . . . . .	47
3.4.1	Doping/pumping equivalence . . . . .	48
3.4.2	Plasmon dispersion . . . . .	50
3.4.3	Purcell enhancement . . . . .	52
<b>4</b>	<b>Conclusions</b> . . . . .	<b>55</b>
	. . . . .	57

# Thesis Details

**Thesis title:** Electronic and optical properties of graphene and other 2D materials  
**Ph.D student:** René Petersen  
**Supervisor:** Thomas Garm Pedersen

The main body of this thesis consists of the following papers:

- (A). **R. Petersen** and T. G. Pedersen, “Bandgap scaling in bilayer graphene antidot lattices”, *J. Phys.: Condens. Matter.* **27**, 225502 (2015).
- (B). **R. Petersen**, T. G. Pedersen, M. N. Gjerding, and K. S. Thygesen, “Limitations of effective medium theory in multilayer graphite/hBN heterostructures”, *Phys. Rev. B.* **94**, 035128 (2016).
- (C). M. N. Gjerding, K. S. Thygsen, **R. Petersen**, T. G. Pedersen and N. A. Mortensen, “Layered van der Waals crystals with hyperbolic light dispersion”, *Nat. Commun.* **8**, 320 (2017).
- (D). **R. Petersen**, T. G. Pedersen and F. J. García de Abajo, “Nonlocal plasmonic response of doped and optically pumped graphene, MoS<sub>2</sub>, and black phosphorus”, Submitted to *Physical Review B*.

This thesis has been submitted for assessment in partial fulfillment of the Ph.D degree. The thesis is based on the submitted or published scientific papers which are listed above. Parts of the papers are used directly or indirectly in the summary in the thesis. As part of the assessment, co-author statements have been made available to the assessment committee and are also available at the Faculty. The thesis is not in its present form acceptable for open publication but only in limited and closed circulation as copyright may not be ensured.



# Preface

This thesis is the result of three years of research at the Institute of Physics and Nanotechnology at Aalborg University, Denmark from August 2014 to August 2017, under the supervision of Professor Thomas Garm Pedersen. There are a number of people to whom I owe a big thanks because they have contributed either directly or indirectly to help me finish my studies.

First, I would like to send a very special thanks to Thomas for accepting me not just once, but twice, as a PhD student, and for excellent supervision during all three years of my PhD. It has been very inspiring to work with Thomas and gain some insight into his tremendous knowledge of physics. I would like to send also a huge thanks to Prof. F. Javier García de Abajo for accepting me as a guest researcher at ICFO for four months, and for great and inspiring supervision during my stay.

I owe also a huge thanks to my colleagues, in particular Morten Rishøj Thomsen, Søren Jacob Brun and Farzad Bonabi for providing a very pleasant office and work environment, for always offering great company all the way to the coffee machine and for several table tennis matches. Thanks to all of those people for their great company at my wedding, to Søren (and his brother) for the great time we spent together in Barcelona and to Farzad for good company at the NanoP conference in Paris.

I would like to send very special thanks also to my mom and to my dad. Even though they might not have realized it at that time, they both played an important role in making it possible for me to complete my PhD studies. I am very grateful to my mom for giving me an interest in computer programming already at the age of 12. This has made so many things much easier to me, and have provided me with some of the utilities necessary for completing my studies. I owe also a huge thanks to my dad for engaging in discussions about natural sciences with me already from my childhood, and for trying his very best to answer my questions about electronics, evolution, astronomy, etc. This has without doubt given me an urge to always strive for a better understanding of all aspects of life.

Finally, I would like to thank my wife María Bartolomé Criado for great company during our numerous trips in particular to Spain and Iceland, that

has provided me with time to relax and clear my mind, and for creating an always warm and pleasant environment at home.

René Petersen  
Aalborg University, September 27, 2017



# Chapter 1

## Introduction

### 1.1 The beginning of the 2D era

Starting with the discovery of graphene in 2004 by Andre K. Geim and Kostya S. Novoselov [1] a huge research area in atomically thin materials has very quickly evolved. Graphene kick-started this area due to its numerous interesting properties such as linear band dispersion [1–4], electron mobilities of around 200000 cm<sup>2</sup>/Vs [5–7] and the relative ease with which large defect free graphene sheets can be produced [8, 9].

Much of the initial excitement about graphene was due to the prospect of producing graphene based transistors for use in electronic circuitry, but for this particular purpose intrinsic graphene is of little use because of its lack of a bandgap, the essential feature enabling turning the current on and off. Various means of introducing a bandgap into graphene has been proposed. Among these are slicing graphene into ribbons [10–15], placing graphene on a substrate [16–18], adsorbing molecules on graphene [19], and nanopatterning graphene [20–25]. With regard to the latter, it has been shown that nanopatterning of graphene and placing graphene on a substrate can drastically decrease the impressive mobility of pure graphene, although carefully choosing the substrate may yield mobilities comparable to intrinsic graphene [26–29].

Another intriguing property of graphene that has attracted much attention is the ease with which the electrical properties can be modified. Graphene is a zero-gap semiconductor (a semimetal) with the Fermi level exactly at the band crossing as shown in Fig. 1.1 and in this intrinsic state graphene exhibits a minimum electrical conductivity of  $\sigma_0 = e^2/4\hbar$  in the DC limit [25], although there is some debate about the actual value of  $\sigma_0$  [30]. Small changes in the free carrier density (the Fermi level) drastically changes the conductivity of graphene. This makes graphene a natural candidate for sensing applications as even small external disturbances can alter the Fermi level and

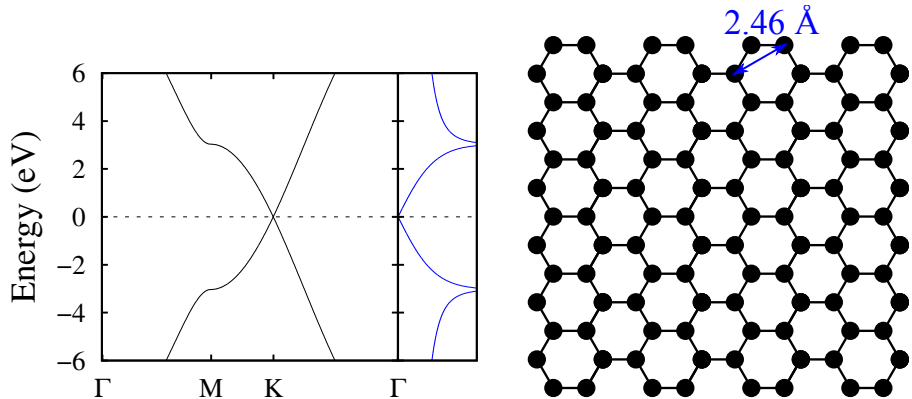


**Fig. 1.1:** (left) Band structure and density of states of intrinsic graphene and (right) geometry of a graphene sheet.

thereby the optical response [31–33], but also for optical applications where for example a back-gate configuration can be used to provide control over material response [34–36]. Also bilayer and few-layer graphene have attracted much interest [37–39] in particular due to the possibility of opening a bandgap simply by electrostatic gating [40, 41]. Bilayer graphene is much different from monolayer graphene. The band structure of A-B stacked (Bernal stacked) bilayer graphene is parabolic near the  $K$  point in the Brillouin zone although still gapless [37], but imposing a perpendicular electrostatic field causes a potential difference across the layers and the opening of a widely tunable gap in the range from 0 to 250 meV [41]. This makes bilayer graphene the only known semiconductor with a tunable bandgap and has started speculations on the possibility of a laser tunable by the electric field effect.

Following the discovery of graphene a large number of other atomically thin materials have been discovered and all these materials are collectively denoted as 2D materials [42]. Among these materials are  $\text{MoS}_2$  and other transition metal dichalcogenides (TMDs) [43], hexagonal boron nitride (hBN) [17], and mono-element 2D materials such as phosphorene and silicene [44–46]. Advances in production and transfer techniques have opened up the possibility of heterogeneous stacking of 2D materials into the so called “van der Waals heterostructures” [47, 48], an extremely interesting field of study where different 2D materials are stacked on top of each other to tailor the properties of the resulting heterostructures in order to create new materials (metamaterials).

Among the plethora of heterostructures, the combination of graphene and hBN have been the focus of much interest due to their crystal structure being identical except for a 2% difference in lattice constant [49, 50]. This has allowed epitaxial growth of graphene on hBN [51, 52] and calculations have suggested that applying a perpendicular electric field to the graphene/hBN structure

opens up a gap in graphene that can be tuned by varying the electric field much in the same way as for bilayer graphene [53].

Graphene on hBN has been suggested also as a so called hyperbolic metamaterial (HMM) [36]. In a hyperbolic material the signs of the parallel and perpendicular components of the dielectric tensor  $\varepsilon_{\parallel}$  and  $\varepsilon_{\perp}$ , respectively, differ, causing the isofrequency contours of the dispersion to be hyperbolic rather than spherical and the material to support modes of very high wavenumber  $k_x$  parallel to the surface that would otherwise be evanescent. This allows for some interesting properties such as hyperlensing and lifetime engineering [54–57, 57–61]. One generally distinguishes between type I and type II hyperbolic metamaterials (see Fig. 1.5). In a type I HMM it is the perpendicular component of the dielectric tensor that is negative, while in a type II HMM it is the parallel component. Graphite is an example of a naturally occurring type II hyperbolic material in certain spectral ranges, but other such natural hyperbolic materials may be found [62, 63] and by stacking of 2D materials one can engineer metamaterials with the desired hyperbolic properties.

## 1.2 This work

This thesis focuses on primarily two aspects of 2D materials research: bandgap engineering in graphene and optical properties of 2D materials based metamaterials. It begins with a brief literature review on the key topics of this thesis, followed by Chp. 2 dedicated to the theory and methods used. It then continues with a summary of the results in Chp. 3. Finally, in Chp. 4 the conclusions of this thesis are presented. In addition, all four papers that have been written as a part of this thesis are found in the last part of the thesis. It is emphasized that this thesis is entirely based on the results and theory of the papers, and no new results or methods are presented.

### 1.2.1 Bilayer graphene antidot lattices

As discussed earlier in this chapter, the key limitation of graphene with regards to use in semiconductor devices is the absence of a bandgap. Various methods of opening a bandgap in graphene have been suggested, but this thesis will focus on bandgap opening by nanopatterning. In 2008 it was suggested that a bandgap could be opened in graphene by introducing a periodic array of holes in the graphene sheet [20, 25, 64–66], and these structures were denoted graphene antidot lattices (GALs), see Fig. 1.2. GALs attracted interest not only for the possibility of opening of a gap, but also as plasmonic materials with prominent absorption properties [67, 68], as wave guides [69] or as barriers for electronic transport [70].

A GAL is described by the unit cell dimensions and the radius of the hole

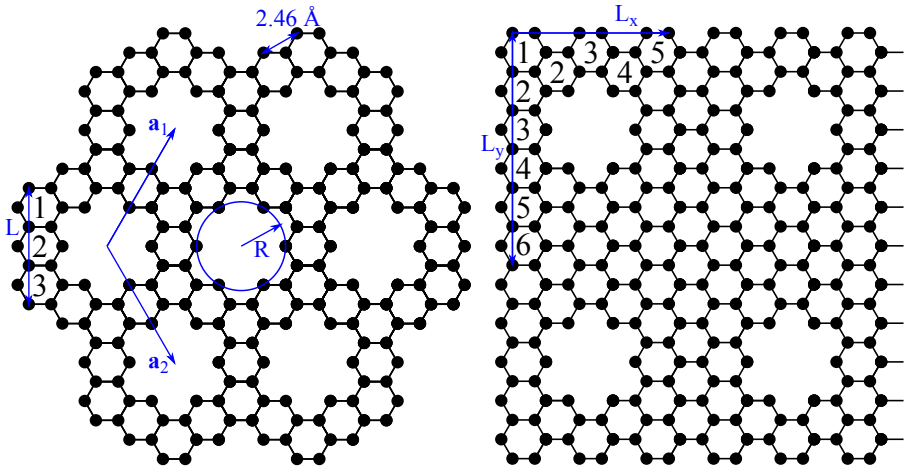


**Fig. 1.2:** (left) Geometry of a triangular  $\{3,1\}$  and (right) a square  $\{5,6,1\}$  GAL.  $\mathbf{a}_1$  and  $\mathbf{a}_2$  are the GAL lattice vectors,  $R$  is the radius of the hole and  $L$  is a measure of the unit cell dimension.

written as  $\{L,R\}$ , where  $L$  denotes the number of hexagons on the unit cell edge and  $R$  denotes the hole radius in units of  $a_0$ , see Fig. 1.2. The term antidot refers to the repelling of electrons from the holes in contrast to the trapping of electrons in a quantum dot. It was shown that a bandgap up to 1 eV can be opened in this manner [20] and that the gap depends heavily on the details of the GAL geometry [23]. For triangular GALs, it has been shown that the bandgap scales, at least approximately, linearly with the factor  $N_{\text{removed}}^{1/2}/N_{\text{total}}$ , where  $N_{\text{total}}$  is the number of atoms in the unit cell before the hole is made and  $N_{\text{removed}}$  is the number of atoms removed to form the hole [20], although some structures diverge considerably from this rule. In Ref. [71] this discrepancy was found to be due to electronic edge states on the antidots. In GALs with antidots with only zigzag edges the electrons are strongly localized to the edge of the antidot while for armchair edges the electrons are spread out over the entire GAL unit cell. In fact, GALs with armchair edges follow almost exactly the bandgap scaling rule. In 2009 Eroms *et al.* successfully produced square GALs and managed to measure a gap opening of  $\approx 6$  meV [72]. The bandgap scaling rule estimates a gap of 26 meV but some care should be taken in applying a scaling rule based on idealized structures to experimentally produced square GALs where disorder will most certainly decrease the gap. Using the block copolymer method GALs with sub-20 nm features were successfully produced in Ref. [73] and gaps of around 100 meV were estimated.

In Ref. [23, 24] it was found that the GAL geometry has a major impact on the bandgap. While all triangular GALs possess a bandgap, this is not the case for other geometries. Similar to what one observes in graphene nanoribbons

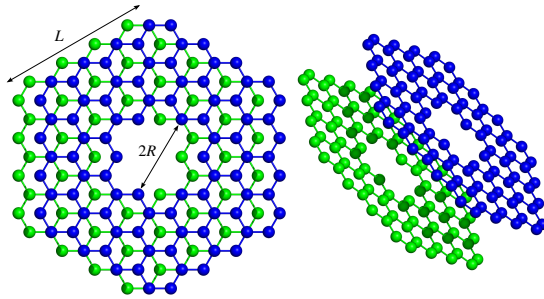


**Fig. 1.3:** Geometry of one of the investigated bilayer GALs. (from [80])

[74], the GAL gap exhibits an oscillating behavior as a function of unit cell dimensions for all but the triangular geometry. For a non-triangular GAL, the unit cell length parameter should obey  $L = 3n + 2$ , with  $n$  being a positive integer, in order for the structure to possess a large bandgap [24]. In all other cases, the structure has either zero gap or a gap much smaller than if the rule is obeyed. This rule is found to be consistent with the formation of a complete benzenoid pattern in the unit cell such that all double bonds are completely delocalized [23]. Liu *et al.* [75] and Dvorak *et al.* [76] have confirmed and extended upon these findings, and reported that the bandgap opening can be understood simply by investigation of the lattice vectors. In Ref. [77] it was shown that half of the possible triangular GALs has been unintentionally left out when constructing the unit cells as illustrated in Fig. 1.2, and that for this “missing” half the bandgap remains closed.

The studies just discussed have all been focused on GALs in monolayer graphene, although some reports on edge effects in bilayer GALs [78] and bandgap dependence on geometry in triangular bilayer GALs [79] may be found. Bilayer graphene has a number of interesting properties such as the possibility of opening and tuning the gap [40] or even activation and tuning of second harmonic generation in the otherwise intrinsically centrosymmetric crystal by applying an electrostatic field perpendicular to the layers [38]. Therefore, bilayer GALs should allow for additional tuning of the gap introduced by patterning. The contribution of this work has been to extend the previous rules of gap dependency on geometry also to bilayer GALs, and to establish bandgap scaling rules in bilayer GALs also considering the additional tunability that might be possible by applying a perpendicular electrostatic field. To obtain this goal, structures as the one shown in Fig. 1.3 have been investigated by applying tight binding (TB) based modelling of bilayer GALs, along with modelling starting from the analytical Dirac Hamiltonian of bilayer graphene including a mass term to account for the bandgap similar to how it was done in [71].

## 1.2.2 Effective medium theory for the description of metamaterials

The identification of numerous exciting 2D materials [46, 81, 82] and the possibility of stacking these materials to create metamaterials with novel properties [83, 84], calls for a simple description of the metamaterials preferably in terms of the presumably well-known properties of the constituents. Due to the extremely small thicknesses of 2D materials compared to the wavelength of visible and infrared light usually used in applications of these materials, it has become common practice to employ effective medium theory (EMT) in the description of the optical properties of layered metamaterials [57, 59, 85]. In EMT, it is assumed that the response of the constituents inside the metamaterials is identical to the response of their isolated bulk counterpart outside the metamaterial. The optical properties of the metamaterial are then calculated by averaging the permittivities of the constituents to obtain a single permittivity for the entire metamaterial, as it is depicted in Fig. 1.4a. In layered heterostructures like this it is frequently the case that the in- and out-of-plane components of the permittivity tensor differs strongly from each other, and so it becomes necessary to consider the two components separately. The EMT permittivities for planar heterostructures are given by

$$\begin{aligned}\varepsilon_{\parallel}^{\text{EMT}} &= \rho\varepsilon_{\parallel,m} + (1 - \rho)\varepsilon_{\parallel,d} \\ \frac{1}{\varepsilon_{\perp}^{\text{EMT}}} &= \frac{\rho}{\varepsilon_{\perp,m}} + \frac{1 - \rho}{\varepsilon_{\perp,d}}\end{aligned}\tag{1.1}$$

and it is seen that for the perpendicular permittivity it is the reciprocals that should be averaged. This will be discussed in more detail later.

Determining the optical properties of heterostructures in this simplified manner naturally rises a number of questions about the validity of such an approximation [87, 88]. First, it is immediately apparent that any reflection of light from the interfaces between layers is neglected in an EMT description. In addition, one could ask, how thin can the layers be before they can no longer be described by their bulk permittivities? The answers to these two questions define the regime of validity of EMT. Basically, there are two limits in between which EMT is expected to work well: The optical limit stating that the period of variation in the refractive index of the material should be much smaller than the wavelength of the incoming light (the wavelength criteria) [60, 87, 89], and the quantum limit stating that the thickness of the constituents should be sufficiently small (large) to entail an accurate description using the bulk (monolayer) properties.

To further investigate the two limits TB model of layered graphene/hBN heterostructures has been employed. This model is based on periodic structures with the unit cell as depicted Fig. 1.4b. TB parameters for an accurate description of graphene and few-layer graphene can be found in the litera-

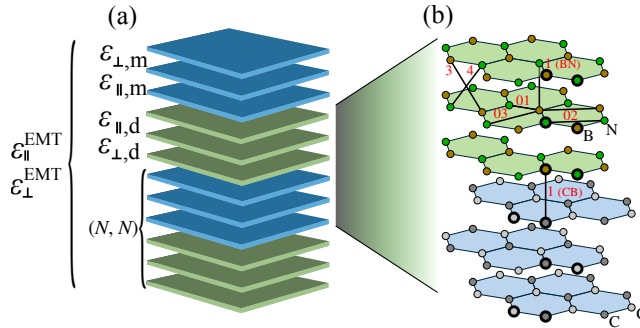


**Fig. 1.4:** (a) Illustration of a metamaterial consisting of layers of dielectric and metal with in-plane permittivities  $\epsilon_{\parallel,d}$  and  $\epsilon_{\parallel,m}$  and out-of-plane permittivities  $\epsilon_{\perp,d}$  and  $\epsilon_{\perp,m}$ . The entire metamaterial has the EMT permittivities  $\epsilon_{\parallel}^{\text{EMT}}$  and  $\epsilon_{\perp}^{\text{EMT}}$ .  $\{N, N\}$  denotes the number of consecutive graphene and hBN layers in the unit cell of the structure. (b) Illustration of the atomic structure of layered graphene/hBN structure for use for TB calculations on graphene/hBN heterostructures. (modified from [86])

ture [90] whereas for hBN the TB parameters have been determined by fitting to a density functional theory (DFT) calculation of bandstructure and optical spectra.

The quantum limit is examined by calculating the dielectric constant  $\epsilon(\omega)$  of the graphene/hBN heterostructures with varying number of graphene and hBN sheets for both the parallel and perpendicular directions, using a full quantum mechanical model taking into account also the coupling between the graphene and hBN layers [53]. The term “layers” refers to the number of graphite and hBN layers in the entire metamaterial and the term “sheet” refers to the number of atomic monolayers in each layer. Thus, the structure depicted in Fig. 1.4a consists of 4 layers and 12 sheets. Ultimately, it is the interlayer coupling between the graphene and hBN sheets and the change in electronic structure when going from many to few sheets that puts a limit to the accuracy of using bulk permittivities for the description of the individual layers. It is shown that it is possible to take this coupling into account by expanding EMT with a “boundary” term accounting for the layer coupling. This improved EMT was tested and shown to provide a better description of heterostructures of thin layers in a number of important cases.

To assess EMT in the optical limit it is natural to look at the reflection coefficient  $r^p$  for p-polarized light, since it probes both the parallel and the perpendicular response of the metamaterial due to the fact that the electric field lies in the plane of incidence. Intuitively, EMT is expected to be a good approximation in the long wavelength limit because the light does not “see” the variation in the refractive index, but previous research has shown that there might be more to that story [87]. First, rather than the vacuum wavelength it is the wavelength inside the metamaterial that counts. If the refractive

index is high, the wavelength inside the material may be considerably larger than outside. This is true in particular for evanescent light of large parallel wavenumber  $k_x > \omega/c$ . Secondly, it has been shown that the topmost layer of the metamaterial plays an important role for the optical properties of the stack [87]. Thus, the different electronic environment of the surface electrons causing the response of the first few sheets of the first layer to be different from the rest may prove to be important for the optical properties of the entire stack.

In order to assess the usability of EMT in actual applications the enhancement of the decay rate of an oscillating dipole located close to the metamaterial, the so called Purcell factor [36, 59], is calculated. It has been suggested already, that EMT may be questionable in applications regarding the decay rate of an oscillating dipole [91]. The Purcell factor depends on the reflection coefficients at high  $k_x$  and is thus a good measure of the overall performance of EMT. The Purcell factor is predicted to be large in materials exhibiting so-called hyperbolic light dispersion [57, 92]. Usually the isofrequency contours of the dispersion relation  $(k_x^2 + k_y^2)/\varepsilon_\perp + k_z^2/\varepsilon_\parallel = \omega^2/c^2$  are spherical, but for the special situation  $\varepsilon_\parallel\varepsilon_\perp < 0$  they become hyperbolic as shown in Fig. 1.5, resulting in an apparent divergence of the photonic density of states. Since the graphite/hBN structures show hyperbolic dispersion in some frequency ranges, one would expect the Purcell enhancement to be particularly strong in this regime.

### 1.2.3 Natural hyperbolic materials

Layered metamaterials, as the graphite/hBN structures discussed in the previous section, may be engineered to exhibit hyperbolic light dispersion by choosing the compounds and the layer thickness [57, 85, 92]. To establish whether a specific metamaterials exhibits hyperbolic behavior the components of the permittivity tensor are calculated from EMT. As discussed above, the applicability of EMT is limited to wavelengths much longer than the metamaterial period, and therefore any predicted hyperbolic behavior breaks down as soon as the long wavelength criterion is broken. This puts an effective upper bound to the wave vectors that see the hyperbolic dispersion, given by  $k_{\max} \sim \pi/d$  where  $d$  is the metamaterial period. To circumvent this limitation the metamaterial period should be lowered, but it is an experimentally difficult task to decrease the period below 10 nm without increasing the surface roughness to an extent that may be detrimental to the metamaterial performance [94].

A different route to obtaining materials with hyperbolic dispersion also for large wave vectors is to search for materials that are naturally hyperbolic. Such materials are not subject to the long wavelength criterion due to the lack of internal structure, and are instead limited only by the so-called non-local response [95, 96] of the material which allows for much larger wave vectors. An



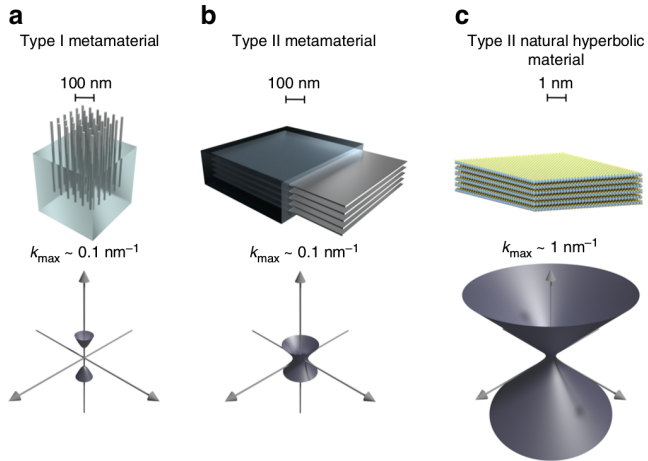


**Fig. 1.5:** Illustration of type I and type II hyperbolic metamaterials and natural a type II hyperbolic material. Due to challenges of downscaling the metamaterial period the maximum wave vector that can be supported is much smaller for the metamaterials than the natural materials. (from [93])

illustration of type I and II hyperbolic metamaterials along with a naturally occurring hyperbolic material and their isofrequency contours is shown in Fig. 1.5. Graphite has already been mentioned as one material exhibiting hyperbolic dispersion in the UV regime, and recently also other materials [62, 97, 98] including the layered tetradymites  $\text{Bi}_2\text{Te}_3$  and  $\text{Bi}_2\text{Se}_3$  [63] has been shown to exhibit hyperbolic dispersion in the near IR spectral range. The much different in- and out-of-plane dielectric properties of these layered compounds stem from the weak coupling between layers, which drastically lowers the plasma frequencies in the perpendicular direction. It is reasonable to expect many other layered compounds to exhibit similar dielectric properties, and as such, this work sets off to investigate and uncover a large class of layered TMDs exhibiting hyperbolic light dispersion in a wide spectral range covering the mid-IR to the UV. 31 different layered TMDs are shown to exhibit primarily type II hyperbolic behavior and these materials are compared to a typical artificially engineered metamaterial based on silver and  $\text{SiO}_2$ .

Conventional metamaterials such as graphene or metal based structures show substantial Purcell factors even outside the hyperbolic region due to losses [36, 59] although carefully choosing the doping level of graphene may open a spectral range of low losses [99]. Recently a number of natural TMDs exhibiting low losses in the hyperbolic region have been identified [100]. In this work, more such materials are found and investigated for their superior properties regarding the Purcell factor, and it is shown that in these materials the Purcell factors are substantially larger inside the hyperbolic region than outside.

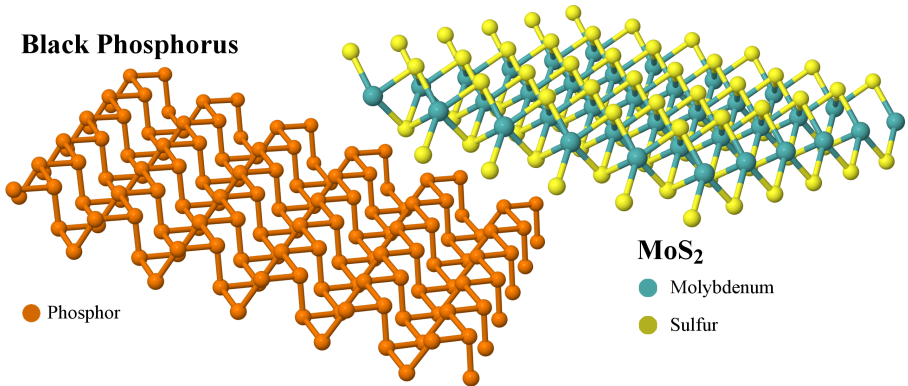


**Fig. 1.6:** Atomic structure of black phosphorus and MoS<sub>2</sub>. The structure of MoS<sub>2</sub> is similar to other TMDs.

## 1.2.4 Optically activated plasmons in 2D materials

Plasmons are collective oscillations in the free electron gas of a conductor [101]. To understand what a plasmon is, one can imagine a piece of conducting material subjected to a homogenous electric field pointing for example along the  $x$ -axis. The free electrons will redistribute such as to cancel out the electric field, and when the electric field is turned off the electrons will bounce back and forth exerting oscillating motion of some frequency  $\omega_p$  called the plasma frequency, until the energy has dissipated to losses in the material. Research in plasmons has attracted much attention due to their small extent in space making it possible to strongly confine light to small dimensions and to subsequently manipulate and guide the propagation of the plasmons on the surface of a metal [102–104]. This could be a step on the way to an all optical computer that has previously been hampered by the huge wavelength of light compared to the extent of the electronic circuits in use in modern computers. Plasmonics has already been applied in a variety of fields such as gas detection [105] and improvement of photovoltaic devices [106].

Short propagation lengths in traditional plasmonic materials such as gold and silver is a major obstacle toward applications. For this reason, there is a great motivation to investigate plasmons in the newly available 2D materials. Graphene has already shown promise in the field of plasmonics, in particular due to easy tunability of the electronic properties of graphene by gating [107, 108] the small wavelength of the plasmons and the possibility to efficiently launch plasmons in graphene [109]. Gating allows voltage control over the plasmon wavelength and amplitude [110] and even electrostatic on/off switching of the plasmons [111]. In addition to this, low losses and consequently long propagation lengths have been demonstrated in van der Waals structures

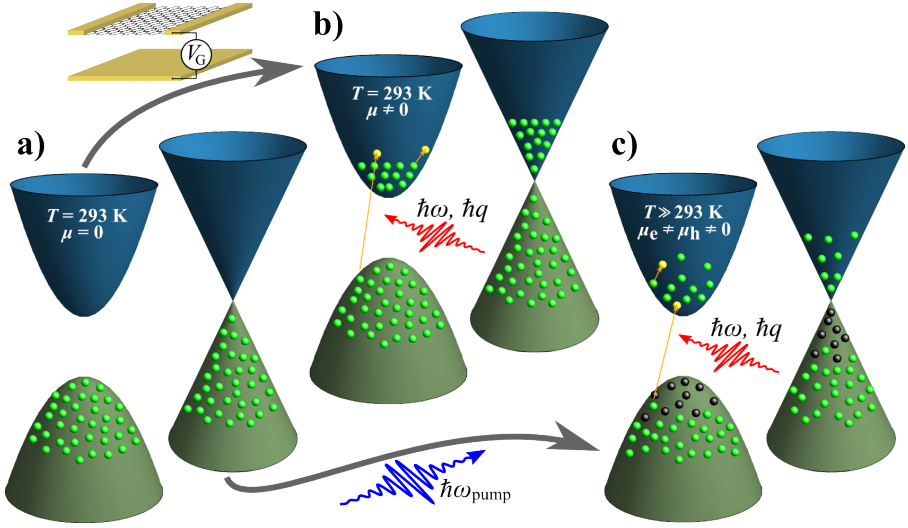


**Fig. 1.7:** Illustration of doping and pumping. (a) Intrinsic materials at low temperature (b) Electron doping for example by gating of materials at low temperature (c) Optical pumping of the materials by photons of energy  $\hbar\omega_{\text{pump}}$ . Holes are illustrated by black spheres and electrons by green spheres. Yellow spheres illustrate electrons that are excited by the probe pulse of energy  $\hbar\omega$  and momentum  $\hbar q$ .

consisting of graphene sandwiched in between two films of hBN [112].

In addition to the intense research in graphene, other 2D materials such as MoS<sub>2</sub> [113, 114] and the monoelement 2D material black phosphorus (or phosphorene) have attracted interest as plasmonic materials [115, 116]. Monolayer MoS<sub>2</sub> is made from a single layer of molybdenum between two layers of sulfur and monolayer black phosphorus consists of two layers of phosphor atoms, see Fig. 1.6. Both materials are semiconductors but black phosphorus is special in the sense that it exhibits strong anisotropic in-plane behavior and a gap tunable by applying strain along the direction perpendicular to the layers [46, 117, 118].

In this work, plasmons activated by optical pumping of graphene, MoS<sub>2</sub> and black phosphorus are investigated. In their intrinsic state and at zero temperature neither of these materials support plasmons due to a lack of free charge carriers, see Fig. 1.7a. In order to activate plasmons one has to either dope the material for example by chemical or electrical means, or alternatively, increase the temperature to thermally excite electrons into the conduction bands. In semiconductors high temperatures on the order of several thousands Kelvin are required to excite electrons across the bandgap and obtain a carrier density sufficiently high to support plasmons, so simple heating of the materials is not feasible because phonons will blur the response, if the material does not simply melt.

Because electrons are much lighter than the atom cores, it is possible to increase the effective temperature of the electrons by optically pumping the material using photons of sufficiently high energy to excite electrons into the conduction band. Dissipation of energy from the electrons to the lattice is slow, thus allowing for probing of the material response with a secondary light pulse. This technique is referred to as pump-probe spectroscopy.

Pumping of a material is different from doping. Doping the materials either introduces electrons into the conduction band (electron doping) or holes into the valence band (hole doping). This is illustrated in Fig. 1.7b for electron doping. Pumping of a material causes electrons to be excited from the valence band to the conduction band leaving behind holes in the valence band, as illustrated in Fig. 1.7c. Initially this creates an unstable out-of-equilibrium state with no well defined electronic temperature or chemical potential. By electron-electron interactions this state relaxes in the course of 10s of fs [119–124] to a Fermi-Dirac distribution to which chemical potentials for electrons and holes  $\mu_e$  and  $\mu_h$  and a temperature  $T$  can be ascribed. The electrons in this scenario are referred to as “hot electrons” because their temperature is significantly higher than room temperature, and also significantly higher than the temperature of the lattice ions. This is a transient state with a lifetime on the order of picoseconds [125] which is sufficient to allow for measurements of for example plasmons. This has already been done experimentally in graphene [126–129] and black phosphorus [130] using pump-probe spectroscopy. The idea is to first pump the material and subsequently during the lifetime of the transient state, probe the material to allow for a time-resolved investigation of the plasmonic response [128, 131–133].

In this thesis it is shown that thermally activated plasmons in graphene, MoS<sub>2</sub> and black phosphorus exhibit dispersive properties similar to plasmons activated by doping, and that the Purcell effect is strongly enhanced by plasmons both in the doping and the pumping scheme. To allow for an accurate description of plasmons in these materials, nonlocal effects [95] are taken into account by using the framework of the nonlocal-RPA to calculate the dielectric function  $\varepsilon(\mathbf{q}, \omega)$ . The results are compared to results obtained using the local-RPA approximation to reveal the importance of nonlocal effects in these materials.

# Chapter 2

## Theory and Methods

In this chapter the fundamental theory and methods used to produce the results in the next chapter are presented. It begins by presenting the quantum mechanical methods used for obtaining the electronic structure of crystalline materials and for obtaining the optical response in the limit of small electrical fields which is usually referred to as the linear response. It then proceeds with methods based on Maxwell's equations to describe the propagation of electromagnetic fields in layered structures using the calculated response functions.

### 2.1 Tight binding

The starting point of all calculations in this work is a tight binding (TB) calculation used to determine eigenstates and eigenenergies of the materials. TB is a semi-empirical method in the sense that it relies on the matrix element of the atomic wave functions with the Hamilton operator (transfer integral) and the overlap between the wave functions of electrons on different atomic sites (overlap integral). These parameters have to be determined by other means for example by fitting to a density functional theory (DFT) calculation or to experimental results.

The starting point of the TB model is the Schrödinger equation

$$\hat{H} |\Psi_n(\mathbf{r})\rangle = E_n |\Psi_n(\mathbf{r})\rangle, \quad (2.1)$$

where  $\Psi_n$  represents the  $n$ 'th eigenstate of eigenenergy  $E_n$ . The basic assumption of the TB model is that the wave function of the entire system can be constructed from the atomic wave functions of the isolated atoms that make up the system. Thus, the wave function  $\Psi_n$  is written as a linear combination

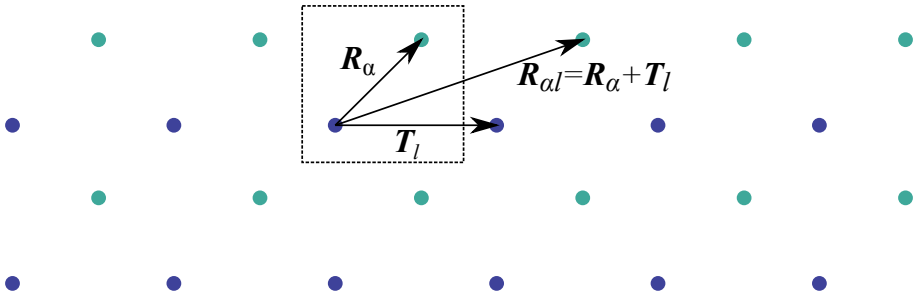


**Fig. 2.1:** Illustration of a crystal lattice with two atoms in the unit cell marked by the dashed square.  $\mathbf{R}_\alpha$  is the position of the atoms within in the unit cell,  $\mathbf{T}_l$  is a translation vector of the lattice and  $\mathbf{R}_{\alpha l} = \mathbf{R}_\alpha + \mathbf{T}_l$  is the position of atom  $\alpha$  in unit cell  $l$ ,

of atomic orbitals

$$|\Psi_n(\mathbf{r})\rangle = \frac{1}{\sqrt{U}} \sum_{\alpha}^N \sum_l^U b_{\alpha l n} |\varphi_{\alpha}(\mathbf{r} - \mathbf{R}_{\alpha l})\rangle, \quad (2.2)$$

where  $N$  is the number of orbitals in the unit cell,  $U$  is the number of unit cells,  $\varphi_{\alpha}(\mathbf{r})$  is the orbital with  $\alpha$  denoting also the orbital symmetry ( $s, p, \dots$ ), and  $\mathbf{R}_{\alpha l} = \mathbf{R}_{\alpha} + \mathbf{T}_l$  is the position of the orbital  $\alpha$  in the unit cell at the lattice translation vector  $\mathbf{T}_l$ , see Fig. 2.1. The sum is taken over all orbitals and all translation vectors of the lattice. In the following the upper limits  $N$  and  $U$  of the sums will not be written out, and it should be understood that sums over  $\alpha$  and  $\beta$  run over all orbitals and sums over  $l$  and  $l'$  run over all unit cells. According to the Bloch theorem, the wave function in a periodic crystal acquires a phase change in going from one lattice site to another. Thus, we must require that  $\Psi(\mathbf{r} + \mathbf{R}_{\alpha l}) = e^{i\mathbf{k} \cdot \mathbf{R}_{\alpha l}} \Psi(\mathbf{r})$ . Imposing this requirement one finds that  $b_{\alpha l n} = b_{n\alpha}^k e^{i\mathbf{k} \cdot \mathbf{R}_{\alpha l}}$  and therefore

$$|\Psi_n^k(\mathbf{r})\rangle = \sum_{\alpha} b_{n\alpha}^k \left[ \frac{1}{\sqrt{U}} \sum_l e^{i\mathbf{k} \cdot \mathbf{R}_{\alpha l}} |\varphi_{\alpha}(\mathbf{r} - \mathbf{R}_{\alpha l})\rangle \right] = \sum_{\alpha} b_{n\alpha}^k |\Phi_{\alpha}^k(\mathbf{r})\rangle, \quad (2.3)$$

where  $|\Phi_{\alpha}^k(\mathbf{r})\rangle$  is called the Bloch function associated with orbital  $\alpha$ . By inserting the wavefunction Eq. 2.3 into the Schrödinger equation and operating from the left with  $\langle \Phi_{\beta}^k(\mathbf{r})|$ , one gets the matrix equation

$$\sum_{\alpha} b_{n\alpha}^k H_{\alpha\beta} = E_n^k \sum_{\alpha} b_{n\alpha}^k S_{\alpha\beta}. \quad (2.4)$$

with the matrix elements of the Hamiltonian given by

$$\begin{aligned}
H_{\alpha\beta} &= \langle \Phi_{\beta}^{\mathbf{k}}(\mathbf{r}) | \hat{H} | \Phi_{\alpha}^{\mathbf{k}}(\mathbf{r}) \rangle \\
&= \frac{1}{U} \sum_l \sum_{l'} e^{i\mathbf{k}\cdot(\mathbf{R}_{\alpha l} - \mathbf{R}_{\beta l'})} \langle \varphi_{\beta}(\mathbf{r} - \mathbf{R}_{\beta l'}) | \hat{H} | \varphi_{\alpha}(\mathbf{r} - \mathbf{R}_{\alpha l}) \rangle \\
&= \sum_l e^{i\mathbf{k}\cdot(\mathbf{R}_{\alpha l} - \mathbf{R}_{\beta 0})} \langle \varphi_{\beta}(\mathbf{r} - \mathbf{R}_{\beta 0}) | \hat{H} | \varphi_{\alpha}(\mathbf{r} - \mathbf{R}_{\alpha l}) \rangle \\
&= \sum_l e^{i\mathbf{k}\cdot(\mathbf{R}_{\alpha l} - \mathbf{R}_{\beta 0})} \gamma_{\alpha\beta l},
\end{aligned} \tag{2.5}$$

and the overlap matrix elements by

$$\begin{aligned}
S_{\alpha\beta} &= \langle \Phi_{\beta}^{\mathbf{k}}(\mathbf{r}) | \Phi_{\alpha}^{\mathbf{k}}(\mathbf{r}) \rangle \\
&= \frac{1}{U} \sum_l \sum_{l'} e^{i\mathbf{k}\cdot(\mathbf{R}_{\alpha l} - \mathbf{R}_{\beta l'})} \langle \varphi_{\beta}(\mathbf{r} - \mathbf{R}_{\beta l'}) | \varphi_{\alpha}(\mathbf{r} - \mathbf{R}_{\alpha l}) \rangle \\
&= \sum_l e^{i\mathbf{k}\cdot(\mathbf{R}_{\alpha l} - \mathbf{R}_{\beta 0})} \langle \varphi_{\beta}(\mathbf{r} - \mathbf{R}_{\beta 0}) | \varphi_{\alpha}(\mathbf{r} - \mathbf{R}_{\alpha l}) \rangle \\
&= \sum_l e^{i\mathbf{k}\cdot(\mathbf{R}_{\alpha l} - \mathbf{R}_{\beta 0})} s_{\alpha\beta l},
\end{aligned} \tag{2.6}$$

and the double sum eliminates the factor of  $1/U$  because all lattice sites give the same contribution and the notation  $\mathbf{R}_{\beta 0}$  means the position of orbital  $\beta$  in the zeroth unit cell. The transfer integral  $\gamma$  and the overlap integral  $s$  are the unknown TB parameters that should be determined by other means. In the next section the framework for using the TB eigenstates and eigenenergies to determine the optical response of a material is developed.

## 2.2 Optical response theory

The optical properties of non magnetic materials are contained in the dielectric constant  $\varepsilon$  of the material. This is the quantity that enters Maxwell's equations and thus describes how the material responds to electrical fields such as light. In many isolating materials such as glass or plastic the dielectric constant is for most practical purposes a purely real quantity in the visible spectrum with a positive real part and an associated refractive index given by  $n = \sqrt{\varepsilon}$  which is also real and positive. In general, the refractive index depends on the wavelength of the light and the properties of a material may change drastically with wavelength. For example, the response of silica glass,  $\text{SiO}_2$ , is rather independent of wavelength in the visible part of the spectrum where it has a constant refractive index of  $\sim 1.5$ , but in the ultraviolet regime the material exhibits strong absorption. This is quantified by the imaginary part of the complex refractive index  $n = n' + in''$  with  $n''$  representing loss mechanisms and absorption [134]. Conducting materials are characterized by a complex dielectric

constant with a negative real part and a positive imaginary part representing losses.

The dielectric constant is directly related to several other material properties such as the electric susceptibility  $\chi_e$  and the electric conductivity  $\sigma$ . These are not independent quantities and are linked through the continuity equation  $\partial\rho/\partial t = -\nabla \cdot \mathbf{J}$  where  $\rho$  is the charge density and  $\mathbf{J}$  is the current density. The charge density is related to the polarization  $\mathbf{P}$  and the electric field  $\mathbf{E}$  as  $\rho = -\nabla \cdot \mathbf{P} = -\varepsilon_0\chi_e \nabla \cdot \mathbf{E}$  and the current density is given by  $\mathbf{J} = \sigma\mathbf{E}$ . Combining all this and assuming harmonic time dependence such that  $\mathbf{E} \propto e^{-i\omega t}$  one finds

$$\begin{aligned}\sigma &= -i\omega\varepsilon_0\chi_e, \\ \varepsilon &= 1 + \frac{i\sigma}{\varepsilon_0\omega},\end{aligned}\tag{2.7}$$

where the definition  $\varepsilon = 1 + \chi_e$  was also used.

For a very thin material the field can be taken constant in the direction perpendicular to the material and so the current flowing through the material per unit length may be calculated as  $\mathbf{J}_{2D} = d\sigma\mathbf{E} = \sigma_{2D}\mathbf{E}$ , where  $\mathbf{J}_{2D}$  is the 2D current density and  $\sigma_{2D}$  is the 2D (sheet) conductivity. In the following the subscript 2D will not be used and all references to the conductivity  $\sigma$  should be taken as references to the sheet conductivity  $\sigma_{2D}$  unless otherwise stated

The calculation of the optical response of a 2D material under illumination by a photon of energy  $\hbar\omega$  and momentum  $\hbar\mathbf{q}$  relies on linear response theory, an application of perturbation theory where only the lowest order terms are kept. In this framework, the real part  $\sigma'$  of the complex conductivity  $\sigma = \sigma' + i\sigma''$  in the zero-broadening limit is given by [135, 136]

$$\sigma'(\mathbf{q}, \omega) = \frac{e^2\omega}{2\pi q^2} \sum_{m,n} \int_{\text{BZ}} f_{nm}^{\mathbf{q}} |M_{mn}^{\mathbf{q}}|^2 \delta(E_{mn}^{\mathbf{q}} - \hbar\omega) d^2k,\tag{2.8}$$

where  $E_{mn}^{\mathbf{q}} = E_m^{\mathbf{k}-\mathbf{q}/2} - E_n^{\mathbf{k}+\mathbf{q}/2}$ ,  $f_{nm}^{\mathbf{q}} = f(E_n^{\mathbf{k}+\mathbf{q}/2}) - f(E_m^{\mathbf{k}-\mathbf{q}/2})$  with  $f(E)$  being the Fermi function,  $\hbar\mathbf{q}$  is the momentum change in the electronic transition, and

$$M_{mn}^{\mathbf{q}} = \langle \Psi_m^{\mathbf{k}-\mathbf{q}/2} | e^{-i\mathbf{q}\cdot\mathbf{r}} | \Psi_n^{\mathbf{k}+\mathbf{q}/2} \rangle\tag{2.9}$$

are the matrix elements with  $\Psi_m^{\mathbf{k}}$  being the wave functions given in Eq. 2.3. This expression considers both vertical and non-vertical electronic transition in the BZ. Non-vertical transitions are transitions in which the electron changes its momentum during the transition, which may be induced for example by phonons but also by evanescent light of high momentum. Eq. 2.8 includes both interband ( $n \neq m$ ) and intraband ( $n = m$ ) transitions, but care should be taken when using it to calculate the intraband response in the limit of



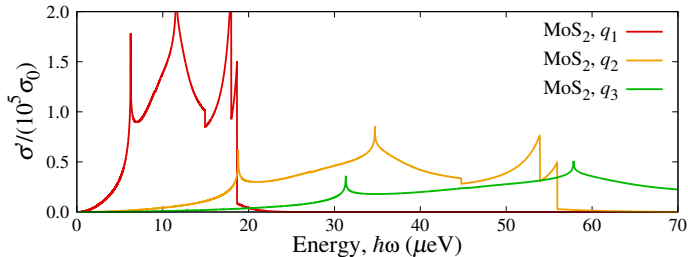


**Fig. 2.2:** Intraband conductivity in the nonlocal-RPA for  $q_1 = 10^{-5} \text{ \AA}^{-1}$ ,  $q_2 = 3 \times 10^{-5} \text{ \AA}^{-1}$ , and  $q_3 = 5 \times 10^{-5} \text{ \AA}^{-1}$  in units of  $\sigma_0 = e^2/(4\hbar)$ .

small  $q$  because in this case the intraband response is found at very small energies, see Fig. 2.2. Eq. 2.8 will from now on be referred to as the nonlocal-RPA conductivity (random phase approximation) contrary to the local-RPA which is the  $q \rightarrow 0$  limit. The associated  $\mathbf{q}$  dependent permittivity found from Eq. 2.7 is referred to as the dielectric function. The zero-broadening limit allows for easier computation using the triangle integration method [25, 38], and broadening is easily reintroduced after calculation by convolution with a Lorentzian of full width half maximum (FWHM)  $\gamma$

$$\sigma'_\gamma(\mathbf{q}, \omega) = \frac{1}{\pi} \int_{-\infty}^{\infty} \sigma'(\mathbf{q}, \omega') \frac{\gamma}{(\omega - \omega')^2 + \gamma^2} d\omega'. \quad (2.10)$$

The imaginary part can be calculated using the Kramers-Kronig relation

$$\sigma''_\gamma(\mathbf{q}, \omega) = -\frac{1}{\pi} \text{PV} \int_{-\infty}^{\infty} \sigma'_\gamma(\mathbf{q}, \omega') \frac{1}{\omega' - \omega} d\omega', \quad (2.11)$$

where PV stands for principal value. Numerically, this amounts to excluding the point  $\omega' = \omega$  from the integral. Instead of actually calculating the conductivity at negative frequencies the symmetry properties of the conductivity stating that  $\sigma'(-\omega) = \sigma'(\omega)$  and  $\sigma''(-\omega) = -\sigma''(\omega)$  can be exploited.

To numerically calculate the matrix elements  $M_{mn}^{\mathbf{q}}$  the expression for  $|\Psi_n^{\mathbf{k}}(\mathbf{r})\rangle$  given in Eq. 2.3 is inserted in Eq. 2.9 to get

$$\begin{aligned} M_{mn}^{\mathbf{q}} &= \sum_{\alpha} \sum_{\beta} \bar{b}_{m\alpha}^{\mathbf{k}-\mathbf{q}/2} b_{m\beta}^{\mathbf{k}+\mathbf{q}/2} \langle \Phi_{\alpha}^{\mathbf{k}-\mathbf{q}/2}(\mathbf{r}) | e^{-i\mathbf{q}\cdot\mathbf{r}} | \Phi_{\beta}^{\mathbf{k}+\mathbf{q}/2}(\mathbf{r}) \rangle \\ &\approx \sum_{\alpha} \sum_{\beta} \bar{b}_{m\alpha}^{\mathbf{k}-\mathbf{q}/2} b_{m\beta}^{\mathbf{k}+\mathbf{q}/2} \langle \Phi_{\alpha}^{\mathbf{k}-\mathbf{q}/2}(\mathbf{r}) | \Phi_{\beta}^{\mathbf{k}-\mathbf{q}/2}(\mathbf{r}) \rangle \\ &= \sum_{\alpha} \sum_{\beta} \bar{b}_{m\alpha}^{\mathbf{k}-\mathbf{q}/2} b_{m\beta}^{\mathbf{k}+\mathbf{q}/2} \sum_l s_{\alpha\beta l} e^{i\mathbf{k}\cdot(\mathbf{R}_{\beta 0} - \mathbf{R}_{\alpha l})} e^{i\mathbf{q}\cdot(\mathbf{R}_{\beta 0} + \mathbf{R}_{\alpha l})/2} \\ &\approx \sum_{\alpha} \bar{b}_{m\alpha}^{\mathbf{k}-\mathbf{q}/2} b_{m\alpha}^{\mathbf{k}+\mathbf{q}/2} e^{i\mathbf{q}\cdot\mathbf{R}_{\alpha 0}}, \end{aligned} \quad (2.12)$$

where  $\bar{b}$  denotes complex conjugation. The second step follows from replacing  $\mathbf{r}$  with  $\mathbf{R}_{\beta l}$  which is a good approximation under the TB assumption that the atomic orbitals are strongly localized around the nucleus to which they belong, such that the main contribution to the integrals in Eq. 2.5 and Eq. 2.6 is for  $\mathbf{r}$  close to one of the nuclei. The last step follows from assuming  $s_{\alpha\beta l} = \delta_{R_{\beta 0}, R_{\alpha l}}$ .

In the limit  $\mathbf{q} \rightarrow 0$  Eq. 2.8 reduces to the local-RPA expression. To see this the inter- and intraband cases are considered separately. For small  $q$  the exponential function can be written  $e^{-i\mathbf{q}\cdot\mathbf{r}} \approx 1 - i\mathbf{q}\cdot\mathbf{r}$  and therefore the matrix element in the interband where  $m \neq n$  case becomes

$$\begin{aligned} M_{mn}^{\mathbf{q}} &\approx \langle \Psi_m^{\mathbf{k}} | \Psi_n^{\mathbf{k}} \rangle - i\mathbf{q} \cdot \langle \Psi_m^{\mathbf{k}} | \mathbf{r} | \Psi_n^{\mathbf{k}} \rangle \\ &= -i\mathbf{q} \cdot \langle \Psi_m^{\mathbf{k}} | \mathbf{r} | \Psi_n^{\mathbf{k}} \rangle, \end{aligned} \quad (2.13)$$

where the last equality follows from the orthogonality of the states. The dipole matrix elements can be rewritten in terms of the momentum matrix elements [137, 138] and so one obtains

$$M_{mn}^{\mathbf{q}} \approx \frac{-\hbar}{mE_{mn}} \mathbf{q} \cdot \mathbf{P}_{mn}, \quad (2.14)$$

where  $\mathbf{P}_{mn} = \langle \Psi_m^{\mathbf{k}} | \hat{\mathbf{p}} | \Psi_n^{\mathbf{k}} \rangle$  and  $\hat{\mathbf{p}} = -i\hbar \nabla$  is the momentum operator. Using this in Eq. 2.8 one gets

$$\sigma'_{\text{inter}}(\omega) = \frac{e^2}{2\pi m^2 \omega} \sum_{m,n} \int_{\text{BZ}} f_{nm} |\hat{\mathbf{q}} \cdot \mathbf{P}_{mn}|^2 \delta(E_{mn} - \hbar\omega) d^2k, \quad (2.15)$$

where  $\hat{\mathbf{q}} = \mathbf{q}/q$ . To arrive at the result Eq. 2.15 we made use of the substitution  $1/E_{mn}^2 \rightarrow 1/(\hbar\omega)^2$  which is allowed because the  $\delta$  function contributes only when  $E_{mn} = \hbar\omega$ . This expression is used for calculation of the local-RPA interband conductivity. The momentum matrix elements can be calculated using  $\hat{\mathbf{p}} = (m/\hbar) \nabla_{\mathbf{k}} \hat{H}$ , which is correct in TB calculations provided the intra-atomic contribution can be neglected [137], and they are given by

$$\begin{aligned} P_{mn} &= \sum_{\alpha} \sum_{\beta} \bar{b}_{m\alpha}^{\mathbf{k}} b_{n\beta}^{\mathbf{k}} \langle \Phi_{\alpha}^{\mathbf{k}} | \hat{\mathbf{p}} | \Phi_{\beta}^{\mathbf{k}} \rangle \\ &= \frac{im}{\hbar} \sum_{\alpha} \sum_{\beta} \bar{b}_{\alpha m}^{\mathbf{k}} b_{\beta n}^{\mathbf{k}} \sum_l \gamma_{\alpha\beta l} (\mathbf{R}_{\beta 0} - \mathbf{R}_{\alpha l}) e^{i\mathbf{k}\cdot(\mathbf{R}_{\beta 0} - \mathbf{R}_{\alpha l})}. \end{aligned} \quad (2.16)$$

For the intraband case we have  $m = n$  and  $M_{nn}^{\mathbf{q}} \rightarrow 1$  for  $q \rightarrow 0$ . By inserting this in Eq. 2.8, making the substitution  $\hbar\omega \rightarrow E_{nn}$  similar to how it was done for the interband part, and using the limits

$$\begin{aligned} \lim_{q \rightarrow 0} E_{nn}^{\mathbf{q}} &= 0, \\ \lim_{q \rightarrow 0} f_{nn}^{\mathbf{q}}/q &= f'(E_{nn}) \nabla_{\mathbf{k}} E_n \cdot \hat{\mathbf{q}}, \\ \lim_{q \rightarrow 0} E_{nn}^{\mathbf{q}}/q &= \nabla_{\mathbf{k}} E_n \cdot \hat{\mathbf{q}}, \end{aligned} \quad (2.17)$$

where  $f'(E_n)$  is the energy derivative of the Fermi function, the expression

$$\sigma'_{\text{intra}}(\omega) = \frac{e^2}{2\pi\hbar} \sum_n \int_{\text{BZ}} f'(E_n) (\nabla_k E_n \cdot \hat{\mathbf{q}})^2 \delta(\hbar\omega) d^2k \quad (2.18)$$

is obtained. Now, by reintroducing a broadening  $\gamma$  using Eq. 2.10 and calculating the imaginary part using Eq. 2.11 one arrives at the Drude response  $\sigma_{\gamma,\text{intra}}(\omega) = i\varepsilon_0\omega_p^2/(\omega + i\gamma)$ , with the plasma frequency  $\omega_p$  given by

$$\omega_p^2 = \frac{-e^2}{2\pi^2\hbar^2\varepsilon_0} \sum_n \int_{\text{BZ}} f'(E_n) (\nabla_k E_n \cdot \hat{\mathbf{q}})^2 d^2k. \quad (2.19)$$

This expression and the expression in Eq. 2.15 are exactly the local-RPA expressions and agree with the results of Ref. [139] and Ref. [25]. To facilitate numerical evaluation of Eq. 2.19 the temperature is taken to zero such that  $f'(E_n)$  becomes  $-\delta(E_n - E_F)$ . This allows usage of the triangle integration method as it was done for the interband part. Subsequently, the temperature is reintroduced by convolution with the Fermi function. It should be noted that all of the above introduced formula for 2D materials can be easily extended to bulk materials simply by making the substitution  $d^2k \rightarrow 1/(2\pi)d^3k$  and replacing all vector quantities by their 3D equivalent.

In all of the above formula the direction  $\hat{\mathbf{q}}$  of the vector  $\mathbf{q}$  plays an important role because it determines the direction of the electric field to which the response is calculated. Many materials such as silica glass or silver are isotropic in the sense that the response is invariant to the direction of the polarizing field, while for other materials the direction plays a crucial role. This should not be confused with the different reflective properties of materials for s- and p-polarized light, which is a consequence solely of the boundary because the electromagnetic boundary conditions are different for transverse and perpendicular electric fields. A light pulse originating from inside the material experiences no directional dependence in its propagation in a truly isotropic material. In some materials, however, the response depends on the direction of the perturbing field and such materials are termed anisotropic or birefringent materials. An example of a strongly anisotropic naturally occurring material is graphite. Graphite is composed of sheets of graphene stacked on top of each other and these sheets interact only weakly. Consequently, the graphene sheets maintain their conductive properties in-plane, but in the out-of-plane direction graphite is an insulator (except at very long wavelengths). Anisotropic materials exhibit a number of special properties such as different refractive indices for s- and p-polarized light. In such materials, the response functions of the materials all become tensors. In this work, only planar anisotropic materials

characterized by a dielectric tensor of the form

$$\boldsymbol{\varepsilon} = \begin{pmatrix} \varepsilon_{\parallel} & 0 & 0 \\ 0 & \varepsilon_{\parallel} & 0 \\ 0 & 0 & \varepsilon_{\perp} \end{pmatrix}, \quad (2.20)$$

where  $\varepsilon_{\parallel}$  is the in-plane permittivity and  $\varepsilon_{\perp}$  is the out-of-plane permittivity, will be treated. Such materials with different in- and out-of-plane responses are termed uniaxial anisotropic media. The associated in- and out-of-plane refractive indices  $n_o = \sqrt{\varepsilon_{\parallel}}$  and  $n_e = \sqrt{\varepsilon_{\perp}}$  are often referred to as the ordinary and the extraordinary refractive indices, respectively. In the following section a method to calculate the propagation of electric fields in stacks of such structures is developed.

## 2.3 Transfer matrix method

Materials composed of layers with different optical properties constitute an exciting field of study due to the possibility of tailoring the properties to specific needs. In principle, it is possible to calculate the optical response of a stacked material using the framework described in the previous section if all layers are introduced into the Hamiltonian and  $\mathbf{q}$  chosen to be perpendicular to the layers, but care should be taken because Eq. 2.8 relies on the assumption that the electric field is constant throughout the entire structure. This assumption is fulfilled for field polarizations parallel to the layers but is, in fact, incorrect for fields polarized perpendicular to the layers. The boundary conditions for an electric field crossing the interface between two layers here designated as 1 and 2 are given by [140]

$$E_{\parallel,1} = E_{\parallel,2}, \quad (2.21)$$

$$\varepsilon_{\perp,1}E_{\perp,1} = \varepsilon_{\perp,2}E_{\perp,2}, \quad (2.22)$$

and from these conditions it is obvious that  $E_{\parallel}$  is invariant through the entire structure, while the perpendicular component changes in proportion with the difference in the permittivities of the layers. Therefore,  $\varepsilon_{\perp}$  of a stacked heterostructure cannot be calculated directly using the framework for calculation of optical response functions, and the optical properties of such materials have to be determined by relying on a method that takes into account the field variation.

Consider Fig. 2.3 illustrating propagating fields in a layered structure. Layer 0 represents the side of incoming light and layer  $N + 1$  the side of transmitted light. In layer  $i$  of the structure there will be a wave propagating left and one propagating right, except in layer  $N + 1$  where there will only be the right propagating wave transmitted through the structure. Taking  $z = 0$  to be

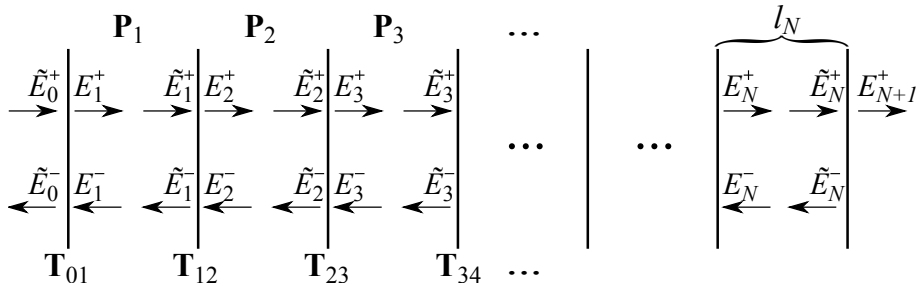


**Fig. 2.3:** Illustration of propagating fields in a layered structure. Light is incident from the left. Superscript + and - denotes a wave travelling right and left, respectively. Fields immediately left and right of an interface are written as  $\tilde{E}$  and  $E$ , respectively. On the left there will be both an incident and a reflected wave while on the right there will be only a transmitted wave.

the leftmost side of layer  $i$ , the total field in layer  $i$  is

$$E_i(z) = E_i^+ e^{ik_{z,i}z} + E_i^- e^{-ik_{z,i}z}, \quad 0 < z < l_i \quad (2.23)$$

where  $l_i$  is the width of layer  $i$ ,  $k_{z,i}$  is the  $z$ -component of the wavevector in layer  $i$  and the superscripts + and - refers to forward and backward propagating waves, respectively. Evaluating the field  $E_i(z)$  at  $z = 0$  and  $z = l_i$  one gets

$$\begin{aligned} E_i(0) &= E_i^+ + E_i^-, \\ E_i(l_i) &= E_i^+ e^{ik_{z,i}l_i} + E_i^- e^{-ik_{z,i}l_i} = \tilde{E}_i^+ + \tilde{E}_i^- = \tilde{E}_i(0), \end{aligned} \quad (2.24)$$

where  $\tilde{E}_i^+ = E_i^+ e^{ik_{z,i}l_i}$  and  $\tilde{E}_i^- = E_i^- e^{-ik_{z,i}l_i}$ .  $E_i(0)$  and  $\tilde{E}_i(0)$  are consequently the total fields in the left and right sides of layer  $i$ , respectively. Accordingly, defining  $j = i + 1$  just to avoid writing  $i + 1$  in the subscripts,  $\tilde{E}_i(0)$  and  $E_j(0)$  are the fields just left and right of the boundary between layer  $i$  and  $j$ . The aim is now to express the relation between the two fields using the transmission and reflection coefficients of the boundary. Thus, if  $r_{ij}$  and  $t_{ij}$  are the Fresnel reflection coefficients when going from layer  $i$  to layer  $j$ , then

$$\begin{aligned} \tilde{E}_i^- &= r_{ij} \tilde{E}_i^+ + t_{ij} E_j^-, \\ E_j^+ &= r_{ji} E_j^- + t_{ij} \tilde{E}_i^+. \end{aligned} \quad (2.25)$$

Now, expressing  $\tilde{E}_i^+$  and  $\tilde{E}_i^-$  in terms of  $E_j^+$  and  $E_j^-$  one gets

$$\tilde{E}_i^+ = \frac{1}{t_{ij}} E_j^+ - \frac{r_{ji}}{t_{ij}} E_j^-, \quad (2.26)$$

$$\tilde{E}_i^- = \frac{1}{t_{ij}} (t_{ij} t_{ji} - r_{ij} r_{ji}) E_j^+ + \frac{r_{ij}}{t_{ij}} E_j^-. \quad (2.27)$$

which written in matrix notation becomes

$$\begin{pmatrix} \tilde{E}_i^+ \\ \tilde{E}_i^- \end{pmatrix} = \mathbf{T}_{ij} \begin{pmatrix} E_j^+ \\ E_j^- \end{pmatrix}, \quad (2.28)$$

where the matrix  $\mathbf{T}_{ij}$  is called the transfer matrix from layer  $i$  to layer  $j = i + 1$  and it is defined as [140]

$$\mathbf{T}_{ij} = \frac{1}{t_{ij}} \begin{pmatrix} 1 & -r_{ji} \\ r_{ij} & t_{ij}t_{ji} - r_{ij}r_{ji} \end{pmatrix} \quad (2.29)$$

$$= \frac{1}{t_{ij}} \begin{pmatrix} 1 & r_{ij} \\ r_{ij} & 1 \end{pmatrix}, \quad (2.30)$$

where the last step follows from the symmetry relations of the Fresnel coefficients  $r_{ij} = -r_{ji}$  and  $t_{ij}t_{ji} - r_{ij}r_{ji} = 1$ . The transfer matrix connects the coefficients on the two sides of a boundary.

To proceed, the connection between the coefficient  $E_i^+$  and  $E_i^-$  in the left side of a layer and the coefficients  $\tilde{E}_i^+$  and  $\tilde{E}_i^-$  in the right side of the same layer is needed. This connection is given by the equations  $E_i^+ = \tilde{E}_i^+ e^{-ik_z, i l_i}$  and  $E_i^- = \tilde{E}_i^- e^{ik_z, i l_i}$ , and writing these equations in matrix form one gets

$$\begin{pmatrix} E_i^+ \\ E_i^- \end{pmatrix} = \mathbf{P}_i \begin{pmatrix} \tilde{E}_i^+ \\ \tilde{E}_i^- \end{pmatrix}, \quad (2.31)$$

with the propagation matrix  $\mathbf{P}_i$  given by [140]

$$\mathbf{P}_i = \begin{pmatrix} e^{-ik_z, i l_i} & 0 \\ 0 & e^{ik_z, i l_i} \end{pmatrix}. \quad (2.32)$$

With the transfer matrix and the propagation matrix at hand, the relation between  $\tilde{E}_0^+$ ,  $\tilde{E}_0^-$  and  $E_{N+1}^+$  can be readily determined by starting with layer  $N + 1$ , calculating the fields in layer  $N$ , then in  $N - 1$  etc.

$$\begin{pmatrix} \tilde{E}_0^+ \\ \tilde{E}_0^- \end{pmatrix} = \mathbf{S} \begin{pmatrix} E_{N+1}^+ \\ 0 \end{pmatrix}, \quad (2.33)$$

where  $\mathbf{S} = \mathbf{T}_{01}\mathbf{P}_1\mathbf{T}_{12}\mathbf{P}_2 \dots \mathbf{P}_N\mathbf{T}_{N,N+1}$  is the so called system matrix describing field propagation within the entire system. The reflection coefficient  $r = \tilde{E}_0^-/\tilde{E}_0^+$  and transmission coefficient  $t = E_{N+1}^+/\tilde{E}_0^+$  of the entire stack are given by

$$r = \frac{S_{21}}{S_{11}}, \quad t = \frac{1}{S_{11}}, \quad (2.34)$$

with  $S_{mn}$  being elements of the system matrix. Since the reflection coefficient of the system is given by the ratio between two element of the system matrix, the prefactors  $t_{ij}^{-1}$  of  $\mathbf{T}$  cancel out, and the reflection coefficient of the stack depends only on the reflection coefficients of the layer boundaries.

## 2.4 Reflection from anisotropic media

The transfer matrix method developed in the previous section relies on knowledge of the Fresnel reflection coefficients  $r_{ij}$  and  $t_{ij}$  of every boundary between two media of different dielectric constants  $\varepsilon_i$  and  $\varepsilon_j$ . For isotropic materials the Fresnel coefficients take their usual form which for s- and p-polarized light are [140]

$$r_{ij}^s = \frac{k_{z,i} - k_{z,j}}{k_{z,i} + k_{z,j}} \quad t_{ij}^s = \frac{2k_{z,i}}{k_{z,i} + k_{z,j}}, \quad (2.35)$$

$$r_{ij}^p = \frac{n_j^2 k_{z,i} - n_i^2 k_{z,j}}{n_j^2 k_{z,i} + n_i^2 k_{z,j}} \quad t_{ij}^p = \frac{2n_i n_j k_{z,i}}{n_j^2 k_{z,i} + n_i^2 k_{z,j}}, \quad (2.36)$$

with  $n_i = \sqrt{\varepsilon_i}$  being the complex refractive index and  $k_{z,i}$  being the  $z$ -component of the wavevector  $\mathbf{k}$  in layer  $i$ . For anisotropic media like the uniaxial media described by the dielectric tensor  $\boldsymbol{\varepsilon}$  of Eq. 2.20, however, the Fresnel coefficients are different. To find them, consider the wave equation in anisotropic media [141, 142]

$$\nabla^2 \mathbf{E}(\mathbf{r}) + k_0^2 \boldsymbol{\varepsilon} \mathbf{E}(\mathbf{r}) - \nabla(\nabla \cdot \mathbf{E}(\mathbf{r})) = 0, \quad (2.37)$$

where  $k_0 = \omega/c$  is the vacuum wavenumber and  $\omega$  is the light frequency. In the following the coordinate system is chosen to be oriented such that the interface between the medium of incidence and the anisotropic medium lies in the  $xy$ -plane. For an electric field given by  $\mathbf{E}(\mathbf{r}) = \mathbf{E}_0 e^{i\mathbf{k} \cdot \mathbf{r}}$  this equation assumes the form

$$-k^2 \mathbf{E}_0 + k_0^2 \boldsymbol{\varepsilon} \mathbf{E}_0 + \mathbf{k}(\mathbf{k} \cdot \mathbf{E}_0) = 0 \quad (2.38)$$

which is in fact three equations, one for each Cartesian component. Now, for s-polarization the electric field lies entirely in the plane of the boundary, that is,  $\mathbf{E}_0 = E_y \hat{\mathbf{y}}$ . In this case, one finds from the  $x$ - and  $z$ -components of Eq. 2.38 that  $k_y$  can be taken to be zero, and from the  $y$ -component that  $k_z^s = \pm \sqrt{k_0^2 \varepsilon_{\parallel} + k_x^2}$ . The positive and negative solutions correspond respectively to waves travelling towards and away from the interface. Thus, the wave propagation direction for s-polarized light in anisotropic media is seen to be identical to the case of isotropic media. Intuitively, this makes sense since light polarized parallel to the interface does not cause any polarization in the out-of-plane direction, and so does not see the out-of-plane permittivity.

For p-polarized light the electric field is of the form  $\mathbf{E}_0 = E_x \hat{\mathbf{x}} + E_z \hat{\mathbf{z}}$ . Inserting this in Eq. 2.38 yields again an equation for each of the three Cartesian coordinates and from the  $y$ -component one finds  $k_y = 0$ . The other two equations yield

$$k_z^p = \pm \sqrt{k_0^2 \varepsilon_{\parallel} + k_x^2 \varepsilon_{\parallel} / \varepsilon_{\perp}}, \quad (2.39)$$

showing that propagation of p-polarized light in uniaxial anisotropic media does indeed depend on both the in-plane and out-of-plane components of the dielectric tensor. The equations also give the field directions, and solving for instance for  $E_z$  one finds that the electric field inside the anisotropic material can be written as (it is only defined up to a constant)

$$\mathbf{E}_0 = E_0 \left( \mp \frac{k_z^{\text{P}}}{\varepsilon_{\parallel}}, 0, \frac{k_x}{\varepsilon_{\perp}} \right) \quad (2.40)$$

where  $E_0$  is a constant. From this it is seen that in the anisotropic case  $\varepsilon_{\parallel} \neq \varepsilon_{\perp}$  the electric field is not perpendicular to the wave vector  $\mathbf{k}^{\text{P}} = (k_x, 0, k_z^{\text{P}})$ . The electric displacement field, however, is perpendicular to  $\mathbf{k}^{\text{P}}$  and it is given by  $\mathbf{D}_0 = \boldsymbol{\varepsilon} \mathbf{E}_0 = E_0 (\mp k_z, 0, k_x)$ . The normalized direction of the displacement field is

$$\mathbf{d}^{\text{P}} = \frac{1}{\sqrt{k_x^2 + k_z^2}} (\mp k_z, 0, k_x) = \frac{1}{n^{\text{P}} k_0} (\mp k_z, 0, k_x), \quad (2.41)$$

where  $n^{\text{P}}$  can be seen as an effective index of refraction that is given by

$$n^{\text{P}} = \frac{\sqrt{\mathbf{k}^{\text{P}} \cdot \mathbf{k}^{\text{P}}}}{k_0} = \sqrt{\varepsilon_{\parallel} - \left(1 - \frac{\varepsilon_{\perp}}{\varepsilon_{\parallel}}\right) \frac{k_x^2}{k_0^2}}. \quad (2.42)$$

The effective refractive index is seen to reduce to  $n = \sqrt{\varepsilon}$  in the isotropic case  $\varepsilon_{\parallel} = \varepsilon_{\perp} = \varepsilon$ .

To derive the reflection and transmission coefficients in the anisotropic case, the incident, reflected and transmitted fields are expressed and the electromagnetic boundary conditions Eq. 2.22 used to provide the relationship between the field amplitudes. The fields are given as

$$\mathbf{E}_{\text{inc}}(\mathbf{r}) = E_0 (k_{z,i}^{\text{P}}/\varepsilon_{\parallel,i}, 0, k_x/\varepsilon_{\perp,i}) e^{-ik_{z,i}^{\text{P}}z} e^{ik_x x}, \quad (2.43)$$

$$\mathbf{E}_{\text{refl}}(\mathbf{r}) = r_{ij}^{\text{P}} E_0 (-k_{z,i}^{\text{P}}/\varepsilon_{\parallel,i}, 0, k_x/\varepsilon_{\perp,i}) e^{ik_{z,i}^{\text{P}}z} e^{ik_x x}, \quad (2.44)$$

$$\mathbf{E}_{\text{trans}}(\mathbf{r}) = t_{ij}^{\text{P}} E_0 (k_{z,j}^{\text{P}}/\varepsilon_{\parallel,j}, 0, k_x/\varepsilon_{\perp,j}) e^{-ik_{z,j}^{\text{P}}z} e^{ik_x x}, \quad (2.45)$$

where  $k_{z,i}^{\text{P}} = \sqrt{k_0^2 \varepsilon_{\parallel,i} + k_x^2 \varepsilon_{\parallel,i} / \varepsilon_{\perp,i}}$  and  $E_0$  is the field amplitude. From the electromagnetic boundary conditions the reflection and transmission coefficients are found to be given by [141, 142]

$$r_{ij}^{\text{P}} = \frac{\varepsilon_{\parallel,j} k_{z,i}^{\text{P}} - \varepsilon_{\parallel,i} k_{z,j}^{\text{P}}}{\varepsilon_{\parallel,j} k_{z,i}^{\text{P}} + \varepsilon_{\parallel,i} k_{z,j}^{\text{P}}}, \quad (2.46)$$

$$t_{ij}^{\text{P}} = \frac{2\varepsilon_{\parallel,j} k_{z,j}^{\text{P}}}{\varepsilon_{\parallel,j} k_{z,i}^{\text{P}} + \varepsilon_{\parallel,i} k_{z,j}^{\text{P}}}, \quad (2.47)$$

and it is seen that the form of the Fresnel coefficients is identical to the isotropic case and therefore that the symmetry properties are unchanged, such that the transfer matrix in the last line of Eq. 2.30 continues to be valid.



## 2.5 Response of layered structures

In the calculation of the response of structures composed of sheets of atomic monolayers, such as naturally occurring graphite or hexagonal boron nitride, or artificially structured metamaterials, composed of layers of different materials that are again composed of monolayers sheets, the response of each individual sheet will in general be different. This is important when calculating for example optical reflection or transmission, since when light enters the structure it is refracted in the first sheet and it is this refracted light, which is then seen by the second sheet. As such, to permit an accurate description of the entire stack, it is in general not enough to assign a refractive index to the entire stack nor is it enough to treat the individual layers as homogenous. An individual calculation of the refractive properties of each sheet of the entire stack is necessary to accurately describe light propagation in the heterostructure and to enable treatment of edge effects on the top and bottommost layers.

To get the individual sheet response the local-RPA projected conductivity is introduced. The projected conductivity gives the contribution from a set  $A = \{\alpha_1, \alpha_2, \dots\}$  of atoms in the unit cell to the total conductivity. To calculate the conductivity due to the atoms in the set  $A$ , the matrix element  $P_{mn}$  is replaced by the matrix element  $M_{mn}^A = \text{Re}(P_{mn}^A \bar{P}_{mn})$  with

$$P_{mn}^A(\mathbf{k}) = \frac{1}{2} \sum_{\alpha \in A} \sum_{\beta}^N [\bar{b}_{m\alpha}^{\mathbf{k}} b_{n\beta}^{\mathbf{k}} + \bar{b}_{m\beta}^{\mathbf{k}} b_{n\alpha}^{\mathbf{k}}] \langle \Phi_{\alpha}^{\mathbf{k}} | \hat{\mathbf{p}} | \Phi_{\beta}^{\mathbf{k}} \rangle, \quad (2.48)$$

being the projected momentum matrix element.  $P_{mn}^A$  reduces to the total matrix element given in Eq. 2.16 if the set  $A$  includes all atoms in the unit cell. In this case interchanging  $\alpha$  and  $\beta$  gives the same result and eliminates the factor of  $1/2$ .

## 2.6 Effective medium theory

In a layered heterostructure composed of thin layers with respect to the wavelength of the light that illuminates the structure, the variation in refractive index may under certain circumstances be ignored because the wavelength of the light is much longer than the period of variation. In this case, it is common to describe the entire layered medium by a single effective refractive index based on the refractive indices of the constituents, and this method is referred to as homogenization or effective medium theory (EMT). Characterizing a heterostructure by a single material parameter is practical because it allows for a characterization of the structure as being metallic or dielectric by just looking at a single parameter, instead of having to calculate for example the reflection spectrum to see how the structure behaves. There is reason to be careful

though, and EMT relies on a number of assumptions. First, EMT cannot catch the phase change across individual layers and thus multiple reflection effects are absent in such a description. If the wavelength is, in fact, much larger than the period of variation in the heterostructure, such effects are of course small, but one should bear in mind that it is the wavelength *in* the layer that counts. As such, a thin layer with a high refractive index may cause a significant phases change across it. Secondly, it is an assumption that the incoming light actually sees several periods of layers. Thus, if one of the first few layers is very lossy it does not make sense to describe the structure as an effective medium because only a few layers are actually seen by the light.

The formulas for calculating the effective permittivity of a heterostructure, may be derived by averaging the perpendicular component of the electric field  $\mathbf{E}$ , and the parallel component of the displacement field  $\mathbf{D} = \boldsymbol{\varepsilon}\mathbf{D}$  over the entire structure and applying the electromagnetic boundary conditions [56]. Here  $\boldsymbol{\varepsilon}$  is the permittivity tensor which in a uniaxial planar heterostructure is given from Eq. 2.20. Considering a heterostructure composed of metal and dielectric layers, the parallel component of the average displacement field  $D_{\parallel}^{\text{avg}} = \varepsilon_{\parallel}^{\text{EMT}} E_{\parallel}^{\text{avg}}$ , with  $\varepsilon_{\parallel}^{\text{EMT}}$  being the sought effective permittivity, is

$$D_{\parallel}^{\text{avg}} = \rho D_{\parallel,m} + (1 - \rho) D_{\parallel,d}, \quad (2.49)$$

where  $D_{\parallel,m} = \varepsilon_{\parallel,m} E_{\parallel,m}$  and  $D_{\parallel,d} = \varepsilon_{\parallel,d} E_{\parallel,d}$  are the displacement fields in the metal and the dielectric, respectively, and  $\rho$  is the fraction of metal in the structure. The boundary condition for the electric field given in Eq. 2.22 state that  $E_{\parallel}^{\text{avg}} = E_{\parallel,m} = E_{\parallel,d}$  and one finds

$$\varepsilon_{\parallel}^{\text{EMT}} = \rho \varepsilon_{\parallel,m} + (1 - \rho) \varepsilon_{\parallel,d}. \quad (2.50)$$

Similarly, by averaging the electric field and using the boundary condition for the displacement field in Eq. 2.22 one finds for the perpendicular component

$$\frac{1}{\varepsilon_{\perp}^{\text{EMT}}} = \frac{\rho}{\varepsilon_{\perp,m}} + \frac{1 - \rho}{\varepsilon_{\perp,d}}. \quad (2.51)$$

The EMT permittivities allows for characterization of a material as metallic or dielectric, and in certain cases a material may even exhibit both metallic and dielectric behavior in the sense that particular choices of the constituent materials and the metal fill fraction  $\rho$ , may lead to metallic behavior in-plane and dielectric behavior out-of-plane. Such materials are strongly anisotropic and exhibit unusual properties. The dispersion relation for a wave propagating in an anisotropic material is found from Eq. 2.39 (generalizing to fields in the  $xy$ -plane) and it is given by

$$\frac{k_x^2 + k_y^2}{\varepsilon_{\perp}} + \frac{k_z^2}{\varepsilon_{\parallel}} = \frac{\omega^2}{c^2}. \quad (2.52)$$

For the case  $\varepsilon_{\parallel} > 0$  and  $\varepsilon_{\perp} > 0$  the isofrequency contours of Eq. 2.52 are elliptical meaning that the allowed values of  $k$  are restricted to lie on an ellipse. Wave components with wavenumbers outside this ellipse are evanescent in the material. For materials for which  $\varepsilon_{\parallel}\varepsilon_{\perp} < 0$ , the isofrequency contours are not spherical but hyperbolic, and therefore these materials are termed hyperbolic materials. In these materials an, in theory, infinite range of  $k$ -modes are allowed to propagate and these materials can have a great impact when placed in the near field of an oscillating dipole. An oscillating dipole emits light of modes that are evanescent in air and they are accordingly only detectable in the near field. These non-propagating modes do not carry away any energy for an isolated dipole, but if the dipole is placed in the vicinity of a hyperbolic material these evanescent modes can couple to the material. This effectively increases drastically the decay rate of the dipole, an effect referred to as the Purcell effect. The Purcell factor, that is, the ratio between the decay rate  $\Gamma$  close to the hyperbolic material and the decay rate  $\Gamma_0$  in vacuum, is for a dipole oriented parallel to the surface of the material given by [59]

$$\frac{\Gamma}{\Gamma_0} = 1 + \frac{3}{4k_0} \operatorname{Re} \left( \int_0^{\infty} \left( r^s - \frac{k_z^2}{k_0^2} r^p \right) \frac{k_x e^{2ik_z d}}{k_z} dk \right), \quad (2.53)$$

where  $d$  is the distance between the dipole and the surface,  $k_z = \sqrt{\varepsilon k_0^2 - k_x^2}$ ,  $\varepsilon$  is the permittivity of the ambient and  $r^s$  and  $r^p$  are the reflection coefficients of the material. Thus, the Purcell factor is determined entirely once the reflection coefficients of the material are known.



# Chapter 3

## Summary of results

In this chapter, a summary of the results from the papers included in the last part of this thesis is presented. The aim is to provide the reader with an overview of the work that has been accomplished during this Ph.D. project. Not all details of the results are discussed, and the reader is referred to the papers for an in-depth treatment.

### 3.1 Electronic properties of bilayer graphene antidot lattices

Graphene antidot lattices (GALs) have been proposed as a way of turning graphene semiconducting. It has been shown that by making a periodic array of holes in graphene, a bandgap opens up and this gap can be tuned by varying the hole separation and the hole diameter [20]. Previous work has shown that the appearance of a large bandgap can be correlated with the Clar sextet structure of the lattice, that is, the possibility of forming a complete benzenoid pattern in the GAL [23, 24]. Only those GALs with completely delocalized electrons have a large bandgap, whereas the rest have either zero band gap or a “small” bandgap [23]. This is illustrated in Fig. 3.1, where the band structure for hexagonal and square monolayer GALs are shown in red along with their Clar sextet structure.

It turns out that all the triangular lattices have large bandgaps but for 30° rotated triangular, square and honeycomb lattices, only every third GAL with respect to the unit cell size allow for a complete Clar structure and thus possess a large gap. This behavior is similar to what has been observed also in graphene nanoribbons [74]. The observation can be formulated in a set of simple restrictions on the unit cell dimensions, such that for a square lattice to possess a large gap one needs the unit cell height  $L_y = 3n + 2$  while for a

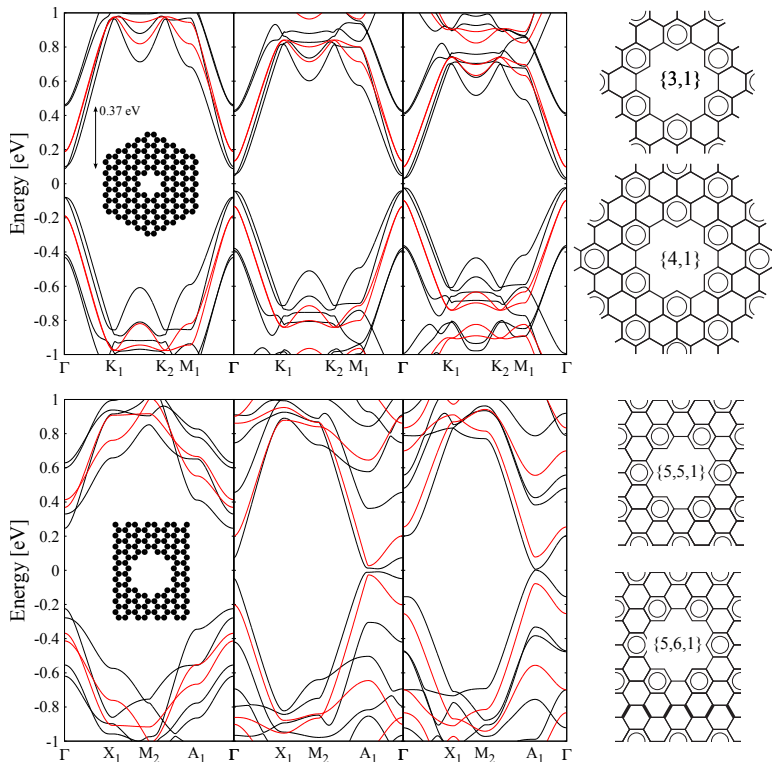


**Fig. 3.1:** (top left) Band structures of triangular and (bottom left) square mono- (red curves) and bilayer (black curves) GALs, along with (right) examples of Clar sextet structures. All hexagonal GALs have large bandgaps while only every third square GAL have a large gap. (from [23, 80])

rotated triangular or a honeycomb lattice to have a large gap one needs the unit cell to have a side length  $L = 3n + 2$  with  $n$  a positive integer and  $L$  and  $L_y$  measured in units of the graphene lattice constant  $a_0 = 2.46 \text{ \AA}$  (see Fig. 1.2).

In paper A GALs in bilayer graphene are investigated using a tight binding (TB) model with the parameters from Ref. [37] and by using a Dirac model to make a simplified analytical analysis. The most stable form of bilayer graphene is the AB stacking, also called Bernal stacking, of the monolayer sheets, where each carbon atom in the top sheet is located in the center of each hexagon beneath it (see Fig. 1.3). In order to maintain similar holes in the two sheets in this geometry, the holes are shifted by  $a_{cc} = 1.42 \text{ \AA}$  (the CC bond length) along one of the bonds and it is assumed that no reconfiguring of the atoms near the hole edge takes place. This assumption is in fact wrong [79], but it is not expected to strongly influence the conclusions in the present investigation.

For bilayer GALs the criteria for gap opening turns out to be identical to those for monolayer GALs as it is seen by comparing the band structures of mono- and bilayer GALs in Fig. 3.1 where two different geometries are shown. This finding is true also for bilayer GALs of other geometries as it is shown in paper A. It is, however, reasonable to expect the monolayer GAL bandgap scaling with  $N_{\text{removed}}^{1/2}/N_{\text{total}}$  as discussed in the introduction, to be different in bilayer GALs due to the different electronic structure.

A simplified analysis of GALs can be made by replacing the actual unit cell by a circular unit cell of radius  $R_e$  with a hole of radius  $R$ .  $R_e$  is chosen such that the area of the circular unit cell is equal to the area of the actual unit cell before the hole is made. At low energies this system can be described by a massive Dirac Hamiltonian with a spatially varying mass term  $\Delta(r) = \Delta_0\theta(R - r)$ , where  $R$  is the hole radius and  $\Delta_0$  the constant value of the mass term inside the hole, accounting for the effect of the holes. The Hamiltonian is written as

$$\mathbf{H} = \begin{pmatrix} \Delta(r) & -\hat{O}_- & 0 & \gamma_1 \\ -\hat{O}_+ & -\Delta(r) & 0 & 0 \\ 0 & 0 & \Delta(r) & -\hat{O}_- \\ \gamma_1 & 0 & -\hat{O}_+ & -\Delta(r) \end{pmatrix}, \quad (3.1)$$

with the operator  $\hat{O}_\pm = -i\hbar v_F e^{\pm i\theta} (\partial_r \pm \frac{i}{r}\partial_\theta)$  where  $v_F$  is the Fermi velocity, and  $\gamma_1$  is the direct (nearest neighbor) coupling between carbon atoms in different sheets that are directly above each other. The upper left block matrix corresponds to one graphene sheet and the lower right to the other sheet. From this Hamiltonian one can determine the eigenstates and the eigenenergies. The four energies are given by

$$E = \pm \frac{\gamma_1}{2} \pm \frac{1}{2} \sqrt{\gamma_1^2 + (2\hbar v_F k)^2}, \quad (3.2)$$

using all possible four combinations of + and -. The boundary conditions for the state of lowest angular momentum [71] leads to a condition on the possible values of  $k$  and this condition can be expressed in terms of the areas of the unit cell and of the hole [71] leading to the following expression for the energies

$$\begin{aligned} E &= \pm \frac{\gamma_1}{2} \pm \frac{1}{2} \sqrt{\gamma_1^2 + 16\pi\hbar^2 v_F^2 A_{\text{hole}}/A_{\text{cell}}^2} \\ &= \pm \frac{\gamma_1}{2} \pm \frac{1}{2} \sqrt{\gamma_1^2 + E_{\text{g,ML}}^2}, \end{aligned} \quad (3.3)$$

where  $E_{\text{g,ML}} = 4\hbar v_F \sqrt{\pi A_{\text{hole}}}/A_{\text{cell}}$  is the monolayer bandgap and  $v_F$  is the Fermi velocity in graphene [20]. The bandgap in the bilayer case is given by

$$\begin{aligned} E_{\text{g,BL}} &= \left( -\frac{\gamma_1}{2} + \frac{1}{2} \sqrt{\gamma_1^2 + E_{\text{g,ML}}^2} \right) - \left( +\frac{\gamma_1}{2} - \frac{1}{2} \sqrt{\gamma_1^2 + E_{\text{g,ML}}^2} \right) \\ &= \sqrt{\gamma_1^2 + E_{\text{g,ML}}^2} - \gamma_1. \end{aligned} \quad (3.4)$$

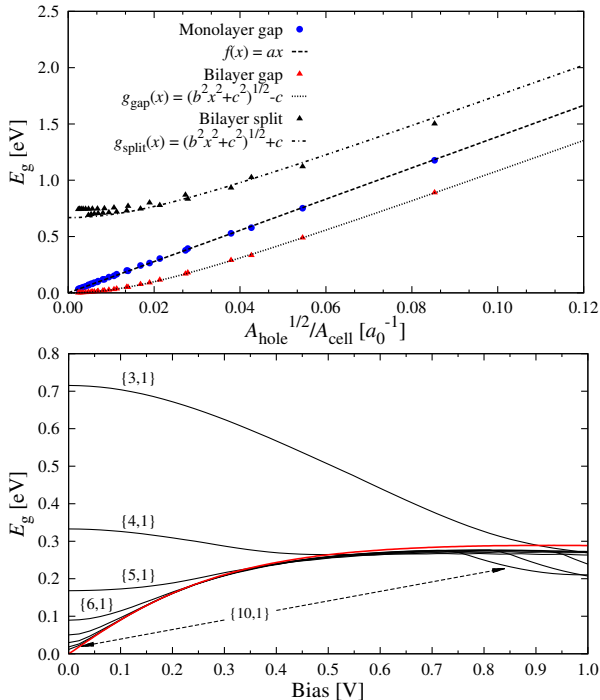


**Fig. 3.2:** (top) Comparison of the bandgap scaling in mono- and bilayer GALs. The dashed lines show the fitted analytical results, the circles show the TB monolayer gaps and triangles show the bilayer gaps. The black triangles show the gap between the lowest valence band and the highest conduction band. (bottom) Bandgap versus electric bias applied perpendicular to a bilayer GAL for a number of GAL geometries. (from [80])

As expected, in the case of zero coupling between atoms in different sheets  $\gamma_1 = 0$  eV, the bilayer gap reduces to the monolayer gap, and when the monolayer gap is zero, so is the bilayer gap.

In the top panel of Fig. 3.2, the result of a TB calculation of the bandgap for a number of bilayer GALs are shown along with a fitted curve of the form  $\sqrt{c^2 + b^2 A_{\text{hole}}/A_{\text{cell}}} - c$  based on Eq. 3.4. The parameters are found to be  $b = 13.78$  eV  $a_0$  and  $c = 0.34$  eV agreeing qualitatively with the values of the model  $b = 4\hbar v_F \sqrt{\pi} = 18.97$  eV  $a_0$  and  $c = 0.381$  eV. Quantitative agreement cannot be expected because the Fermi velocity is likely to be smaller in an antidot lattice than in pure graphene, and because the TB model includes effects that are ignored in the Dirac model such as skew coupling between atoms in different layers. Even so, the model predicts the correct bandgap scaling, which is seen to be fundamentally different from the monolayer case for small gaps. For large gaps the monolayer scaling is recovered. In this study only holes with armchair edges are considered. Holes with zig-zag edges deviate significantly from the bandgap scaling rule because the electrons in this case



are strongly confined to the edge of the hole, and this effect is not described by the boundary conditions used for the Dirac model treatment of GALs [71].

Biasing of bilayer graphene is easily modelled in TB by adding the potential  $V$  and  $-V$  on the diagonal of the block matrix representing the top sheet and bottom sheets, respectively. For pristine bilayer graphene this leads to an opening of the gap as seen from the red curve in the bottom panel of Fig. 3.2. For small  $V$  one has  $E_g \approx V$  while for large  $V$  the gap saturates at some value. If only the direct coupling  $\gamma_1$  between the layers is considered this value is exactly  $\gamma_1$  [37], but for the present TB model the value is different because also the skew coupling is included.

In the case of bilayer GALs a more complicated behavior is observed. For small  $A_{\text{hole}}/A_{\text{cell}}$  ratios the gap increases as a function of the applied bias as expected, but for large ratios the gap decreases when the applied bias is increased. This effect is somewhat unexpected, but has in fact been observed also in hydrogenated bilayer graphene [143].

## 3.2 Effective medium theory in graphene/hBN multilayer structures

In paper B, heterostructures composed of graphene and hexagonal boron nitride (hBN) were investigated with the aim of assessing the validity of effective medium theory (EMT) in these structures. EMT is typically based on the bulk permittivities of the constituent layers, in this case graphite and bulk hBN, so EMT may be expected to be a good description in between two limits: The optical limit where individual layers are made so thick that EMT breaks down because the long wavelength criteria is broken, and the quantum limit where the thickness of the layers is made so thin that the layer properties deviate significantly from their isolated bulk counterpart.

To investigate these two limits, structures of varying number of graphene and hBN sheets are considered. In the following, references to “sheets” mean monolayers, while references to “layers” mean a number of identical monolayers. Thus, a graphene/hBN heterostructure consists of a number of graphene and hBN layers, and each of these layers consists of a number of sheets.

To accurately describe the graphene/hBN heterostructures modelling using DFT based methods is preferred because DFT allows for accurate calculations of optical properties, especially if many body effects are included and the GW correction used. This, however, is a heavy calculation, in particular when the optical properties are demanded and the number of atoms increases. The calculations of this work involve too many atoms that DFT methods are feasible, and thus a TB model is adopted. Accurate TB models for the optical properties of graphene and graphite can be found in the literature [90], but it has not been possible to find a set of TB parameters for hBN that accurately de-

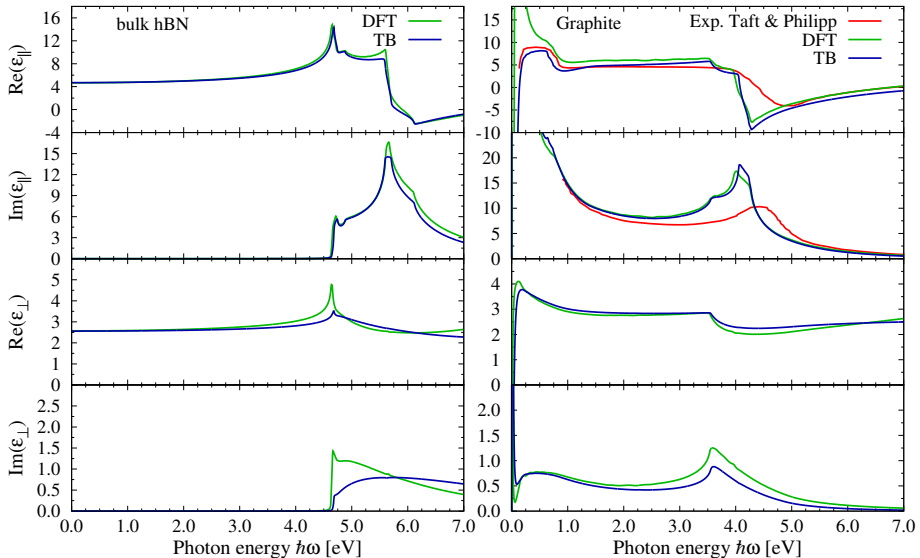


**Fig. 3.3:** Comparison of the in- and out-of-plane permittivity of graphene and hBN calculated in both DFT and TB. Experimental results are included for graphite in the in-plane case [144] (from [86]).

describes both the in- and out-of-plane response. Thus, to describe the hBN layers a set of TB parameters that accurately reproduces both the DFT band structure and the DFT based optical spectra has been determined. There is generally no guarantee that a good fit to the DFT band structure will give good correspondence between optical spectra also, since the band structure is determined entirely from the eigenvalues while the optical spectrum relies also on the eigenvectors. Thus, a good fitting procedure will fit also to the eigenvectors. Using the optimization toolbox of MATLAB a third nearest neighbor model including also the overlap of atomic orbitals has been fitted to a DFT calculation of the band structure and the optical spectrum, and the parameters can be found in Ref. [86]. In Fig. 3.3 the optical spectra calculated both from DFT and from TB are presented along with experimental results for graphite from [144], and it is seen that good agreement between TB and DFT has been obtained. Experimental results are included for the graphite in-plane response, but the out-of-plane response is difficult to measure reliably and significant disagreement is found in the literature [145].

### 3.2.1 Calculation of $\varepsilon$ using EMT and TB

In this section EMT is assessed by calculating the permittivity using EMT and the local-RPA formalism introduced in Sec. 2.2 to study the quantum limit of EMT. Periodic structures are considered (thus consisting of infinitely

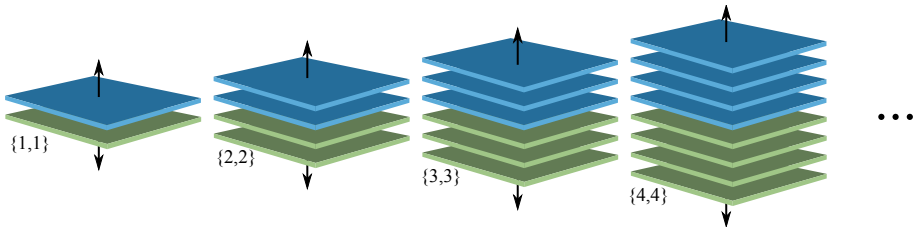


**Fig. 3.4:** Periodic graphene/hBN structures with the number of sheets in each layer increasing. The arrows indicate that the structure is repeated indefinitely.

many layers) as the number of sheets is gradually increased. This is depicted in Fig. 3.4, where the notation  $\{N, N\}$  is used to refer to periodic structures of alternating graphene and hBN layers with  $N$  sheets in each layer.

For a  $\{1, 1\}$  structure, EMT is expected to perform rather poor because the single sheets of graphene are not well described by the permittivity of graphite. That this is indeed the case, is seen from the top two panels of Fig. 3.5, where the convergence of  $\varepsilon_{\parallel}$  is studied for increasingly thicker layers. The  $\{1, 1\}$  structures behave much different from EMT and, contrary to what one might intuitively expect, basing EMT on monolayer permittivities is in fact not better at describing the  $\{1, 1\}$  structures. This is due to the coupling between carbon and boron, which gives the graphene sheets similar properties to what they have in graphite. This study shows that already for  $\{5, 5\}$  structures the permittivities calculated in EMT and the full TB model are almost indistinguishable.

For the perpendicular permittivity, the story is much different. In the bottom two panels of Fig. 3.5 the convergence study for  $\varepsilon_{\perp}$  is shown, and it is seen that  $\varepsilon_{\perp}$  certainly does not converge to the EMT value. That this is so is not a huge surprise, since  $\varepsilon_{\perp}^{\text{EMT}}$  is calculated by averaging the reciprocals according to Eq. 2.51, and it is difficult to see how one would obtain this result from a calculation based on Eq. 2.15 which simply adds the contributions of all possible transitions. The reason is that the linear response theory on which Eq. 2.15 is based, is simply not correct for the calculation of optical properties of heterostructures because it assumes the perturbing field to be constant throughout the entire structure. This is obviously not a problem when calculating the in-plane response, because in this case the electric field is in fact constant throughout the entire structure as dictated by the Maxwell boundary condition given in Eq. 2.22. However, it is clear from the boundary conditions that the perpendicular component of the electric field is not continuous throughout the heterostructure but “jumps” in proportion with the ratio between the individual permittivities. Thus, the basic assumption of the framework leading to Eq. 2.15 is broken explaining the discrepancy in the bottom two panels of Fig. 3.5.

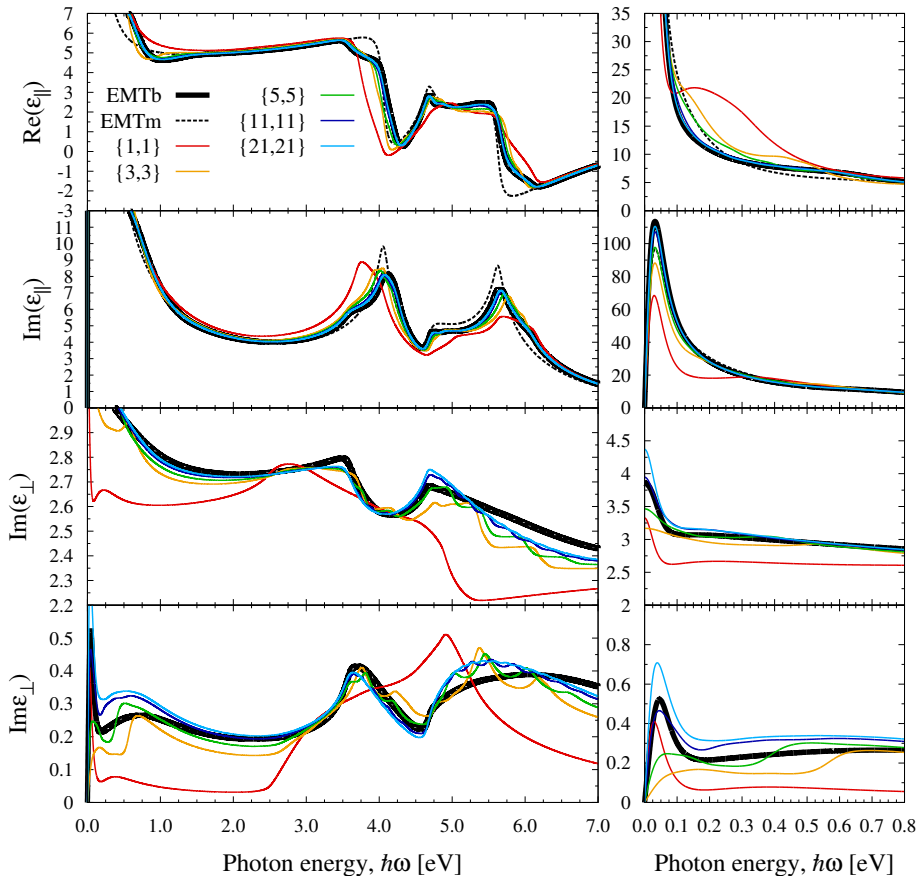


**Fig. 3.5:** The top two panels show the real and imaginary part of  $\epsilon_{\parallel}$  for increasingly thicker layers, and the bottom two panels show the real and imaginary part of  $\epsilon_{\perp}$ . The right panels show a zoom on the low energy region. Two EMT models are shown: EMTb, based on bulk permittivities and EMTm, based on monolayer permittivities.(from [86])

### 3.2.2 Calculation of $r^P$ using TMM based on EMT and TB

To remedy this and enable studying the convergence of the out-of-plane permittivity to the EMT value, the field variation throughout the structure is taken into account by using the transfer matrix method (TMM). As described in Sec. 2.3, the TMM is a method for calculating the fields in all layers of a layered structure and therefore any property calculated using this method will have the field variation taken into account. The TMM does not allow calculation of the stack permittivities, but rather of the reflection or transmission coefficient of the stack. Thus, the reflection coefficient is calculated for finite structures of

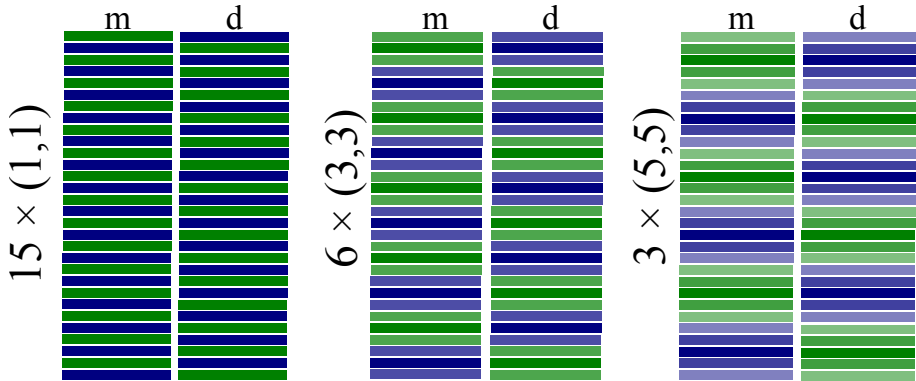


**Fig. 3.6:** Illustration of the structures used for TMM calculations. The total number of layers is constant in all structures and the reflection coefficient is calculated as an average between structures with metallic (m) and dielectric (d) top layer. The different shade of sheets within the same layers indicates that each sheets have a distinct permittivity due to different atomic environments.

the form  $M \times (N, N)$ , that is, the stack composed from stacking  $M$  copies of a *finite*  $(N, N)$  structure on top of each other, treating each sheet as a layer in the TMM. This is illustrated in Fig. 3.6, where three different stacks denoted as  $15 \times (1, 1)$ ,  $6 \times (3, 3)$ , and  $3 \times (5, 5)$ , all with a total of 30 sheets, are shown. Now, it is expected that the out-of-plane permittivity of each layer converge to the bulk value as the number of sheets is increased. If this is so, the reflection coefficient of the entire stack should gradually converge to the EMT reflection coefficient provided that the EMT calculation is comparable to the TMM calculation. There are two important points to be considered for this to be true: The choice of the top layer which has meaning only in the TMM calculation and the total thickness of the stack. The choice of top-layer is important as it has been shown in [87], and in order to take this into account the reflection coefficient is calculated as an average between a stack with graphene on top and one with hBN on top. The total thickness of the layer is kept constant throughout all calculations by considering only structures for which the number of sheets  $2MN$  is equal to 420. This number is chosen because it allows for many different combinations of  $M$  and  $N$ , so as to allow for a meaningful convergence study with several intermediate steps. For the EMT calculation only the thickness of the entire structure enters and this is chosen to be  $420c_0$  with  $c_0 = 3.35 \text{ \AA}$  being the sheet thickness [49, 53].

To actually do the TMM calculation, the permittivity of each single sheet is needed. This is obtained by using the formalism introduced in Sec. 2.5 to extract the single sheet conductivities from a calculation of a periodic  $\{N, N\}$  structure, and then using Eq. 2.7 to calculate the permittivity. In Fig. 3.6 the distinct permittivities of the individual sheets in the entire structure are

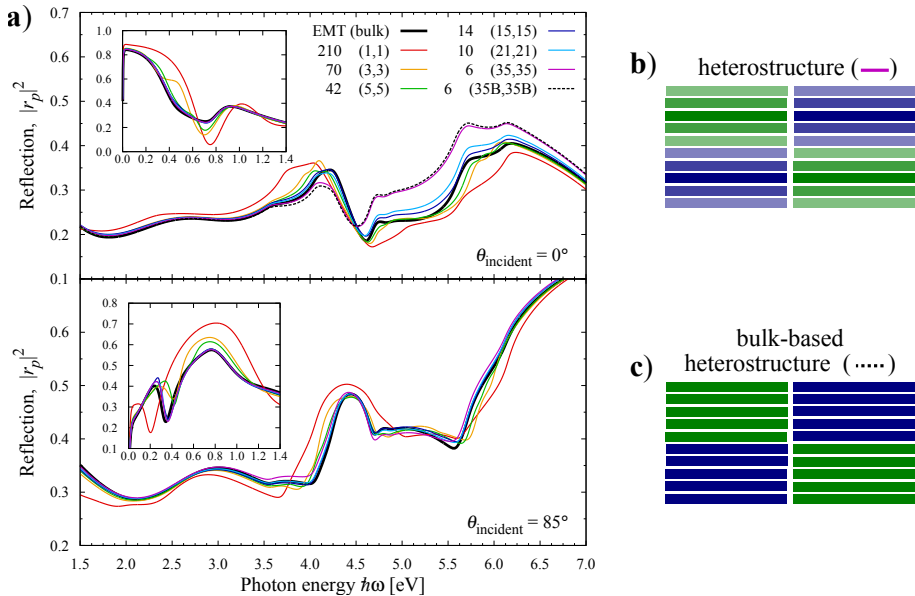


**Fig. 3.7:** **a)** Convergence in the reflection spectrum for increasingly thicker layers with the graphitic part doped to  $E_F = 0.5$  eV. The dashed curve referred to as  $6 \times (35B, 35B)$  in the legend shows the reflection based on layers described by bulk permittivities. **b)** and **c)** Illustration of the kind of structures used for the  $6 \times (35, 35)$  and  $6 \times (35B, 35B)$  calculations (the structure shown here are  $2 \times (5, 5)$  and  $2 \times (5B, 5B)$ ). (from [86])

illustrated using colors of different shades. For simplicity, edge effects are considered only on boundaries between layers graphene and hBN layers but not on the boundary between the metamaterial and air. This would in principle be possibly within the used framework, but it would be a very heavy calculation due to the large number of atoms involved.

The results of the TMM calculation is shown in Fig. 3.7a for two angles of incidence  $\theta_{\text{incident}} = 0^\circ$  and  $85^\circ$  and with the graphene doped to a Fermi level  $E_F = 0.5$  eV. From Eq. 2.39 it is clear that the influence of the out-of-plane permittivity is dependent on the angle of incidence, and so to actually probe  $\varepsilon_\perp$  large incident angles should be considered. Again, one should bear in mind that it is the path of light *in* the material that counts and even at an incident angle of  $85^\circ$  the parallel component of the permittivity tensor could play a significant role due to refraction. From the figure it is clear that the reflection based on  $\{1, 1\}$  structures differs significantly from the EMT based reflection in the entire spectral range shown. Considering the difference in the dielectric constant apparent from Fig. 3.5 this is not surprising. For increasingly thicker layers convergence is reached for energies below  $\approx 4$  eV approximately for the  $14 \times (15, 15)$  structures for both angles of incidence. For higher energies, significant deviations that get only worse as the layer thickness is increased are seen.

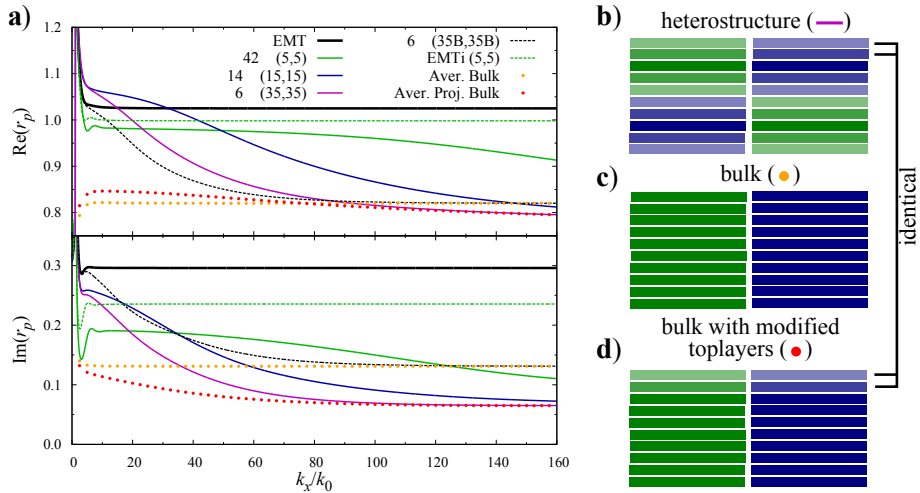


**Fig. 3.8:** a) Convergence in the reflection spectrum for  $\hbar\omega = 0.3$  eV for evanescent waves of increasing  $k_x$ . EMTi is improved EMT. The orange dots represents the average of the reflection coefficient from a stack of graphite and bulk hBN. The same for the red dots, except that the 17 topmost layers are based on the projected permittivities from a  $\{35,35\}$  structure. b - d) Illustration of the kind of structures used for  $6 \times (35, 35)$ , “Aver. Bulk” and “Aver. Proj. Bulk”, coloring is the same as in Fig. 3.7. (from [86])

Since these deviations exist only for high energies, that is, small wavelengths, one might suspect that the EMT criterion that the wavelength should be much larger than the period of the structure is broken at these energies, and multiple reflections throughout the structure contribute significantly to the overall reflection. To test this hypothesis the reflection is calculated for a layered structure composed of graphite and bulk hBN denoted as  $6 \times (35B, 35B)$ , thus being identical to the  $6 \times (35, 35)$  structure except that bulk permittivities are used instead of those based on projected permittivities, see Fig. 3.7b and c. If the deviations are in fact due to multiple reflections, and if the permittivity has converged, the reflection should be very similar to the  $6 \times (35, 35)$  reflection. From Fig. 3.7 where the dashed line represents the  $6 \times (35B, 35B)$  reflection this is seen to be the case. For the case of  $\theta_{\text{incident}} = 85^\circ$  the same pattern is followed, but the effects of multiple reflections play a much smaller role which is exactly what one would expect when the angle of incidence is increased. For low energies where these effects have only a weak influence, convergence is reached for the  $14 \times (15, 15)$  structure. Thus, it can be concluded that convergence in both components of the permittivity tensor is reached and that EMT provides an accurate description provided the layers are thin enough that reflection off the layer boundaries can be ignored.

In Fig. 3.7 the reflection was studied only for the propagating wave components  $k_x \leq k_0$ . In the near field of an oscillating electric dipole there will

be non-propagating modes of  $k_x > k_0$  and so it is of relevance to study also the performance of EMT for these modes. There is good reason to be skeptical about the performance of EMT in this case, because large  $k_x$  generally leads to a large imaginary component of  $k_z$  in the stack layers, thus limiting the penetration depth of such modes. Thus, even if the wavelength is large enough to fulfill the wavelength criterion, the limited penetration depth could lead to the failure of EMT. In Fig. 3.8a the reflection coefficient is shown for large values of  $k_x$  and it is clear that EMT is a bad description already for  $k_x/k_0 \gtrsim 2$ . EMT tend to severely overestimate the reflection coefficient. One might expect multiple reflections to be the explanation as it was the case for  $k_x < k_0$ . Comparing the reflection from  $6 \times (35, 35)$  with the reflection from  $6 \times (35B, 35B)$  shows that the reflection in this case does indeed get closer for small to moderate values of  $k_x$ , but one quickly realizes that this cannot be the whole explanation since the limiting value for large  $k_x$  is different from the EMT value. That the explanation might lie in the limited penetration depth as it has already been mentioned, is suggested by looking at the orange dotted curve. This result is obtained by simply calculating the reflection from two samples of graphite and hBN both of thickness  $420c_0$  and averaging the two. The real part of the reflection calculated in this way is somewhat closer to the  $6 \times (35, 35)$  heterostructure for large  $k_x$  but the imaginary part is still off. In the limit of large  $k_x$  only a few of the top sheets contribute to the reflection because the propagation depth will be very small. In the heterostructure the top layers are not bulk layers, because they sit in a different atomic environment than the bulk layers, see Fig. 3.8b. Doing again a calculation of the reflection by averaging the reflection from two bulk calculations, but with the top layers replaced by the value used in the heterostructure, see Fig. 3.8d, one gets the red dotted line shown in Fig. 3.8a, and it is clear that this calculation has exactly the correct limiting behavior. This proves that the effects the top layers are of huge importance for the modes of large  $k_x$ , and thus that EMT in this case is unreliable.

### 3.2.3 Doped structures

In the left panel of Fig. 3.9 the equivalent of the top two panels of Fig. 3.5 is shown in the energy range 0 to 1.5 eV, but with the graphene part doped to 0.5 eV. The convergence is somewhat slower in the low energy region and in particular for doped structures. As such, an improved EMT (EMTi) has been suggested that provides quicker convergence for layered structures. The idea is to include in the averaging not only the bulk permittivities, but also an intermediate “transition” layer, which accounts for the different environment seen by the sheets just at the boundary between two layers. The EMTi permittivities



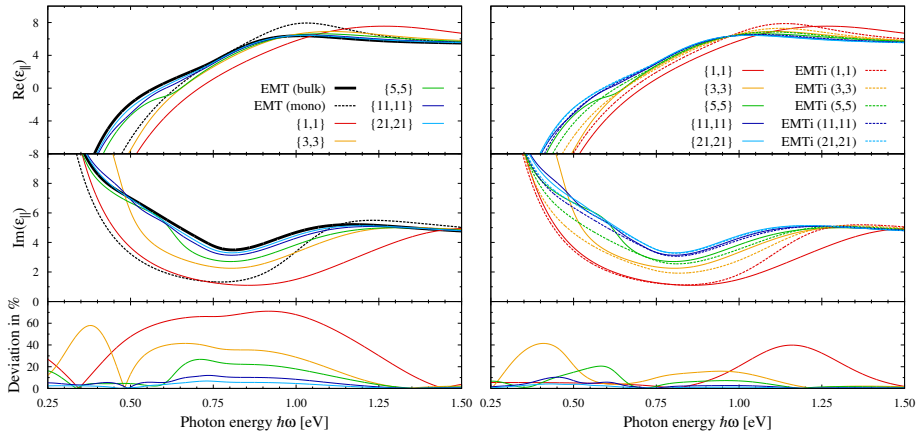


**Fig. 3.9:** The left panel shows the convergence of  $\varepsilon_{\parallel}$  to EMT for periodic structure with increasingly thicker layers with the graphene part doped to 0.5 eV. The right part shows the convergence to EMTi (improved EMT) under the same conditions. The bottom panel shows the deviation from EMT and EMTi in percent. (from [86])

are accordingly calculated from

$$\begin{aligned} \varepsilon_{\parallel}^{\text{EMTi}} &= \rho_m \varepsilon_m + \rho_d \varepsilon_d + (1 - \rho_m - \rho_d) \varepsilon_{\text{interface}}, \\ \frac{1}{\varepsilon_{\perp}^{\text{EMTi}}} &= \frac{\rho_m}{\varepsilon_m} + \frac{\rho_d}{\varepsilon_d} + \frac{1 - \rho_m - \rho_d}{\varepsilon_{\text{interface}}}, \end{aligned} \quad (3.5)$$

with  $\rho_m$  and  $\rho_d$  being the fractions of metal and dielectric, respectively, and  $\varepsilon_{\text{interface}}$  the permittivity of the interface layer.  $1 - \rho_m - \rho_d$  is the fraction of interface layer in the structure. In the case of graphene/hBN structures, the interface layer consists of one layer of graphene and one layer of hBN. For a  $\{5, 5\}$  structure, for instance,  $\rho_m = \rho_d = 0.8$ . Using this method, the interface layer is included in the calculation if it is assumed that the layers above and below the interface layers are only weakly affected by the boundary.

In the right part of Fig. 3.9, the convergence to EMTi is shown and by looking at the deviations it is clear that EMTi certainly does offer improvement over ordinary EMT shown to the left for stacked heterostructures. To actually use this method access to the sheet permittivities is needed which makes the method less versatile than ordinary EMT where the ingredients in form of bulk permittivities are usually readily available. If however, strong coupling between interface layers is expected in a certain setup, the interface permittivity can be treated as a fitting parameter that may account for interface effects. In paper B, reflection spectra are provided showing the improvement also in the reflection spectra.

In Fig. 3.10, the Purcell enhancement is shown for all considered structures along with the Purcell factor calculated from EMT. It is clear that EMT in

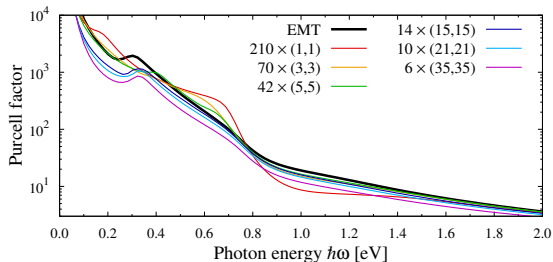


**Fig. 3.10:** Purcell factor of the graphene/hBN metamaterials of different compositions compared to EMT. (from [86])

all converged cases severely overestimates the Purcell factor, which should not be too surprising considering the discussion of EMT for modes of high  $k_x$  that are crucial to the Purcell factor calculation. EMT suggest that the structures considered are hyperbolic in the frequency range 50 to 600 meV and thus one should accordingly find the Purcell enhancement to be much greater in this regime. It is obvious that no clear features are observed in the Purcell factor for these energies. The reason for this is the huge losses in the graphitic part of the materials for low energies which by itself causes the Purcell factor to be large. Thus, features in the Purcell factor related to the hyperbolic modes are blurred by the losses.

### 3.3 Natural hyperbolic materials

In paper C, the dielectric properties of 31 different metallic or semiconducting layered transition metal dichalcogenides (TMDs) were investigated using density functional theory (DFT) with the Perdew-Burke-Ernzerhof (PBE) exchange-correlation (xc) functional, to calculate the components of the dielectric tensor, starting from the experimentally determined crystal structure of the compounds [148] (see Fig. 1.6 for the crystal structure of TMDs). This allows classification of the materials according to spectral regions of hyperbolic dispersion ( $\epsilon_{\parallel}\epsilon_{\perp} < 0$ ) and as exhibiting either type I or type II hyperbolic behavior.

In Fig. 3.11, the result indicating the hyperbolic regimes for all 31 TMDs is shown along with experimental results for graphite, MoS<sub>2</sub> and ZrS<sub>2</sub> marked with red squares. All 31 TMDs were found to exhibit predominantly type II hyperbolic dispersion (metallic response in-plane and dielectric response out-of-plane) in a wide spectral range covering the mid-IR to the UV. The relatively good agreement with experiment suggests that the results can be at least qualitatively trusted. Unfortunately, experimental studies probing both the in- and out-of-plane response are sparse and instead the regimes of negative in-plane di-

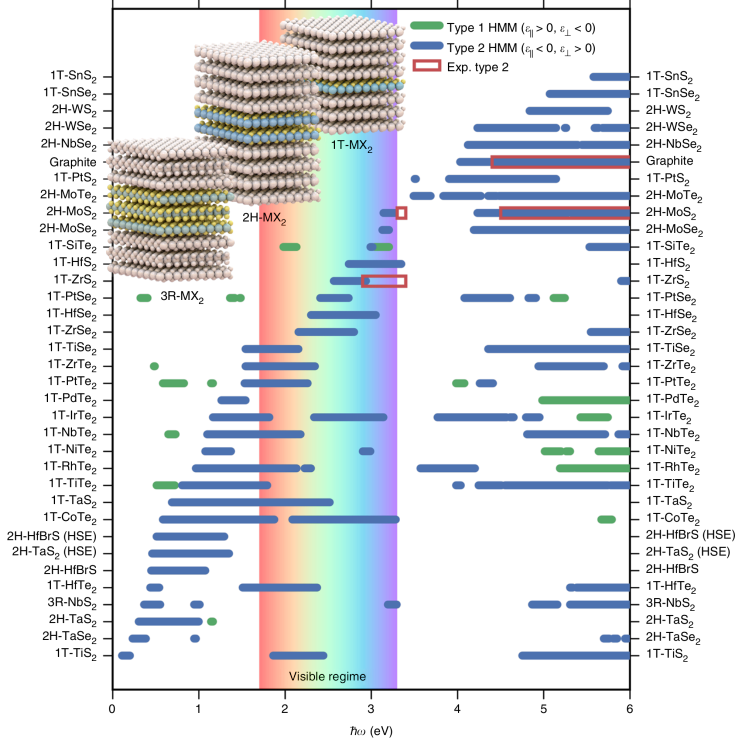


**Fig. 3.11:** Hyperbolic regimes of 31 TMDs along with experimentally extracted results from [144] (graphite), [146] ( $\text{MoS}_2$ ) and [147] ( $\text{ZrS}_2$ ). The investigated materials are predominantly type II hyperbolic materials. (from [93])

electric constant, a good indicator of a type II hyperbolic material, have been compared to experiments [149–151] and the accuracy found to be  $\sim 0.5$  eV. To further strengthen the confidence in the DFT results, the two compounds  $\text{HfBrS}$  and  $\text{TaS}_2$  are investigated using also the more accurate but computationally expensive HSE xc-functional [152], and it is found that the hyperbolic spectral range is blue shifted by  $\sim 0.2$  eV, a tendency which is expected also for the other materials.

Natural hyperbolic materials are interesting due to the lack of internal structure and hence the ability to support hyperbolic modes of much larger wave vector than the artificially structured metamaterials that are hampered by the metamaterial period  $d$  limiting the supported wave vectors to  $k_{\max} \sim \pi/d$ , as discussed in the introduction. The Purcell factor is strongly dependent on modes of large wave vectors and consequently makes an excellent figure of merit for comparing natural and artificial hyperbolic materials. In Fig. 3.12a, the Purcell factor calculated for a metamaterial consisting of layers of silver and  $\text{SiO}_2$  both with a thickness of 10 nm and thus, a period of 20 nm, is calculated

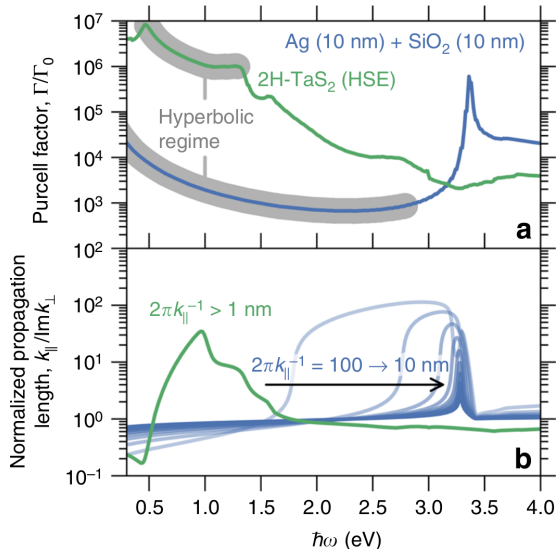


**Fig. 3.12:** (a) Comparison of the Purcell factor and (b) the propagation length of electromagnetic modes in a silver/SiO<sub>2</sub> metamaterial and the natural hyperbolic material TaS<sub>2</sub>. (from [93])

using the TMM and compared to the Purcell factor of TaS<sub>2</sub>, a natural hyperbolic material. In the silver/SiO<sub>2</sub> metamaterial the Purcell factor is orders of magnitude smaller than in TaS<sub>2</sub> even in the region where EMT predicts the metamaterial to be hyperbolic, while the hyperbolic character of TaS<sub>2</sub> has a clear enhancing effect on the Purcell factor. In traditional planar metamaterials the broadband hyperbolic response is caused by hybridization of surface plasmons on the interfaces. Therefore, the broadband response is heavily relying on sufficient spatial overlap of plasmons, a condition that is hardly fulfilled in the shown silver/SiO<sub>2</sub> structure because of strongly decaying fields inside the silver layers [153]. Thus, the hyperbolic character predicted by EMT does not manifest itself in a TMM calculation where the field propagation within each layer is properly accounted for. The peak seen for the metamaterial at  $\sim 3.3$  eV is due to the unhybridized plasmons in silver.

The metallic TMDs investigated in this work all has the unique feature of being hyperbolic below the onset of interband absorption, thus allowing for weakly damped propagating hyperbolic modes that lead to high Purcell factors. TaS<sub>2</sub>, in particular, entails a special band structure with isolated metallic bands causing low losses due to the absence of interband transitions normally giving rise to strong absorption [100]. The clear signature of the hyperbolic region in the Purcell factor is a consequence of low losses, because absorption by itself leads to Purcell enhancement thereby blurring the signature of the hyperbolic dispersive modes. Another indicator of low losses is the propagation length of

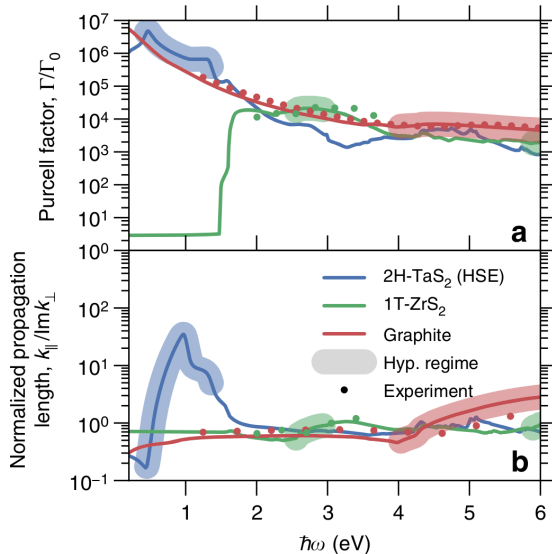


**Fig. 3.13:** (a) Comparison of the Purcell factor and (b) the propagation length of electromagnetic modes in the natural hyperbolic materials graphite, TaS<sub>2</sub> (metal) and ZrS<sub>2</sub> (semiconductor,  $E_{\text{gap}} \sim 1.5$  eV). For graphite and ZrS<sub>2</sub> the high Purcell factor is due to interband absorption, while for TaS<sub>2</sub> it is caused by the low loss hyperbolic modes. (from [93])

electromagnetic modes. In Fig. 3.12b the propagation length normalized by the in-plane wavelength is shown for TaS<sub>2</sub> and for the silver/SiO<sub>2</sub> metamaterial and the much longer propagation length in TaS<sub>2</sub> compared to the metamaterial due to low losses and hyperbolic dispersion is clearly seen. In fact, the propagation lengths in the metamaterial rarely exceed unity except for in-plane wavelengths much longer than the metamaterial periodicity, and this is the case even within the hyperbolic region where the modes are propagating within the structure.

Among the TMDs shown in Fig. 3.11 are both metals and semiconductors and in Fig. 3.13 a comparison between the Purcell factor and the propagation lengths of the semiconducting TMD ZrS<sub>2</sub> and the metallic TMD TaS<sub>2</sub> is shown including also the results for graphite. ZrS<sub>2</sub> shows large Purcell enhancement only above its bandgap of  $\sim 1.5$  eV where the material is not hyperbolic, thus clearly indicating that large Purcell enhancement in this case is not dictated by hyperbolic dispersion but is rather purely due to absorption losses that are present only for energies above the onset of interband transitions. The hyperbolic range between  $\sim 2.4$  and  $\sim 3.1$  eV entails only a weak enhancement in addition to that already present due to losses. This effect is severe also in graphite where the Purcell enhancement seems to be uncorrelated with the hyperbolic region, something that was seen also in connection with Fig. 3.10 where no clear correlation with the hyperbolic regime was seen.

In order to have strong enhancement solely within the hyperbolic region, the

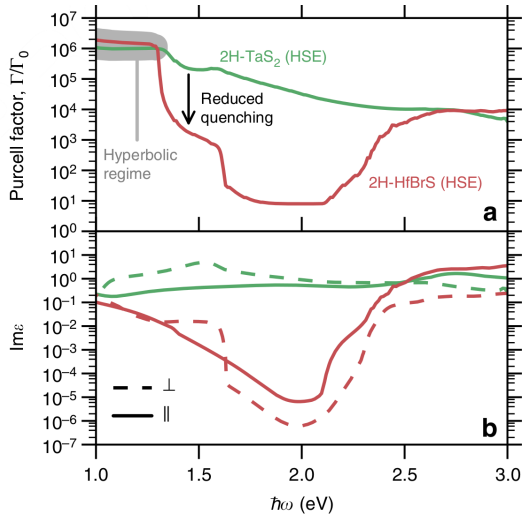


**Fig. 3.14:** (a) Comparison of the Purcell factor of the materials HfBrS and TaS<sub>2</sub> and (b) the imaginary part of their dielectric constant measuring absorption losses. HfBrS shows a clear drop in Purcell enhancement outside the hyperbolic region contrary to TaS<sub>2</sub> where the drop is less pronounced because the Purcell factor remains high due to absorption. (from [93])

material losses, as quantified by the imaginary part of the dielectric constant, should be small. Recently, the chalcogen-halogen mixed compound HfBrS was identified as such a low loss material [100]. This material features a single metallic band that is isolated from higher and lower lying bands by gaps that are sufficiently large as to separate intraband from interband losses. In this case, a low-loss energy regime opens up and in HfBrS it coincides with the regime of hyperbolic dispersion. In Fig. 3.14a the Purcell factor of this material is compared to the Purcell factor of TaS<sub>2</sub> and in Fig. 3.14b the imaginary part of the corresponding dielectric constants of the materials are shown. Clearly, the hyperbolic region HfBrS shows huge Purcell factors that drop abruptly for frequencies where the material cease to be hyperbolic, while for TaS<sub>2</sub> the Purcell factor remains high. The correlation with the material losses is strong and the Purcell enhancement in HfBrS increase again above  $\sim 2.1$  eV with the material losses.

With the rather versatile selection of TMDs that has been shown to exhibit hyperbolic behavior, it is natural to try and combine different TMDs into van der Waals heterostructures and calculate their optical properties by using EMT, thus neglecting the plasmon hybridization as well as quantum confinement effects. Referring to the results of paper B, quantum effects should have negligible influence even when as few as  $\sim 5$  layers are stacked. Suppose that a metamaterial with hyperbolic dispersion in the range 1.5-2.0 eV and elliptical dispersion in the range 2.0-2.5 eV is desired. In this case one can define a figure

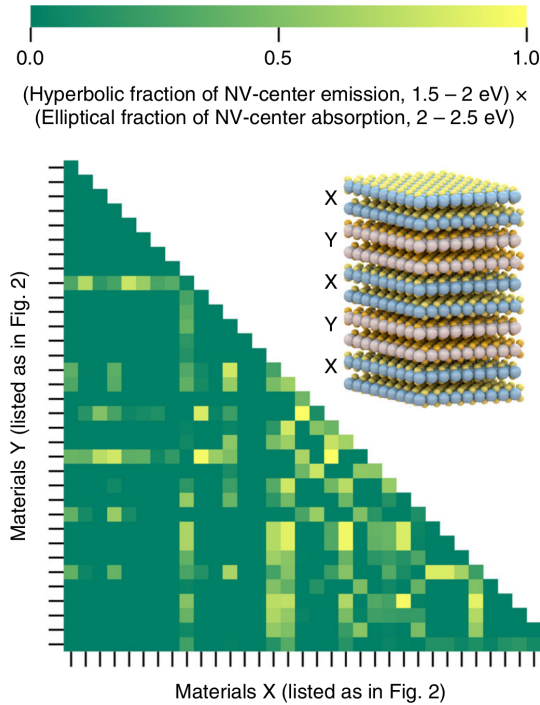


**Fig. 3.15:** (Heterostructures of different TMDs with the aim of obtaining a combination with hyperbolic dispersion in the range 1.5-2.0 eV and elliptical dispersion in the range 2.0-2.5 eV. The same ordering of the materials as in Fig. 3.11 is used. (from [93])

of merit as

$$(\text{Hyp. fraction in range 1.5-2.0 eV}) \times (\text{Ellipt. fraction in range 2.0-2.5 eV}), \quad (3.6)$$

and calculate this figure of merit for different combinations of TMDs. In Fig. 3.15 the result of such a calculation combining two different TMDs with a fill fraction of 50% is shown. The diagonal of the figure corresponds to the pristine TMDs while all other points correspond to heterostructures. Quite a few good candidates are found, showing the strengths of heterostructuring to obtain the desired properties. Even higher flexibility can be obtained by allowing the fill fraction to differ from 50% or by combining three or more different materials.

### 3.4 Optically activated plasmons in 2D materials

The aim of the work of paper D is to investigate plasmons in doped and heated graphene, MoS<sub>2</sub> and black phosphorus. The dielectric function  $\varepsilon(\mathbf{q}, \omega)$ , where  $\hbar\mathbf{q}$  is the momentum and  $\hbar\omega$  the energy of the exciting light, of the materials

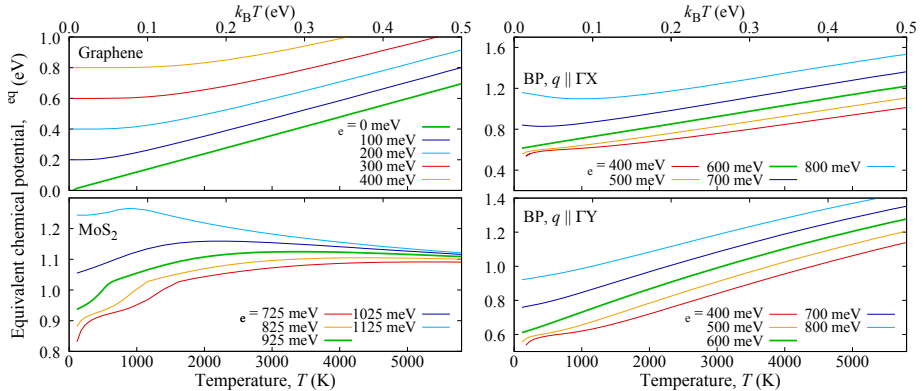


**Fig. 3.16:** Chemical potential  $\mu$  that gives the same plasma frequency as a specific choice of the electron chemical potential  $\mu_e$  and the temperature  $T$ . The thick green lines mark  $\mu_e = E_c$ , the equivalence used to produce the rest of the results in this work.

is determined using both the local- and the nonlocal-RPA (in the local-RPA  $\varepsilon$  does not depend on  $\mathbf{q}$  and is called the dielectric constant) to allow also for an investigation of the importance of nonlocal effects in these materials. Graphene is described using the simple nearest neighbor TB model with  $\gamma = 3.033$  eV. For MoS<sub>2</sub> the model of Ref. [154] that includes up to third nearest neighbor interactions and reproduces well the GGA-DFT band structure is employed. Black phosphorus (BP) is described using the simplified two-band model of Ref. [118] which describes well the strong crystal anisotropy and is accurate at low energies up to  $\sim 0.5$  eV from the band edges. The atomic structure of MoS<sub>2</sub> and BP is shown in Fig. 1.6.

### 3.4.1 Doping/pumping equivalence

Optically activated plasmons are plasmons activated by heating of the electrons in a material using a light pulse. In their intrinsic state, graphene and the semiconductors MoS<sub>2</sub> and black phosphorus do not support plasmons due to the lack of free charge carriers, but they can be activated either by doping or by increasing the electronic temperature by optically pumping the materials as it has been described in Sec. 1.2.4. Doping and pumping are both ways of creating free charge carriers in the materials, and as such, they lead to similar material response with the exception that pumping in many cases broadens the response. Therefore, doping and pumping are fully comparable provided that they lead to the same plasma frequency  $\omega_p$ .

The plasma frequency can be easily calculated using Eq. 2.19 for a number of different pumping conditions. In this work pumping is described by the temperature  $T$  and the electron chemical potential  $\mu_e$  and these two parameters are determined by the exact nature of the pumping process.



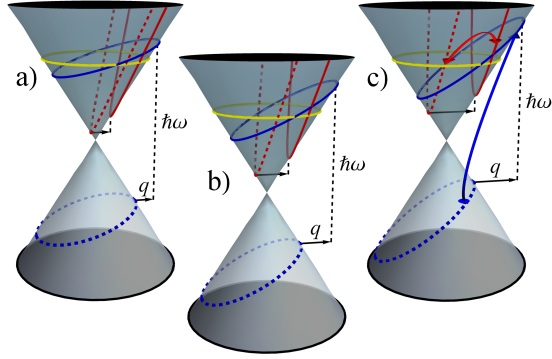


**Fig. 3.17:** Non-vertical transitions in the Brillouin zone illustrated for graphene. Red lines illustrate intraband transitions, blue lines interband transitions and the ellipse the Fermi level. For increased  $q$  intraband transitions from below the Fermi level and interband transitions of energy  $\hbar\omega < 2E_F$  are possible.

Since the electrons excited into the conduction band by the pump pulse are coming from the valence bands, one must require the number of electrons in the conduction bands to equal the number of holes in the valence bands. In order for this to be possible, the distribution of holes in the valence bands follows a separate Fermi-Dirac distribution of the same temperature as the electrons but distinct chemical potential  $\mu_h$ .  $\mu_h$  is determined from the equation

$$\int_{E_c}^{\infty} D(E) f_e(E) dE = \int_{-\infty}^{E_v} D(E) f_h(E) dE, \quad (3.7)$$

where  $D(E)$  is the density of states,  $f_e(E)$  and  $f_h(E)$  are the Fermi occupation factors for electrons and holes, and  $E_c$  and  $E_v$  are the conduction and valence band edges, respectively. For materials with electron/hole symmetry, such as graphene,  $\mu_e = -\mu_h$  but in general  $\mu_e$  will be different from  $-\mu_h$ .

Having calculated  $\omega_p$  for some pair of  $T$  and  $\mu_e$  it is a simple numerical exercise to find the equivalent electron doping level  $\mu^{eq}$  at room temperature (commonly referred to as the Fermi level) that gives the same  $\omega_p$ . In Fig. 3.16 the results of these calculations are shown for five different values of  $\mu_e$  with the value  $\mu_e = E_c$  used for all subsequent calculations highlighted using green thick lines.

In the case of graphene, the result agrees with what one would find in a simple analytical treatment with linearized bands near the  $K$  point [108]. For  $\text{MoS}_2$  it may be a bit surprising to see that  $\mu^{eq}$  decreases above a certain temperature, but this is due to the relatively complicated band structure of  $\text{MoS}_2$  (see Fig. 3.18b). The maximum attainable  $\omega_p$  by doping in  $\text{MoS}_2$  is for  $\mu = 1.32$  eV such that for some combinations of  $\mu_e$  and  $T$  it will not be possible to find an equivalent doping to match the plasma frequency.

Since black phosphorus is a strongly anisotropic material, the response depends on the direction of the perturbing electric field. Therefore, in the figure the equivalence is shown for the field polarized along both directions in the Brillouin zone. For BP there is no upper limit to  $\omega_p$  due to the simplified model used. The equivalence for  $\mathbf{q} \parallel \Gamma X$  resembles the case of graphene because in this direction the bands in BP are approximately linear (see Fig. 3.18c).

It should be noted that the equivalence is determined based on the local-RPA formalism, but used also for calculations within the nonlocal-RPA formalism where the conductivity depends on both the energy  $\hbar\omega$  and the momentum  $\hbar q$ . This is strictly not correct, but it is used as an approximation.

### 3.4.2 Plasmon dispersion

Having established the equivalence between doping and pumping the plasmon dispersion relation can be easily determined. Often the dispersion is determined from the maxima of the loss function given by imaginary part of the nonlocal-RPA dielectric function  $-\text{Im}\{\varepsilon(\mathbf{q}, \omega)^{-1}\}$ . These maxima can be found by determining the solutions to  $\varepsilon(\mathbf{q}, \omega) = 0$ . It can be shown that an alternative loss function that yields the same plasmon dispersion relation can be constructed from the imaginary part of the reflection coefficient for p-polarized light,  $r^p$  [155], which for a 2D material in the electrostatic limit ( $k_z \approx iq$ ) is given by

$$r^p = \frac{1}{1 - 2i\varepsilon_0\omega/(q\sigma(\omega, \mathbf{q}))} \quad (3.8)$$

where  $\sigma(\omega, \mathbf{q})$  is the 2D sheet conductivity. The conductivity is calculated within the nonlocal-RPA formalism introduced in Sec. 2.2. Contrary to the local-RPA, this formalism includes also the non-vertical transitions in the Brillouin zone. This allows intraband transitions (transitions within the same band) of any energy  $\hbar\omega > 0$  and therefore also transitions starting from below the Fermi level, which are not possible in the local-RPA. Also, interband transitions in the energy regime  $\hbar\omega < 2E_F$  are not possible in the local-RPA due to Pauli blocking, but in the nonlocal-RPA these transitions become allowed when  $q$  is increased. This is illustrated in Fig. 3.17 for three different values of  $q$ . Non-vertical transitions may happen if the exciting light carries high momentum. For light propagating in air the momentum is very small and will not be able to inflict the non-vertical transitions that require a substantial momentum change of the involved electrons. However, evanescent light components such as those present on the air side of a prism during total internal reflection or in the near field of an electric dipole may carry significant momentum and may cause non-vertical transitions to take place.

In Fig. 3.18 the loss function is shown in a  $(q, \hbar\omega)$  plot for graphene, MoS<sub>2</sub>, and black phosphorus in the intrinsic case, for doping and for pumping in the

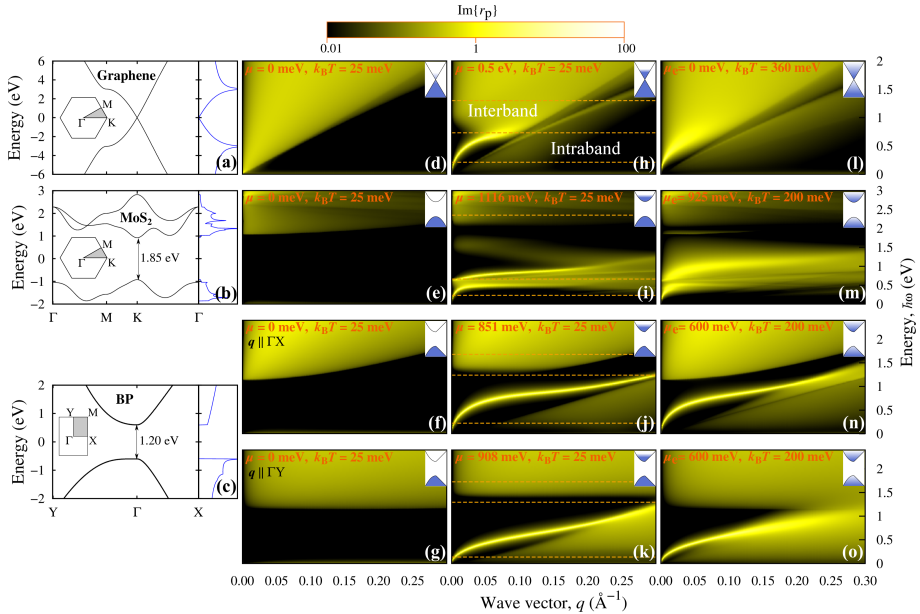


**Fig. 3.18:** Dispersion relations of plasmons in the nonlocal-RPA and for (d-g) intrinsic, (h-k) electrically doped, and (l-m) optically pumped graphene, MoS<sub>2</sub> and black phosphorus. (a-c) shows the band structure and density of states of the materials.

nonlocal-RPA. For doped graphene (Fig. 3.18h), the regime of Pauli blocking is clearly seen at  $q = 0$  where the losses are weak for  $\hbar\omega < 2\mu$ , but for  $q > 0$  losses increase even below the threshold of Pauli blocking. For doped graphene the well-known plasmon dispersion relation is clearly seen [108]. For graphene at increased temperature (Fig. 3.18l) the overall picture remains the same but with much stronger losses due to interband transitions. In doped graphene at low temperature interband transitions are only allowed above  $\sim 2\mu$  due to Pauli blocking and the almost step like Fermi function separating occupied from unoccupied states. However, for graphene at increased temperatures interband transitions may occur at any energy causing heavy broadening of the Plasmon resonances.

For MoS<sub>2</sub> plasmon resonances are also seen both for doping and for pumping. In MoS<sub>2</sub> in the pumping case a special feature arises around 2 eV that is not present in the doping case. This feature is due to population inversion and it causes the imaginary part of the reflection coefficient to be negative. This should be interpreted as negative losses, or gain, in the material and it has been suggested that such features may be exploited to balance plasmon losses [131]. For MoS<sub>2</sub> interband transitions also cause broadening of the plasmon modes in the pumping case due to transitions between the second and the third band. It is quite clear, that in order to avoid broadening of the plasmonic modes the

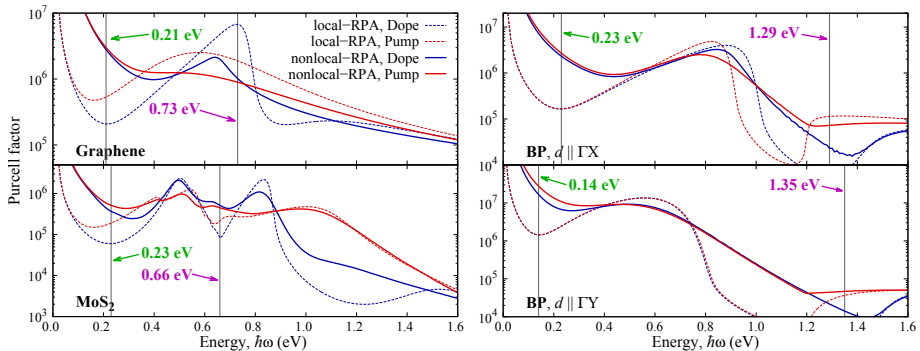


**Fig. 3.19:** Purcell factor energy dependence for all materials for a dipole located 1 nm from the surface, calculated in both the local-RPA and the nonlocal-RPA.

number of possible inter- and intraband transitions should be limited, and it is actually possible to identify materials of this kind exhibiting very low losses and consequently long plasmon propagation lengths as discussed in paper C.

For black phosphorus the loss function is shown for the two independent directions in the Brillouin zone corresponding to light polarized along the GX and ΓY directions. In the model employed here, losses are practically non-existing because the model includes only two bands and thus there can be no interband absorption losses below the bandgap. This is the reason for the striking similarity between doping and pumping. Some broadening is seen due to intraband transitions at increased  $q$ , and especially so for the ΓY direction because the density of accessible states when  $q$  is increased is higher in this direction. The broadening introduced in this manner corresponds to phonon or impurity assisted broadening where the electron momentum is increased to allow for non-vertical transitions.

### 3.4.3 Purcell enhancement

Knowing the material response and the reflection coefficient it is a simple matter to calculate the Purcell factor using Eq. 2.53. The Purcell factor is completely determined once the reflection coefficients for s and p-polarized light have been calculated. In the electrostatic limit, that is, for large  $q$  where  $k_z = \sqrt{\epsilon k_0^2 - q^2} \approx iq$  the formula Eq. 2.53 (using  $q$  instead of  $k_x$ ) reduces to

$$\frac{\Gamma}{\Gamma_0} = 1 + \frac{3}{4k_0^3} \int_{k_0}^{\infty} q^2 \text{Im}\{r_p(q)\} e^{-2qd} dq. \quad (3.9)$$

In Fig. 3.19, a comparison of the Purcell factor calculated in both the local- and the nonlocal-RPA and for doping and pumping is presented. For graphene in the local-RPA a peak is clearly seen at 0.73 eV which corresponds exactly

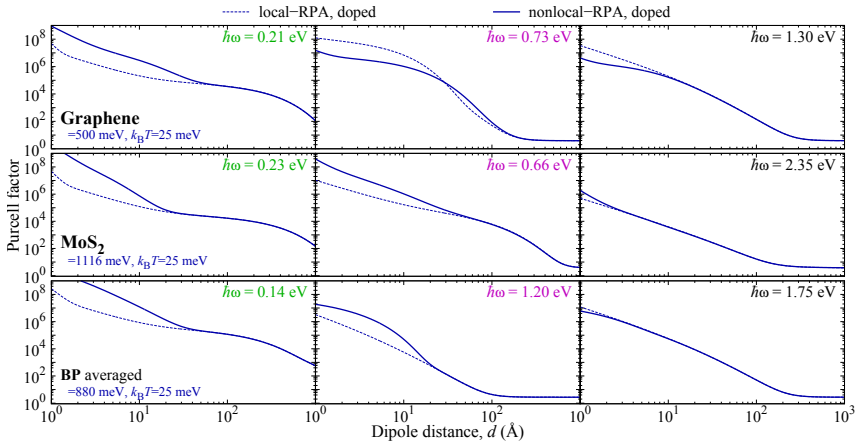


**Fig. 3.20:** Dependence of the Purcell factor on the dipole-surface distance  $d$ , calculated in both the local-RPA and the nonlocal-RPA.

to the plasmon energy at high  $q$ . In the local-RPA the plasmon is almost nondispersive at high  $q$  leading to the strong plasmonic response not seen in the nonlocal-RPA due to the  $q$  dependence of the dielectric function. Thus, when turning to the nonlocal-RPA, the peak is much less pronounced. A similar trend is seen for pumping where the plasmon peak has almost disappeared in the nonlocal-RPA. In the supplementary information of paper D the plasmon dispersion for the local-RPA is shown.

In MoS<sub>2</sub> in the doping case two clear peaks are seen and similar to the case of graphene, these peaks are weaker in the nonlocal-RPA. Again, these peaks stem from losses to plasmon modes. Contrary to graphene, one can in fact still find relatively strong peaks in the case of plasmons activated by optical heating, with peak to valley ratios of about 5. Thus, it might in fact be possible to measure the plasmonic contribution to the Purcell factor for optically pumped MoS<sub>2</sub>. For BP the difference between doping and pumping is much smaller due the aforementioned reasons of using only a two-band model.

To quantitatively measure the contributions of nonlocal effects in the studied materials it is natural to look at the dependence of the Purcell factor on the distance  $d$  between the dipole and the material. As the dipole gets farther away from the surface the evanescent wave components found in the near field of the dipole has to travel longer before they reach the surface. Thus, they will have decayed by a considerable factor such that their coupling to the surface is weakened, and their contribution to the dipole decay rate is decreased. Since this is true in particular for the wave components of high  $q$ , one would expect the local- and the nonlocal-RPA to agree when  $d$  is large while the limit of small  $d$  will be a measure for the importance of nonlocal effects.

In Fig. 3.20 the dipole decay rate as a function of the distance  $d$  to the

surface is shown for doping in both the local- and the nonlocal-RPA on a log-log scale for all materials and for three different energies. The energies marked by green and purple labels correspond to energies where intraband transitions constitute the main contribution to the response, while for the energy marked with black labels interband transitions is the main contribution. For large distances perfect agreement between the local- and nonlocal-RPA is seen, while for small distances the Purcell enhancement in the nonlocal-RPA is more than an order of magnitude larger than in the local-RPA. It is clear from the figure that intraband transitions are more heavily affected by nonlocal effects than interband transitions, since the agreement for the energies in the interband regime is much better for all materials.

# Chapter 4

## Conclusions

In this thesis 2D materials and heterostructures based on 2D materials have been investigated using tight binding (TB) and density functional theory (DFT) based modelling. TB allows for computationally inexpensive yet accurate calculations on large structures and this has been exploited to determine the electronic structure of both 2D and bulk structures on a relatively large scale. Based on the TB calculations linear response theory has been employed to determine the response functions of the materials. Because the used framework cannot be applied in structures where the electric field cannot be assumed constant, the transfer matrix method (TMM) has been applied to correctly calculate the reflection coefficient taking into account both the in- and out-of-plane response where appropriate.

Monolayer graphene antidot lattices (GALs) have been suggested as a route to making graphene semiconducting by nanopatterning. In paper A, bilayer graphene antidot lattices (GALs) have been investigated to extend on previous findings in monolayer GALs showing that a bandgap can be opened only for very specific lattice geometries. These findings were found to apply in the exact same form also to bilayer GALs, but has been extended by revealing a different form of the bandgap scaling with lattice parameters in the bilayer case. In addition, it has been shown that by applying a perpendicular electrostatic field to the bilayer GAL it may be possible to further tune the size of the gap simply by tuning the strength of the electric field. In principle, GALs provide for an easy way of turning graphene semiconducting, but given the high sensitivity to even minute changes in the lattice geometry, it is unlike that the large gaps seen in theory can be realized in experiments.

The promising properties of the numerous different 2D materials that have been discovered since graphene kick-started the field, have been made even more versatile with the possibility of stacking 2D materials into heterostructures tailored to specific needs. The properties of such heterostructures may

be determined by using effective medium theory (EMT) based on the bulk permittivities of the constituents. In paper B an assessment of EMT in the limit of very thin and very thick layers is made for graphene/hBN structures. It is found that even layers as thin as 5 monolayers are accurately described using monolayer permittivities, but that the choice of the top-layer of the stack significantly influences the reflective properties of the entire stack. Modes of high  $k_x$  were found to be particularly sensible to the properties of the top layers to the extent that even the effect of the edge on the electronic structure of the topmost layers drastically influence the reflection. This was found to be due to the short penetration depth of high  $k_x$  modes. A method of improving EMT by taking into account the boundary between individual layers was suggested and found to be superior to ordinary EMT especially for structures where the graphitic part was doped.

In paper C a large group of natural hyperbolic materials (NHM) were identified and compared to a silver/SiO<sub>2</sub> hyperbolic metamaterial with respect to the Purcell factor. Numerous NHM with hyperbolic dispersion in different energy regimes covering the spectrum from  $\sim 0.1$  eV to above 6 eV were found. It was found that the Purcell factor of 2H-TaS<sub>2</sub> is much larger than that of an ordinary Silver/SiO<sub>2</sub> metamaterial, and that losses are much smaller giving rise to longer propagating lengths of electromagnetic modes. The lower losses are due to a special band structure with the metallic bands being isolated from both lower and higher lying bands by a gap large enough to separate intraband from interband losses. Strong Purcell enhancement is expected in the hyperbolic regime, but in some materials such as graphite and the silver/SiO<sub>2</sub> heterostructures the Purcell factor may remain high even outside this region due to losses. 2H-HfBrS was identified as a low loss material with a very clear Purcell enhancement only inside the hyperbolic region.

In paper D the dispersion of plasmons activated by optical pumping in graphene, MoS<sub>2</sub>, and black phosphorus (BP) were compared to plasmons activated by electron doping. This was done by looking at the dispersion relations and by comparing the Purcell factor in equivalent situations chosen to yield the same plasma frequency for doping and pumping. The results were obtained within the nonlocal-RPA model, which properly takes into account the non-vertical electronic transitions that may be induced by evanescent light of high momentum. It was found that pumping and doping leads to largely identical dispersion relations with the exception that pumping leads to strong broadening due to interband transitions. Because the model of BP employed includes only two bands broadening due to interband transitions is almost non-existent, showing that materials having band structures with isolated bands may exhibit optically activated plasmons free of strong broadening. Finally, the calculations of the Purcell factor seems to suggest that strong Purcell enhancement may be observable in MoS<sub>2</sub> in the pumping scheme.



# References

- [1] K. S. Novoselov, A. K. Geim, S. Morozov, D. Jiang, Y. Zhang, S. Dubonos, I. Grigorieva, A. Firsov, Electric field effect in atomically thin carbon films, *Science* 306 (5696) (2004) 666–669.
- [2] A. K. Geim, K. S. Novoselov, The rise of graphene, *Nat. Mater.* 6 (3) (2007) 183–191.
- [3] M. Katsnelson, Minimal conductivity in bilayer graphene, *Eur. Phys. J. B* 52 (2) (2006) 151–153.
- [4] M. I. Katsnelson, Graphene: carbon in two dimensions, *Mater. Today* 10 (2007) 20.
- [5] K. I. Bolotin, K. Sikes, Z. Jiang, M. Klima, G. Fudenberg, J. Hone, P. Kim, H. Stormer, Ultrahigh electron mobility in suspended graphene, *Solid State Commun.* 146 (9) (2008) 351–355.
- [6] X. Du, I. Skachko, A. Barker, E. Y. Andrei, Approaching ballistic transport in suspended graphene, *Nat. Nanotechnol.* 3 (2008) 491.
- [7] A. S. Mayorov, R. V. Gorbachev, S. V. Morozov, L. Britnell, R. Jalil, L. A. Ponomarenko, P. Blake, K. S. Novoselov, K. Watanabe, T. Taniguchi, et al., Micrometer-scale ballistic transport in encapsulated graphene at room temperature, *Nano Lett.* 11 (6) (2011) 2396–2399.
- [8] M. Kim, N. S. Safron, E. Han, M. S. Arnold, P. Gopalan, Fabrication and characterization of large-area, semiconducting nanoperforated graphene materials, *Nano Lett.* 10 (2010) 1125.
- [9] E. O. Polat, O. Balci, N. Kakenov, H. B. Uzlu, C. Kocabas, R. Dahiya, Synthesis of large area graphene for high performance in flexible optoelectronic devices, *Scientific reports* 5 (2015) 16744.
- [10] J. Cai, P. Ruffieux, R. Jaafar, M. Bieri, T. Braun, S. Blankenburg, M. Muoth, A. P. Seitsonen, M. Saleh, X. Feng, et al., Atomically precise bottom-up fabrication of graphene nanoribbons, *Nature* 466 (7305) (2010) 470–473.

- [11] Y.-W. Son, M. L. Cohen, S. G. Louie, Energy gaps in graphene nanoribbons, *Phys. Rev. Lett.* 97 (21) (2006) 216803.
- [12] Z. Chen, Y.-M. Lin, M. J. Rooks, P. Avouris, Graphene nano-ribbon electronics, *Physica E* 40 (2007) 228–232.
- [13] V. Barone, O. Hod, G. E. Scuseria, Electronic structure and stability of semiconducting graphene nanoribbons, *Nano Lett.* 6 (2006) 2748.
- [14] L. Jiao, X. Wang, G. Diankov, H. Wang, H. Dai, Facile synthesis of high-quality graphene nanoribbons, *Nat. Nanotech.* 5 (5) (2010) 321–325.
- [15] M. Y. Han, B. Özyilmaz, Y. Zhang, P. Kim, Energy band-gap engineering of graphene nanoribbons, *Phys. Rev. Lett.* 98 (20) (2007) 206805.
- [16] B. Sachs, T. Wehling, M. Katsnelson, A. Lichtenstein, Adhesion and electronic structure of graphene on hexagonal boron nitride substrates, *Phys. Rev. B* 84 (19) (2011) 195414.
- [17] G. Giovannetti, P. A. Khomyakov, G. Brocks, P. J. Kelly, J. Van Den Brink, Substrate-induced band gap in graphene on hexagonal boron nitride: Ab initio density functional calculations, *Phys. Rev. B* 76 (7) (2007) 073103.
- [18] S. Y. Zhou, G.-H. Gweon, A. V. Fedorov, P. N. First, W. A. D. Heer, D. H. Lee, F. Guinea, A. H. C. Neto, A. Lanzara, Substrate-induced bandgap opening in epitaxial graphene, *Nat. Mater.* 6 (2007) 770.
- [19] R. Balog, B. Jørgensen, L. Nilsson, M. Andersen, E. Rienks, M. Bianchi, M. Fanetti, E. Lægsgaard, A. Baraldi, S. Lizzit, et al., Bandgap opening in graphene induced by patterned hydrogen adsorption, *Nat. Mater.* 9 (4) (2010) 315–319.
- [20] T. G. Pedersen, C. Flindt, J. Pedersen, N. A. Mortensen, A.-P. Jauho, K. Pedersen, Graphene antidot lattices: designed defects and spin qubits, *Phys. Rev. Lett.* 100 (13) (2008) 136804.
- [21] S. Yuan, R. Roldán, A.-P. Jauho, M. Katsnelson, Electronic properties of disordered graphene antidot lattices, *Phys. Rev. B* 87 (8) (2013) 085430.
- [22] M. R. Thomsen, S. J. Brun, T. G. Pedersen, Dirac model of electronic transport in graphene antidot barriers, *J. Phys. Condens. Matter* 26 (33) (2014) 335301.
- [23] R. Petersen, T. G. Pedersen, A.-P. Jauho, Clar sextet analysis of triangular, rectangular, and honeycomb graphene antidot lattices, *ACS Nano* 5 (1) (2011) 523–529.

- [24] R. Petersen, T. G. Pedersen, A.-P. Jauho, Clar sextets in square graphene antidot lattices, *Physica E* 44 (6) (2012) 967–970.
- [25] T. G. Pedersen, C. Flindt, J. Pedersen, A.-P. Jauho, N. A. Mortensen, K. Pedersen, Optical properties of graphene antidot lattices, *Phys. Rev. B* 77 (24) (2008) 245431.
- [26] A. Betti, G. Fiori, G. Iannaccone, Strong mobility degradation in ideal graphene nanoribbons due to phonon scattering, *Appl. Phys. Lett.* 98 (21) (2011) 212111.
- [27] T. Fang, A. Konar, H. Xing, D. Jena, Mobility in semiconducting graphene nanoribbons: Phonon, impurity, and edge roughness scattering, *Phys. Rev. B* 78 (20) (2008) 205403.
- [28] C. R. Dean, A. F. Young, I. Meric, C. Lee, L. Wang, S. Sorgenfrei, K. Watanabe, T. Taniguchi, P. Kim, K. L. Shepard, et al., Boron nitride substrates for high-quality graphene electronics, *Nat. Nanotech.* 5 (10) (2010) 722–726.
- [29] J.-H. Chen, C. Jang, S. Xiao, M. Ishigami, M. S. Fuhrer, Intrinsic and extrinsic performance limits of graphene devices on  $\text{SiO}_2$ , *Nat. Nanotech.* 3 (4) (2008) 206–209.
- [30] K. Ziegler, Minimal conductivity of graphene: Nonuniversal values from the kubo formula, *Phys. Rev. B* 75 (23) (2007) 233407.
- [31] Y. Shao, J. Wang, H. Wu, J. Liu, I. A. Aksay, Y. Lin, Graphene based electrochemical sensors and biosensors: a review, *Electroanalysis* 22 (10) (2010) 1027–1036.
- [32] S. K. Min, W. Y. Kim, Y. Cho, K. S. Kim, Fast dna sequencing with a graphene-based nanochannel device, *Nat. Nanotech.* 6 (3) (2011) 162–165.
- [33] H. J. Yoon, J. H. Yang, Z. Zhou, S. S. Yang, M. M.-C. Cheng, et al., Carbon dioxide gas sensor using a graphene sheet, *Sensors and Actuators B: Chemical* 157 (1) (2011) 310–313.
- [34] J. Chen, M. Badioli, P. Alonso-González, S. Thongrattanasiri, F. Huth, J. Osmond, M. Spasenović, A. Centeno, A. Pesquera, P. Godignon, et al., Optical nano-imaging of gate-tunable graphene plasmons, *Nature* 487 (7405) (2012) 77–81.
- [35] F. H. Koppens, D. E. Chang, F. J. García de Abajo, Graphene plasmonics: a platform for strong light–matter interactions, *Nano Lett.* 11 (8) (2011) 3370–3377.

- [36] I. V. Iorsh, I. S. Mukhin, I. V. Shadrivov, P. A. Belov, Y. S. Kivshar, Hyperbolic metamaterials based on multilayer graphene structures, *Phys. Rev. B* 87 (7) (2013) 075416.
- [37] E. McCann, M. Koshino, The electronic properties of bilayer graphene, *Rep. Prog. Phys.* 76 (5) (2013) 056503.
- [38] S. J. Brun, T. G. Pedersen, Intense and tunable second-harmonic generation in biased bilayer graphene, *Phys. Rev. B* 91 (20) (2015) 205405.
- [39] T. Ohta, A. Bostwick, T. Seyller, K. Horn, E. Rotenberg, Controlling the electronic structure of bilayer graphene, *Science* 313 (5789) (2006) 951–954.
- [40] E. V. Castro, K. Novoselov, S. Morozov, N. Peres, J. L. Dos Santos, J. Nilsson, F. Guinea, A. Geim, A. C. Neto, Biased bilayer graphene: semiconductor with a gap tunable by the electric field effect, *Phys. Rev. Lett.* 99 (21) (2007) 216802.
- [41] Y. Zhang, T.-T. Tang, C. Girit, Z. Hao, M. C. Martin, A. Zettl, M. F. Crommie, Y. R. Shen, F. Wang, Direct observation of a widely tunable bandgap in bilayer graphene, *Nature* 459 (7248) (2009) 820–823.
- [42] G. R. Bhimanapati, Z. Lin, V. Meunier, Y. Jung, J. Cha, S. Das, D. Xiao, Y. Son, M. S. Strano, V. R. Cooper, et al., Recent advances in two-dimensional materials beyond graphene, *ACS. Nano* 9 (2015) 11509.
- [43] K. F. Mak, J. Shan, Photonics and optoelectronics of 2d semiconductor transition metal dichalcogenides, *Nat. Photon.* 10 (4) (2016) 216–226.
- [44] X. Ling, H. Wang, S. Huang, F. Xia, M. S. Dresselhaus, The renaissance of black phosphorus, *Proc. Natl. Acad. Sci.* 112 (15) (2015) 4523–4530.
- [45] S. Balendhran, S. Walia, H. Nili, S. Sriram, M. Bhaskaran, Elemental analogues of graphene: silicene, germanene, stanene, and phosphorene, *Small* 11 (6) (2015) 640–652.
- [46] F. Xia, H. Wang, Y. Jia, Rediscovering black phosphorus as an anisotropic layered material for optoelectronics and electronics, *Nat. Commun.* 5 (4458).
- [47] A. K. Geim, I. V. Grigorieva, Van der waals heterostructures, *Nature* 499 (7459) (2013) 419–425.
- [48] L. Ponomarenko, A. Geim, A. Zhukov, R. Jalil, S. Morozov, K. Novoselov, I. Grigorieva, E. Hill, V. Cheianov, V. Fal’Ko, et al., Tunable metal-insulator transition in double-layer graphene heterostructures, *Nat. Phys.* 7 (12) (2011) 958–961.

- [49] G. Constantinescu, A. Kuc, T. Heine, Stacking in bulk and bilayer hexagonal boron nitride, *Phys. Rev. Lett.* 111 (3) (2013) 036104.
- [50] W. Paszkowicz, J. Pelka, M. Knapp, T. Szyszko, S. Podsiadlo, Lattice parameters and anisotropic thermal expansion of hexagonal boron nitride in the 10–297.5 k temperature range, *Appl. Phys. A* 75 (3) (2002) 431–435.
- [51] W. Yang, G. Chen, Z. Shi, C.-C. Liu, L. Zhang, G. Xie, M. Cheng, D. Wang, R. Yang, D. Shi, et al., Epitaxial growth of single-domain graphene on hexagonal boron nitride, *Nat. Mater.* 12 (9) (2013) 792–797.
- [52] Z. Liu, L. Song, S. Zhao, J. Huang, L. Ma, J. Zhang, J. Lou, P. M. Ajayan, Direct growth of graphene/hexagonal boron nitride stacked layers, *Nano letters* 11 (5) (2011) 2032–2037.
- [53] J. Sławińska, I. Zasada, Z. Klusek, Energy gap tuning in graphene on hexagonal boron nitride bilayer system, *Phys. Rev. B* 81 (15) (2010) 155433.
- [54] Z. Liu, H. Lee, Y. Xiong, C. Sun, X. Zhang, Far-field optical hyperlens magnifying sub-diffraction-limited objects, *Science* 315 (5819) (2007) 1686–1686.
- [55] M. Noginov, H. Li, Y. A. Barnakov, D. Dryden, G. Nataraj, G. Zhu, C. Bonner, M. Mayy, Z. Jacob, E. Narimanov, Controlling spontaneous emission with metamaterials, *Opt. Lett.* 35 (11) (2010) 1863–1865.
- [56] P. Shekhar, J. Atkinson, Z. Jacob, Hyperbolic metamaterials: fundamentals and applications, *Nano Converg.* 1 (1) (2014) 1–17.
- [57] A. Poddubny, I. Iorsh, P. Belov, Y. Kivshar, Hyperbolic metamaterials, *Nat. Photon.* 7 (12) (2013) 948–957.
- [58] K. Sreekanth, T. Biaglow, G. Strangi, Directional spontaneous emission enhancement in hyperbolic metamaterials, *J. Appl. Phys.* 114 (13) (2013) 134306.
- [59] A. M. DaSilva, Y.-C. Chang, T. Norris, A. H. MacDonald, Enhancement of photonic density of states in finite graphene multilayers, *Phys. Rev. B* 88 (19) (2013) 195411.
- [60] M. A. Othman, C. Guclu, F. Capolino, Graphene-based tunable hyperbolic metamaterials and enhanced near-field absorption, *Opt. Express* 21 (6) (2013) 7614–7632.
- [61] A. Andryieuski, A. V. Lavrinenko, D. N. Chigrin, Graphene hyperlens for terahertz radiation, *Phys. Rev. B* 86 (12) (2012) 121108.

- [62] E. E. Narimanov, A. V. Kildishev, Metamaterials: naturally hyperbolic, *Nat. Photon.* 9 (4) (2015) 214–216.
- [63] M. Esslinger, R. Vogelgesang, N. Talebi, W. Khunsin, P. Gehring, S. De Zuani, B. Gompf, K. Kern, Tetradymites as natural hyperbolic materials for the near-infrared to visible, *ACS. Photon.* 1 (12) (2014) 1285–1289.
- [64] J. A. Fürst, T. G. Pedersen, M. Brandbyge, A.-P. Jauho, Density functional study of graphene antidot lattices: Roles of geometrical relaxation and spin, *Phys. Rev. B* 80 (11) (2009) 115117.
- [65] J. A. Fürst, J. G. Pedersen, C. Flindt, N. A. Mortensen, M. Brandbyge, T. G. Pedersen, A.-P. Jauho, Electronic properties of graphene antidot lattices, *New J. Phys.* 11 (9) (2009) 095020.
- [66] R. Petersen, T. G. Pedersen, Quasiparticle properties of graphene antidot lattices, *Phys. Rev. B* 80 (2009) 113404.
- [67] A. Y. Nikitin, F. Guinea, L. Martin-Moreno, Resonant plasmonic effects in periodic graphene antidot arrays, *Appl. Phys. Lett.* 101 (15) (2012) 151119.
- [68] A. Y. Nikitin, F. Guinea, F. J. Garcia-Vidal, L. Martin-Moreno, Surface plasmon enhanced absorption and suppressed transmission in periodic arrays of graphene ribbons, *Phys. Rev. B* 85 (8) (2012) 081405.
- [69] J. G. Pedersen, T. Gunst, T. Markussen, T. G. Pedersen, Graphene antidot lattice waveguides, *Phys. Rev. B* 86 (24) (2012) 245410.
- [70] M. R. Thomsen, S. R. Power, A.-P. Jauho, T. G. Pedersen, Magnetic edge states and magnetotransport in graphene antidot barriers, *Phys. Rev. B* 94 (4) (2016) 045438.
- [71] S. J. Brun, M. R. Thomsen, T. G. Pedersen, Electronic and optical properties of graphene antidot lattices: comparison of dirac and tight-binding models, *J. Phys. Condens. Matter* 26 (26) (2014) 265301.
- [72] J. Eroms, D. Weiss, Weak localization and transport gap in graphene antidot lattices, *New J. Phys.* 11 (9) (2009) 095021.
- [73] M. Kim, N. S. Safron, E. Han, M. S. Arnold, P. Gopalan, Fabrication and characterization of large-area, semiconducting nanoporated graphene materials, *Nano Lett.* 10 (4) (2010) 1125–1131.
- [74] M. Baldoni, A. Sgamellotti, F. Mercuri, Electronic properties and stability of graphene nanoribbons: An interpretation based on clar sextet theory, *Chem. Phys. Lett.* 464 (4) (2008) 202–207.

- [75] X. Liu, Z. Zhang, W. Guo, Universal rule on chirality-dependent bandgaps in graphene antidot lattices, *Small* 9 (8) (2013) 1405–1410.
- [76] M. Dvorak, W. Oswald, Z. Wu, Bandgap opening by patterning graphene, *Sci. Rep.* 3 (2013) 2289.
- [77] F. Ouyang, S. Peng, Z. Liu, Z. Liu, Bandgap opening in graphene antidot lattices: the missing half, *ACS. Nano* 5 (5) (2011) 4023–4030.
- [78] L. A. Chernozatonskii, V. A. Demin, A. A. Artyukh, Bigraphene nanomeshes: Structure, properties, and formation, *JETP Lett.* 99 (5) (2014) 309–314.
- [79] D. G. Kvashnin, P. Vancsó, L. Y. Antipina, G. I. Márk, L. P. Biró, P. B. Sorokin, L. A. Chernozatonskii, Bilayered semiconductor graphene nanostructures with periodically arranged hexagonal holes, *Nano Res.* (2014) 1–9.
- [80] R. Petersen, T. G. Pedersen, Bandgap scaling in bilayer graphene antidot lattices, *J. Phys. Condens. Matter* 27 (22) (2015) 225502.
- [81] A. Gupta, T. Sakhivel, S. Seal, Recent development in 2d materials beyond graphene, *Prog. Mater. Sci.* 73 (2015) 44–126.
- [82] Y. Venkata Subbaiah, K. Saji, A. Tiwari, Atomically thin  $\text{mos}_2$ : A versatile nongraphene 2d material, *Adv. Funct. Mater.* 26 (13) (2016) 2046–2069.
- [83] K. Novoselov, A. Mishchenko, A. Carvalho, A. C. Neto, 2d materials and van der waals heterostructures, *Science* 353 (6298) (2016) aac9439.
- [84] S. Jahani, Z. Jacob, All-dielectric metamaterials, *Nat. Nanotech.* 11 (1) (2016) 23.
- [85] Z. Jacob, I. I. Smolyaninov, E. E. Narimanov, Broadband purcell effect: Radiative decay engineering with metamaterials, *Appl. Phys. Lett.* 100 (18) (2012) 181105.
- [86] R. Petersen, T. G. Pedersen, M. N. Gjerding, K. S. Thygesen, Limitations of effective medium theory in multilayer graphite/hbn heterostructures, *Phys. Rev. B* 94 (3) (2016) 035128.
- [87] O. Kidwai, S. V. Zhukovsky, J. Sipe, Effective-medium approach to planar multilayer hyperbolic metamaterials: Strengths and limitations, *Phys. Rev. A* 85 (5) (2012) 053842.
- [88] J. Elser, V. A. Podolskiy, I. Salakhutdinov, I. Avrutsky, Nonlocal effects in effective-medium response of nanolayered metamaterials, *Appl. Phys. Lett.* 90 (19) (2007) 191109.

- [89] H. H. Sheinfux, I. Kaminer, Y. Plotnik, G. Bartal, M. Segev, Subwavelength multilayer dielectrics: ultrasensitive transmission and breakdown of effective-medium theory, *Phys. Rev. Lett.* 113 (24) (2014) 243901.
- [90] A. Grüneis, C. Attacalite, L. Wirtz, H. Shiozawa, R. Saito, T. Pichler, A. Rubio, Tight-binding description of the quasiparticle dispersion of graphite and few-layer graphene, *Phys. Rev. B* 78 (20) (2008) 205425.
- [91] O. Kidwai, S. V. Zhukovsky, J. Sipe, Dipole radiation near hyperbolic metamaterials: applicability of effective-medium approximation, *Opt. Lett.* 36 (13) (2011) 2530–2532.
- [92] D. Lu, J. J. Kan, E. E. Fullerton, Z. Liu, Enhancing spontaneous emission rates of molecules using nanopatterned multilayer hyperbolic metamaterials, *Nat. Nanotech.* 9 (1) (2014) 48.
- [93] M. N. Gjerding, P. R. T. G. Pedersen, N. A. Mortensen, K. S. Thygesen, Layered van der waals crystals with hyperbolic light dispersion, *Nat. Commun.* 8 (2017) 320.
- [94] G. V. Naik, B. Saha, J. Liu, S. M. Saber, E. A. Stach, J. M. Irudayaraj, T. D. Sands, V. M. Shalaev, A. Boltasseva, Epitaxial superlattices with titanium nitride as a plasmonic component for optical hyperbolic metamaterials, *Proceedings of the National Academy of Sciences* 111 (21) (2014) 7546–7551.
- [95] T. Wenger, G. Viola, M. Fogelström, P. Tassin, J. Kinet, Optical signatures of nonlocal plasmons in graphene, *Phys. Rev. B* 94 (20) (2016) 205419.
- [96] E. Hwang, S. D. Sarma, Dielectric function, screening, and plasmons in two-dimensional graphene, *Phys. Rev. B* 75 (20) (2007) 205418.
- [97] J. Sun, N. M. Litchinitser, J. Zhou, Indefinite by nature: from ultraviolet to terahertz, *ACS. Photon.* 1 (4) (2014) 293–303.
- [98] P. Li, M. Lewin, A. V. Kretinin, J. D. Caldwell, K. S. Novoselov, T. Taniguchi, K. Watanabe, F. Gaussmann, T. Taubner, Hyperbolic phonon-polaritons in boron nitride for near-field optical imaging and focusing, *Nat. Commun.* 6.
- [99] Y.-C. Chang, C.-H. Liu, C.-H. Liu, S. Zhang, S. R. Marder, E. E. Narimanov, Z. Zhong, T. B. Norris, Realization of mid-infrared graphene hyperbolic metamaterials, *Nat. Commun.* 7 (2016) 10568.
- [100] M. N. Gjerding, M. Pandey, K. S. Thygesen, Band structure engineered layered metals for low-loss plasmonics, *Nat. Commun.* 8 (2017) 15133.



- [101] H. Raether, *Surface plasmons on smooth and rough surfaces and on gratings*, Springer, 2006.
- [102] W. L. Barnes, A. Dereux, T. W. Ebbesen, Surface plasmon subwavelength optics, *Nature* 424 (6950) (2003) 824–830.
- [103] J. A. Schuller, E. S. Barnard, W. Cai, Y. C. Jun, J. S. White, M. L. Brongersma, Plasmonics for extreme light concentration and manipulation, *Nat. Mater.* 9 (3) (2010) 193–204.
- [104] T. Søndergaard, S. I. Bozhevolnyi, Theoretical analysis of finite-size surface plasmon polariton band-gap structures, *Phys. Rev. B* 71 (12) (2005) 125429.
- [105] B. Liedberg, C. Nylander, I. Lunström, Surface plasmon resonance for gas detection and biosensing, *Sensor Actuator* 4 (1983) 299–304.
- [106] D. Derkacs, S. Lim, P. Matheu, W. Mar, E. Yu, Improved performance of amorphous silicon solar cells via scattering from surface plasmon polaritons in nearby metallic nanoparticles, *Appl. Phys. Lett.* 89 (9) (2006) 093103.
- [107] M. Jablan, H. Buljan, M. Soljačić, Plasmonics in graphene at infrared frequencies, *Phys. Rev. B* 80 (24) (2009) 245435.
- [108] F. J. García de Abajo, Graphene plasmonics: challenges and opportunities, *ACS. Photon.* 1 (3) (2014) 135–152.
- [109] A. Y. Nikitin, P. Alonso-González, R. Hillenbrand, Efficient coupling of light to graphene plasmons by compressing surface polaritons with tapered bulk materials, *Nano Lett.* 14 (5) (2014) 2896–2901.
- [110] Z. Fei, A. Rodin, G. Andreev, W. Bao, A. McLeod, M. Wagner, L. Zhang, Z. Zhao, M. Thiemens, G. Dominguez, et al., Gate-tuning of graphene plasmons revealed by infrared nano-imaging, *Nature* 487 (7405) (2012) 82–85.
- [111] J. Chen, M. Badioli, P. Alonso-González, S. Thongrattanasiri, F. Huth, J. Osmond, M. Spasenović, A. Centeno, A. Pesquera, P. Godignon, A. Zurutuza Elorza, N. Camara, F. J. García de Abajo, R. Hillenbrand, F. H. L. Koppens, Optical nano-imaging of gate-tunable graphene plasmons, *Nature* 487 (2012) 77–81.
- [112] A. Woessner, M. B. Lundeborg, Y. Gao, A. Principi, P. Alonso-González, M. Carrega, K. Watanabe, T. Taniguchi, G. Vignale, M. Polini, J. Hone, R. Hillenbrand, F. H. Koppens, Highly confined low-loss plasmons in graphene-boron nitride heterostructures, *Nat. Mater.* 14 (2015) 421–425.

- [113] A. Scholz, T. Stauber, J. Schliemann, Plasmons and screening in a monolayer of  $\text{mos}_2$ , *Phys. Rev. B* 88 (3) (2013) 035135.
- [114] S. Butun, S. Tongay, K. Aydin, Enhanced light emission from large-area monolayer  $\text{mos}_2$  using plasmonic nanodisc arrays, *Nano Lett.* 15 (4) (2015) 2700–2704.
- [115] T. Low, R. Roldán, H. Wang, F. Xia, P. Avouris, L. M. Moreno, F. Guinea, Plasmons and screening in monolayer and multilayer black phosphorus, *Phys. Rev. Lett.* 113 (10) (2014) 106802.
- [116] F. Jin, R. Roldán, M. I. Katsnelson, S. Yuan, Screening and plasmons in pure and disordered single-and bilayer black phosphorus, *Phys. Rev. B* 92 (11) (2015) 115440.
- [117] V. Tran, R. Soklaski, Y. Liang, L. Yang, Layer-controlled band gap and anisotropic excitons in few-layer black phosphorus, *Phys. Rev. B* 89 (23) (2014) 235319.
- [118] A. S. Rodin, A. Carvalho, A. H. Castro Neto, Strain-induced gap modification in black phosphorus, *Phys. Rev. Lett.* 112 (17) (2014) 176801.
- [119] J. C. Johannsen, S. Ulstrup, F. Cilento, A. Crepaldi, M. Zacchigna, C. Cacho, I. E. Turcu, E. Springate, F. Fromm, C. Roidel, et al., Direct view of hot carrier dynamics in graphene, *Phys. Rev. Lett.* 111 (2) (2013) 027403.
- [120] M. Breusing, C. Ropers, T. Elsaesser, Ultrafast carrier dynamics in graphite, *Phys. Rev. Lett.* 102 (8) (2009) 086809.
- [121] S. Ulstrup, J. C. Johannsen, F. Cilento, A. Crepaldi, J. A. Miwa, M. Zacchigna, C. Cacho, R. T. Chapman, E. Springate, F. Fromm, et al., Ramifications of optical pumping on the interpretation of time-resolved photoemission experiments on graphene, *J. Electron. Spectrosc. Relat. Phenom.* 200 (2015) 340–346.
- [122] S. Ulstrup, J. C. Johannsen, M. Grioni, P. Hofmann, Extracting the temperature of hot carriers in time-and angle-resolved photoemission, *Rev. Sci. Instrum.* 85 (1) (2014) 013907.
- [123] H. Wang, C. Zhang, F. Rana, Ultrafast dynamics of defect-assisted electron–hole recombination in monolayer  $\text{mos}_2$ , *Nano Lett.* 15 (1) (2014) 339–345.
- [124] A. Grubisic Cabo, J. A. Miwa, S. S. Grønberg, J. M. Riley, J. C. Johannsen, C. Cacho, O. Alexander, R. T. Chapman, E. Springate, M. Grioni, et al., Observation of ultrafast free carrier dynamics in single layer  $\text{mos}_2$ , *Nano Lett.* 15 (9) (2015) 5883–5887.

- [125] K.-J. Tielrooij, J. Song, S. A. Jensen, A. Centeno, A. Pesquera, A. Z. Elorza, M. Bonn, L. Levitov, F. Koppens, Photoexcitation cascade and multiple hot-carrier generation in graphene, *Nat. Phys.* 9 (4) (2013) 248–252.
- [126] A. Dubinov, V. Y. Aleshkin, V. Mitin, T. Otsuji, V. Ryzhii, Terahertz surface plasmons in optically pumped graphene structures, *J. Phys. Condens. Matter* 23 (14) (2011) 145302.
- [127] M. Wagner, Z. Fei, A. S. McLeod, A. S. Rodin, W. Bao, E. G. Iwinski, Z. Zhao, M. Goldflam, M. Liu, G. Dominguez, et al., Ultrafast and nanoscale plasmonic phenomena in exfoliated graphene revealed by infrared pump–probe nanoscopy, *Nano Lett.* 14 (2) (2014) 894–900.
- [128] G. Ni, L. Wang, M. Goldflam, M. Wagner, Z. Fei, A. McLeod, M. Liu, F. Keilmann, B. Özyilmaz, A. C. Neto, et al., Ultrafast optical switching of infrared plasmon polaritons in high-mobility graphene, *Nat. Photon.* 10 (2016) 244–247.
- [129] D. Basov, M. Fogler, A. Lanzara, F. Wang, Y. Zhang, et al., Colloquium: graphene spectroscopy, *Rev. Mod. Phys.* 86 (3) (2014) 959.
- [130] M. A. Huber, F. Mooshammer, M. Plankl, L. Viti, F. Sandner, L. Z. Kastner, T. Frank, J. Fabian, M. S. Vitiello, T. L. Cocker, et al., Femtosecond photo-switching of interface polaritons in black phosphorus heterostructures, *Nat. Nanotech.* 12 (3) (2017) 207–211.
- [131] O. Hess, J. B. Pendry, S. A. Maier, R. F. Oulton, J. Hamm, K. Tsakmakidis, Active nanoplasmonic metamaterials, *Nat. Mater.* 11 (7) (2012) 573–584.
- [132] F. Rana, Graphene terahertz plasmon oscillators, *IEEE Trans. Nanotechnol.* 7 (1) (2008) 91–99.
- [133] Z. Sun, D. Basov, M. Fogler, Adiabatic amplification of plasmons and demons in 2d systems, *Phys. Rev. Lett.* 117 (7) (2016) 076805.
- [134] R. Kitamura, L. Pilon, M. Jonasz, Optical constants of silica glass from extreme ultraviolet to far infrared at near room temperature, *Appl. Optics* 46 (33) (2007) 8118–8133.
- [135] A. Hill, S. Mikhailov, K. Ziegler, Dielectric function and plasmons in graphene, *Europhys. Lett.* 87 (2) (2009) 27005.
- [136] H. Ehrenreich, M. H. Cohen, Self-consistent field approach to the many-electron problem, *Phys. Rev.* 115 (4) (1959) 786.

- [137] T. G. Pedersen, K. Pedersen, T. B. Kriestensen, Optical matrix elements in tight-binding calculations, *Phys. Rev. B* 63 (20) (2001) 201101.
- [138] L. L. Y. Voon, L. Ram-Mohan, Tight-binding representation of the optical matrix elements: Theory and applications, *Phys. Rev. B* 47 (23) (1993) 15500.
- [139] T. G. Pedersen, P. Modak, K. Pedersen, N. E. Christensen, M. M. Kjeldsen, A. N. Larsen, Ab initio calculation of electronic and optical properties of metallic tin, *J. Phys. Condens. Matter* 21 (11) (2009) 115502.
- [140] M. Klein, Furtak, "optics (1986).
- [141] J. J. Saarinen, J. Sipe, A green function approach to surface optics in anisotropic media, *J. Mod. Opt.* 55 (1) (2008) 13–32.
- [142] R. J. Gehr, G. L. Fischer, R. W. Boyd, J. Sipe, Nonlinear optical response of layered composite materials, *Phys. Rev. A* 53 (4) (1996) 2792.
- [143] D. K. Samarakoon, X.-Q. Wang, Tunable band gap in hydrogenated bilayer graphene, *ACS Nano* 4 (7) (2010) 4126–4130.
- [144] E. Taft, H. Philipp, Optical properties of graphite, *Phys. Rev.* 138 (1A) (1965) A197.
- [145] G. E. Jellison Jr, J. D. Hunn, H. N. Lee, Measurement of optical functions of highly oriented pyrolytic graphite in the visible, *Phys. Rev. B* 76 (8) (2007) 085125.
- [146] A. Beal, H. Hughes, Kramers-kronig analysis of the reflectivity spectra of 2h-mos<sub>2</sub>, 2h-mose<sub>2</sub> and 2h-mote<sub>2</sub>, *J. Phys. C Solid State* 12 (5) (1979) 881.
- [147] S. Bayliss, W. Liang, Symmetry dependence of optical transitions in group 4b transition metal dichalcogenides, *J. Phys. C Solid State* 15 (6) (1982) 1283.
- [148] S. Lebègue, T. Björkman, M. Klintonberg, R. M. Nieminen, O. Eriksson, Two-dimensional materials from data filtering and ab initio calculations, *Phys. Rev. X* 3 (3) (2013) 031002.
- [149] A. Beal, H. Hughes, W. Liang, The reflectivity spectra of some group va transition metal dichalcogenides, *J. Phys. C Solid State* 8 (24) (1975) 4236.
- [150] S. Bayliss, W. Liang, Reflectivity, joint density of states and band structure of group ivb transition-metal dichalcogenides, *J. Phys. C Solid State* 18 (17) (1985) 3327.

- [151] T. Buslaps, R. Johnson, G. Jungk, Spectroscopic ellipsometry on 1t-tise2, *Thin solid films* 234 (1-2) (1993) 549–552.
- [152] J. Heyd, G. E. Scuseria, M. Ernzerhof, Hybrid functionals based on a screened coulomb potential, *J. Chem. Phys.* 118 (18) (2003) 8207–8215.
- [153] T. Li, J. Khurgin, What are the merits of hyperbolic metamaterials?, in: *Lasers and Electro-Optics (CLEO), 2016 Conference on, IEEE, 2016*, pp. 1–2.
- [154] G.-B. Liu, W.-Y. Shan, Y. Yao, W. Yao, D. Xiao, Three-band tight-binding model for monolayers of group-vib transition metal dichalcogenides, *Phys. Rev. B* 88 (8) (2013) 085433.
- [155] P. A. D. Goncalves, N. M. Peres, *An Introduction to Graphene Plasmonics*, World Scientific, 2016.

ISSN (online): 2446-1636  
ISBN (online): 978-87-7210-073-9

AALBORG UNIVERSITY PRESS